ASTRO-F Observer's Manual

Version 3.2

— for Open Time Observation Planning —

ASTRO-F User Support Team

in

Institute of Space and Astronautical Science / JAXA

contact: iris_help@ir.isas.jaxa.jp

European Space Astronomy Centre / ESA

contact: http://astro-f.esac.esa.int/esupport/

November 29, 2005

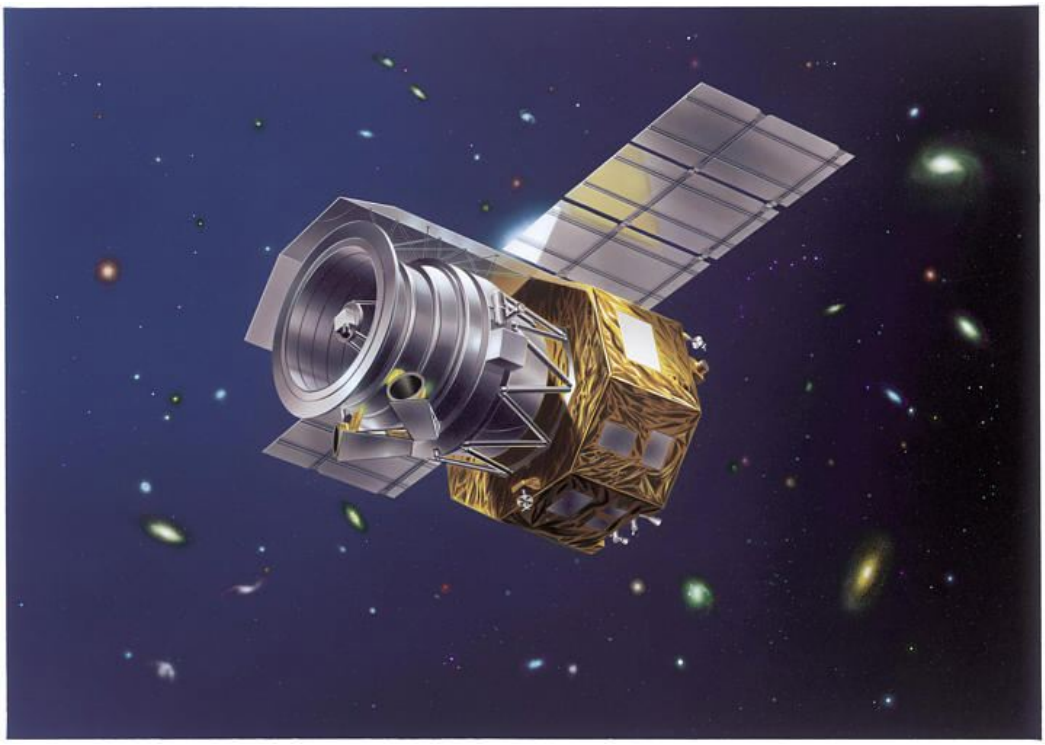

Revision Record

2005 Nov. 29:	Version 3.2 released. Updated description of IRC FoV and slit (Section 5.1.4 and 5.1.5). Updated IRC04 detection and saturation limits. Also improve the description (Section 5.5.9). Section 5.4.2 revised to clarify the point. Units for Ho given value in p.113.
2005 Nov. 8:	Version 3.1 released. Updated Visibility Map for Open Time Users (Figure 3.4.3) Information for the handling of Solar System Object observations (Section 3.4) Updated saturation limits for FTS (FIS03) mode (Table 4.4.16) IRC04 detection limits for NG+Np added (Table 5.5.25,5.5.26) Updated worked examples using the latest versions of the Tools (Section B) ESAC web pages URL and Helpdesk contact address updated Numerous errors and typos corrected
2005 Sep.20:	Version 3.0 released.

Contents

Chapter 1

Introduction

1.1 Purpose of this document

This *ASTRO-F Observer's Manual*, is issued as the reference for ASTRO-F observers, for observation planning and the preparation for the data analysis. The current version (3.0) is mainly used for the preparation of Open Time Proposals.

The document covers the specifications of the satellite and the instruments, their performance, flight operation plan, including definitions of the Astronomical Observation Templates (AOTs), and the data reduction system. It contains the most up-to-date estimates of the detection limits of the instruments (based on the performance evaluation tests carried out over the last few months). This version (version 3) contains more a detailed introduction to the mission and instruments, guidance to the users on how to prepare their observations, and the scope for the data reduction.

Information about the scientific programmes and proposal handling are not included in this document. Users are suggested to refer to other information resources (see the next page).

Note that some of the instrumental performance information was not yet available by the time of the publication of this edition version. Frequent updates will be given on the Observer's support Web page.

Figure 1.1.1: ASTRO-F on the vibration test bench (May, 2005).

1.2 Relevant Information

ASTRO-F Observer's Web

The ISAS Web page contains some additional information and data useful for the observers. Also links to the user support tools are given:
URL:*http://www.ir.isas.jaxa.jp/ASTRO-F/Observation/*

The ESAC page includes mission overview, fact sheet, and user support policy for the European Open Time proposals. Web tools are also available.
URL:*http://astro-f.esac.esa.int/*

Helpdesk

Any questions and comments on ASTRO-F observations and user support are addressed to the ASTRO-F Helpdesks.
iris_help@ir.isas.jaxa.jp: for Japanese & Korean Open Time Users and general inquiry.
http://astro-f.esac.esa.int/esupport/ : for ESA Open Time Users

Chapter 2

Mission Overview

2.1 The ASTRO-F Mission

ASTRO-F (previously known as IRIS) is the second Japanese space mission for infrared astronomy. The satellite will be launched by JAXA's M-V rocket. The launch is expected to take place in January–February 2006 [1]. The orbit is a Sun-synchronous polar orbit with an altitude of 745 km and a period of 100 minutes. The cryogen lifetime is expected to be 550 days. A pair of Stirling cycle mechanical coolers enables this long lifetime with only 170 liters of liquid Helium. Even after the liquid Helium has boiled-off, observations at near-infrared wavelengths can be continued.

ASTRO-F is equipped with a 68.5 cm cooled telescope and two scientific instruments, namely the Far-Infrared Surveyor (FIS) and the Infrared Camera (IRC). The FIS has two 2-dimensional detector arrays and observes in four far-infrared bands between 50 and 180 μm. The IRC consists of three cameras covering 1.7–26 μm in 9 bands with fields of view of approximately $10' \times 10'$. Both instruments have low- to moderate-resolution spectroscopic capability.

A major goal of the mission is to carry out an All-Sky Survey with the FIS and additionally with the IRC at 9 and 18 μm. The ASTRO-F All-Sky Survey will significantly surpass the previous all-sky survey in the infrared by IRAS in both spatial resolution and sensitivity. The results will be published as ASTRO-F infrared source catalogues. In addition to the survey observations, ASTRO-F will carry out thousands of dedicated pointed observations with both the FIS and IRC. Deep imaging as well as spectroscopic observations are available. Two high-visibility regions, the North Ecliptic Polar (NEP) region and the Large Magellanic Cloud (LMC) will be observed intensively by the pointed observations. These surveys are operated by the ASTRO-F Project in a similar vein to the All-Sky Survey. Many pointed observations are used for the legacy observations by the ASTRO-F project team members. Such programmes are referred to as "Mission Programmes". In addition, a significant fraction of pointed observation opportunities will be open for general users in Japan/Korea and ESA related countries.

Many international collaborations are ongoing with the ASTRO-F project. The European Space Agency (ESA) will supply a ground station operated by ESOC, and ESAC will carry out the pointing reconstruction of the All-Sky Survey observations. ESAC will also handle the user support for the European Open Time observing programmes. A consortium of Imperial College University of London, University of Kent, Sussex University, and SRON-Groningen with the University of Groningen (IKSG consortium) participates on the data reduction of the FIS All-Sky Survey. Seoul National University representing the Korean community also joins the data reduction activity. Several collaborations at the personal level are also ongoing especially on the celestial calibrators.

[1] Precise launch schedule will be given later this year.

2.2 Satellite

Figure 2.2.1 shows the overall structure of the ASTRO-F spacecraft. The hight is about 3.7 m (excluding the aperture lid) and the launch weight will be 960 kg. The satellite consists of two parts, the bus module and the cryostat. The two parts are connected by a truss structure.

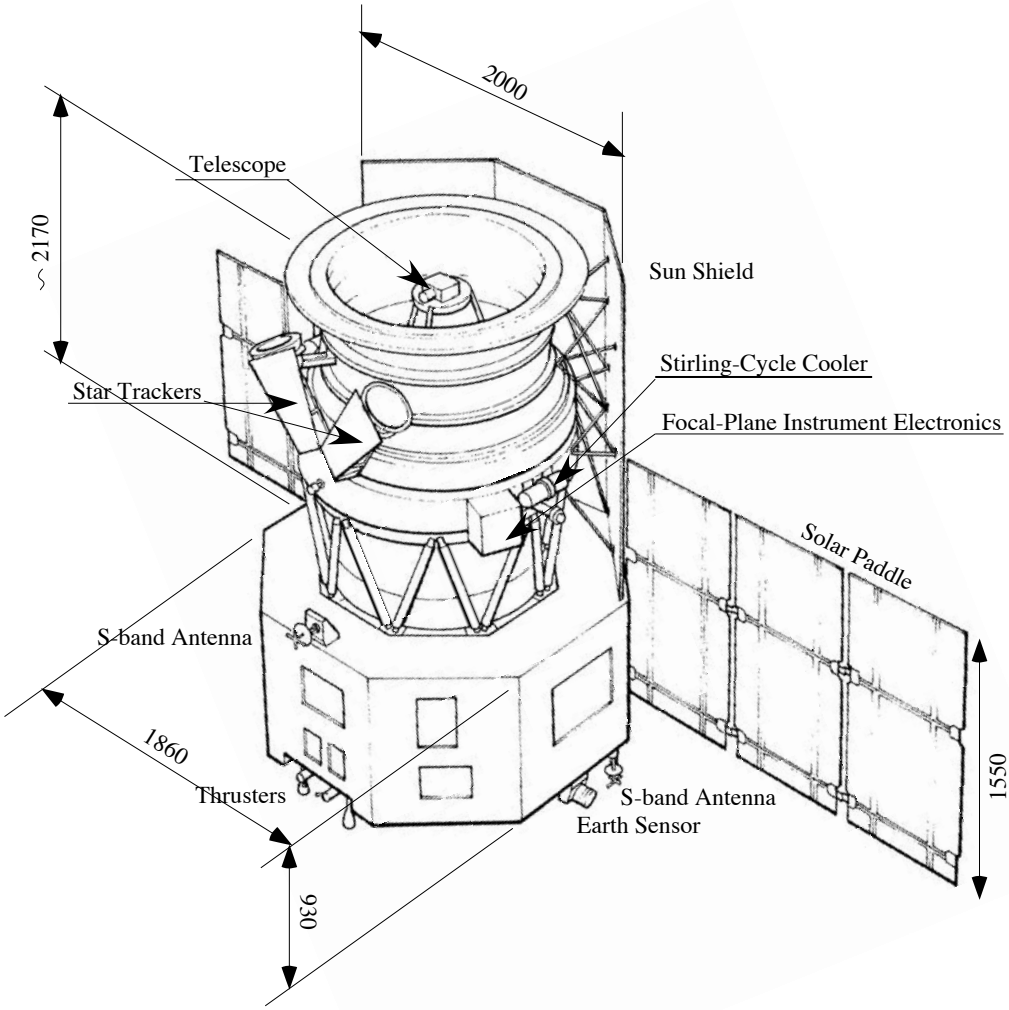

Figure 2.2.1: An overall view of the ASTRO-F spacecraft (scales are in mm).

2.2.1 The Bus Module

The bus module takes care of the power supply, house keeping, spacecraft attitude control, data acquisition and the telecommunication link to the ground station. ASTRO-F uses the S-band (mainly for command and house-keeping telemetry data) and the X-band (mainly for scientific data) for telecommunication. Due to its' near-Earth orbit, communication between the satellite and the ground stations is limited. Therefore, ASTRO-F has a two-Gigabyte data recorder.

2.2.2 Attitude Determination and Control System

The attitude of the ASTRO-F satellite is determined and controlled by on-board sensors and a computer unit. Figure 2.2.2 shows the block diagram of the attitude and orbit control system (AOCS). The framework of the system is as follows: The IRU (Gyro) measures the motion of the satellite. The TFSS (Two-dimensional Fine Sun Sensor) monitors the position of the Sun in two-dimensions perpendicular to the Sun-satellite direction, and corrects any long-term drift of the IRU signal. A pair of Star Sensors (STT) mounted on the wall of the cryostat are used to observe the attitude along the third axis and the alignment change between the bus module, where IRU and TFSS are located, and the cryostat in which the telescope is installed. Other instruments provide additional information for attitude determination. A dedicated computer (AOCU) will determine the satellite attitude. A set of reaction wheels (RW) will control the spacecraft attitude, with the help of Magnetic Torque Rods (MTQ). In the case of any very large required motion, a set of thrusters may be used, but this is not expected during the survey (until liquid Helium boil off).

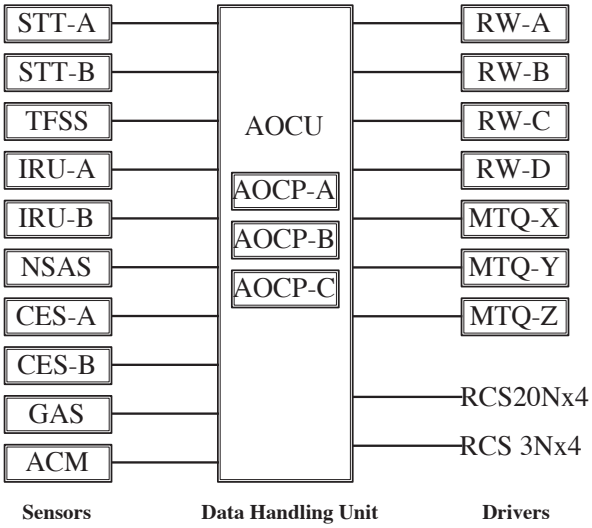

Figure 2.2.2: Block diagram of the ASTRO-F attitude determination and control system.

Table 2.2.1: ASTRO-F AOCS Performance

Absolute Pointing Control Accuracy	30 arcsec
Scan Speed Stability (in-scan)	< 0.1 per cent
Scan Speed Stability (cross-scan)	3×10^{-5} arcsec/min
Pointing Stability	< 1 arcsec/min (peak-to-peak)

2.2.3 Cryogenics

Scientific instruments are all stored in the cryostat and maintained at cryogenic temperatures by 170 liters of super-fluid liquid Helium with the help of two sets of Stirling-cycle coolers. The expected lifetime of the cryogen is 550 days. The near-infrared instrument can be operated with the mechanical coolers even after the liquid Helium boil-off. ASTRO-F will be operated with the Sun-shield always directed to the Sun. The cryostat is covered by silver coated film that reflects visible light but radiates in the infrared.

The Scientific Instrument Assembly (SIA), namely the telescope and the Focal-Plane Instruments (FPI) are thermally shielded by two layers of Vapour Cooled Shield (VCS) in which Helium vapour evaporated from the tank is running through. The inner VSC is also cooled by the mechanical coolers. The SIA is mainly cooled by the Helium vapour down to about 6 K. The FIS body and two detectors are directly connected to the Helium tank via thermal straps and are operated at 2.0–2.2 K.

The two mechanical coolers are designed to work symmetrically to cancel the momentum that may interfere with the spacecraft attitude control system. High-frequency noise remains, and we recognize that it interferes with the FTS mode observation by the FIS. See Section 4.1.4 for details.

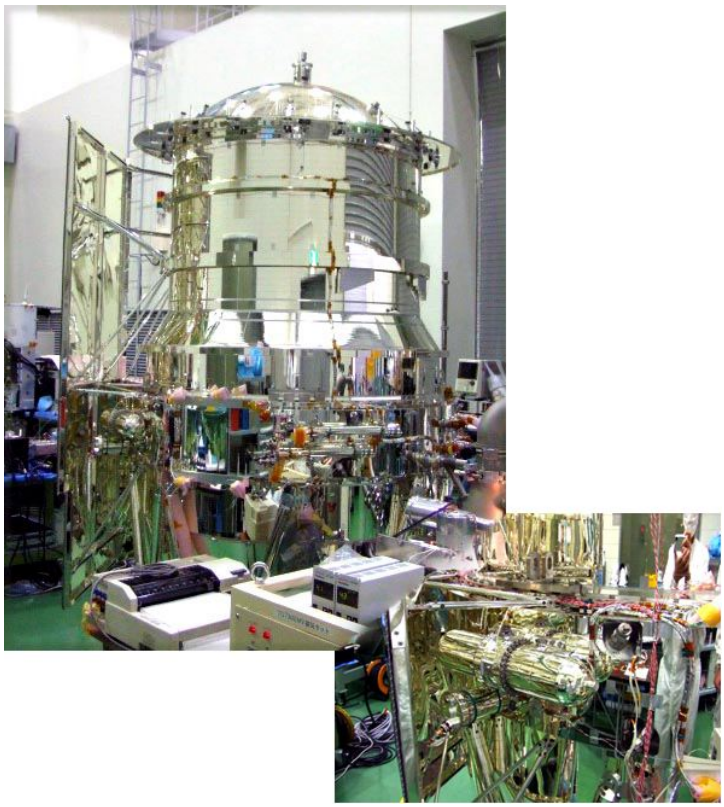

Figure 2.2.3: The ASTRO-F Cryogenic system in the clean room for maintenance. (Left) The Cryostat. (Right) Close-up of the Two-Stage Stirling cooler. (Photo: July, 2005)

2.3 Telescope

2.3.1 Specification

The telescope is a Rithcy-Chrétien system with an effective aperture of 68.5 cm and a focal ratio of 6.1 (Figure 2.3.4). The mirrors are made of SiC porous+CVD coated material. This rigid material allows us to reduce the weight of the mirrors significantly. The primary mirror, with a physical diameter of 71 cm, weighs only 11 kg. The total weight of the telescope system is 42 kg. The focus may be adjusted in orbit during the PV phase by moving the position of the secondary mirror. The parameters for the telescope are summarized in Table 2.3.2.

The primary mirror was replaced in 2004 as a part of a refurbishment of the telescope system. The effective aperture has been increased slightly (previously 67 cm). The telescope has been tested in the cryogenic vibration tests, and the mirror support system which previously had a problem has been confirmed to be secure.

The telescope of ASTRO-F is cooled mainly by Helium vapour evaporated from the tank. The nominal operation temperature is 5.8 K.

Figure 2.3.4: The ASTRO-F telescope system.

Table 2.3.2: Telescope Specification

Effective diameter	68.5 cm (primary mirror)
Focal length	420 cm
Focal ratio	6.1
Optical design	Ritchey-Chrétien type
Temperature	$\sim$ 5.8 K

2.3.2 Pre-flight performance

Mirror surface accuracy has been measured at cryogenic temperatures (as low as 9 K). Due to thermal stress at the supporting points, the wave front error becomes larger at low temperatures and is at its' worse at around 50 K, but improves slightly beyond that.

The analysis of the cryogenic tests of the telescope predict that the system reaches the diffraction limit at 6.2 μm, slightly longer than the original design goal (at 5 μm).

The focus position of the telescope has been measured accurately in cryogenic optical tests, and the telescope will be adjusted to the best position at the launch. Further focus adjustments may be carried out in orbit during the performance verification (PV) phase.

No indication of stray light has been observed, though the tests were not intended to simulate the complete flight environment. This will also be measured in the PV phase.

2.4 Focal-Plane Instruments

2.4.1 Specification Overview

Two scientific instruments are placed in the Focal-Plane of the telescope; the Far-Infrared Surveyor (FIS) and the Infrared Camera (IRC). In addition, two sets of Focal-Plane Star Sensors (FSTS) are installed for observing guide stars in the Near Infrared band ($\sim$ J-band) for pointing reconstruction during the survey observations.

The FIS is equipped with two sets of two-dimensional detector arrays. The Short-Wavelength channel (SW; 50–110 μm) uses two monolithic Ge:Ga arrays[2] of 20×3 and 20×2 pixels, while the Long-Wavelength channel (LW; 110–180 μm) has a stressed Ge:Ga array of $15 \times 3 + 15 \times 2$ pixels. Each of the four arrays correspond to a different wavelength band. The pixel sizes are 27 and 44 arcsec^2, respectively.

The IRC consists of three independent cameras; the NIR (2–5 μm), the MIR-S (5–13 μm), and the MIR-L (13–26 μm). The NIR camera has a 512×412 pixel InSb array, of which 100×412 pixels are dedicated for slit spectroscopy. The two MIR cameras use 256×256 pixel Si:As detectors.

Table 2.4.3: Observation Capabilities of ASTRO-F.

	Channel	Band	Wavelength (μm)	Resolution ($\lambda/\Delta\lambda$)	Detector Array (pix^2)	FoV (arcmin^2)
IRC	NIR	N2	1.7–2.7	3.6	InSb 512×412	9.5×10.0
		N3	2.7–3.7	2.8		
		N4	3.7–5.5	3.4		
		NP	1.7–5.5	22@3.5 μm		
		NG	2.5–5.0	135@3.6 μm		
	MIR-S	S7	5.8–8.4	2.8	Si:As 256×256	9.1×10.0
		S9W	6.5–11.6	2.1		
		S11	8.6–14.1	2.3		
		SG1	5.5–8.3	47@6.6 μm		
		SG2	7.4–13.0	34@10.6 μm		
	MIR-L	L15	12.4–19.4	2.5	Si:As 256×256	10.3×10.2
		L18W	13.9–25.3	1.8		
		L24	20.4–26.5	4.3		
		LG1		*Not Available*		
		LG2	17.7–25.0	27@20.2 μm		
FIS	SW	N60	50–80	2.2	Ge:Ga 20×2	10×1.5
		WIDE-S	60–110	1.8	Ge:Ga 20×3	10×1.0
	LW	WIDE-L	110–180	2.0	Stressed Ge:Ga 15×3	12×2.5
		N160	140–180	4.0	Stressed Ge:Ga 15×2	12×1.6
	FTS		60–180	150–450	WIDE-S + WIDE-L	

[2]The SW detector was manufactured by NICT.

The wavelength range and resolving power provided by the scientific instruments are shown in Figure 2.4.5. The spatial resolution and the Field of View (FoV) of the instruments are summarized in Figure 2.4.6. The detection limits are illustrated in Figure 2.4.7.

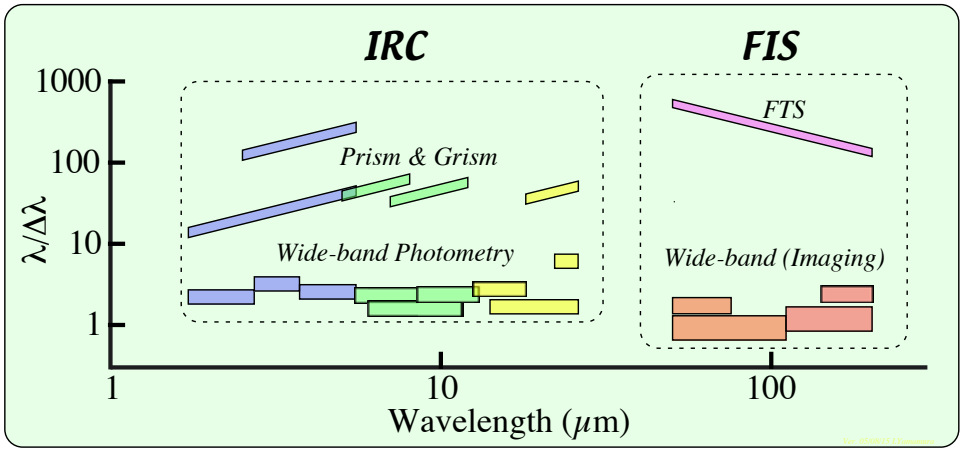

Figure 2.4.5: The wavelength coverage and resolving power of the ASTRO-F instruments.

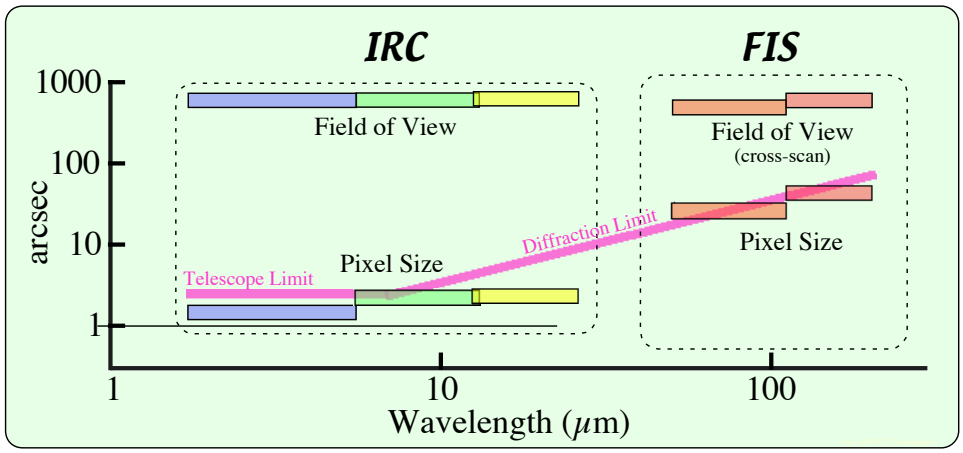

Figure 2.4.6: Pixel size and field of view (FoV) of the ASTRO-F on board instruments.

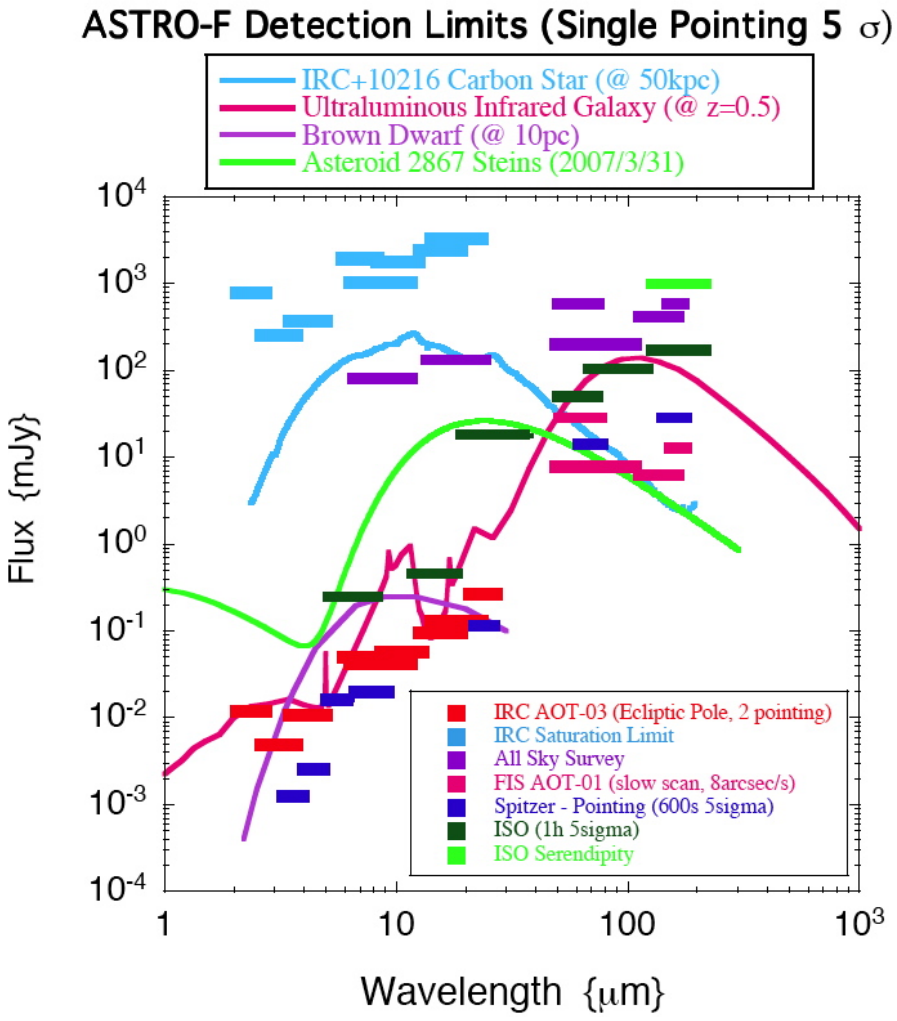

Figure 2.4.7: Detection limits of the ASTRO-F onboard instruments in various observing modes.

2.4.2 Focal-Plane Layout

Figure 2.4.8 shows the Focal-Plane layout projected onto the sky. There are three light entrances to the instruments; one for the FIS and two for the IRC. The two instruments essentially can observe simultaneously, but they see different areas of the sky as shown in the figure. Therefore, observations of a sky position with different aperture have to be made on different orbits.

The incident infrared radiation coming into the FIS aperture is divided into two spectral domains by a dichroic beam splitter, as a result of which the FIS-SW and LW detector arrays observe almost the same sky position. A small difference remains due to difference in pixel size of each detector array (see Figure 4.1.3). Similarly, the NIR and MIR-S cameras of the IRC share the same FoV so as to observe the same sky position. Only the MIR-L channel observes a different sky position.

The scan path is approximately parallel to the Ecliptic meridian line. The scan direction depends on the launch configuration, namely the launch time (morning or evening). The current plan is a morning launch, with the FoV moving downward, i.e., stars go through the detector from bottom to top on the figure.

Note that the real position and the shape of each Focal-Plane Instrument on the sky will be slightly different from those shown in Figure 2.4.8, due to optical aberration. See Section 4.1.3 (FIS) and 5.1.4 (IRC) for details.

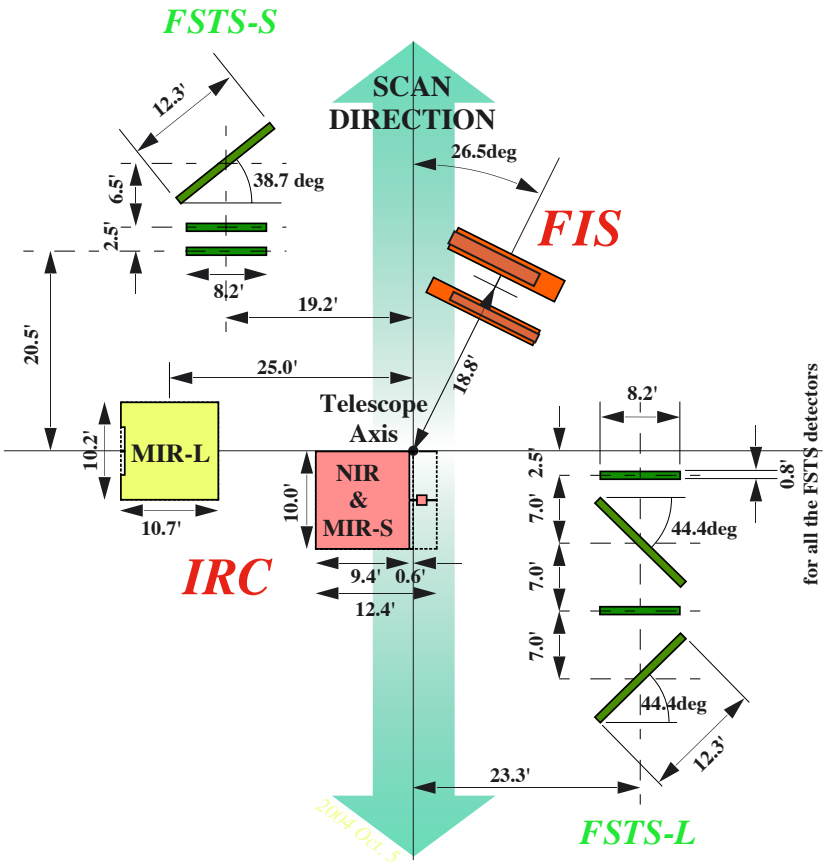

Figure 2.4.8: Focal-Plane layout projected onto the sky. The distortion due to the telescope and instrumental optics have to be taken into account for the data reduction. See the instrument pages for details.

2.4.3 The Focal-Plane Star Sensor (FSTS)

A pair of star sensors are installed in the Focal-Plane. The *FSTS-L* consists of four Ge detector elements[3], while the *FSTS-S* has three. They observe stars with their intrinsic wavelength band profile close to the J-band (1.25 μm). The readout is a TIA (TransImpedance Amplifier) circuit with a sampling rate of about 50 Hz. The seven detectors are sampled almost simultaneously.

As the satellite scans the sky, stars cross the detectors in the in-scan direction one after another. The detection interval between a pair of two horizontal detectors placed in parallel defines the scan speed, and the interval between the tilted and horizontal detectors can be converted to the cross-scan position. The two FSTS's located in opposite corners provide information on the roll angle of the Focal-Plane with respect to the scan direction, as well as a redundancy for the star detection. The absolute positional information is given by comparing the detection information with the position reference catalogue. The pointing reconstruction using the FSTS assumes (all-sky) survey operation mode. It is not decided whether the FSTS data can be used for the Slow-Scan operation for pointed observations.

Although the FSTS is controlled via the FIS electronics and software, and the data is transfered within the FIS data telemetry packet, the data may not be provided to the users for analysis. The pointing reconstruction processing is carried out by a dedicated team at ESAC/ESA and the results are provided to the All-Sky Survey data reduction team.

[3]One of the four elements is known to be dead. The effect of this loss to the pointing reconstruction is expected to be small.

2.5 The ASTRO-F Observation Programms

Observations with the ASTRO-F can be divided into three categories.

Large Area Survey (LS): Survey programmes of wide areas of the sky which use the ASTRO-F capabilities most efficiently. Three observing programmes are included in this category; the All-Sky Survey (LSASS), the North Ecliptic Pole Survey (LSNEP) and the Large Magellanic Cloud Survey (LSLMC). The latter two surveys will use the pointed observation mode. Planning and data processing of these programmes are led by dedicated teams in the ASTRO-F Project, and the products will be released to the communities.

Mission Programmes (MP): Seventy per cent of the pointed observation opportunities are allocated to the ASTRO-F team members as a kind of guaranteed observation time. Specific working groups in every scientific field have worked to establish the observing programmes. In total 15 Mission Programmes are assigned. The data will be used by the team members for a one year prioritized period and then will be opened to the public. The MP observations, as well as the LS are regarded as the legacy of the ASTRO-F mission.

Open Time Programmes (OT): The remaining 30 per cent of the total pointing opportunities are available to the general research community. Two thirds of the opportunities (= 20 per cent of the total) are reserved for Japanese/Korean astronomers, and 10 per cent are for the ESA member countries. Details of the Call for Open Time Proposals are explained in a separate document.

Chapter 3

Satellite Operations

3.1 Orbit and Observing Attitude

The orbit of ASTRO-F is a Sun-synchronous polar orbit along the twilight zone. The nominal altitude is 745 km, corresponding to an orbital period of 100 min. Once ASTRO-F is brought into this orbit in the initial maneuver operation, no adjustments or changes of the orbit during the mission will be performed in principle until the boil-off of the liquid Helium, in order to avoid contamination by the thruster gas.

In principle, the spacecraft always points in the direction perpendicular to the Sun–Earth line, keeping the Sun-shield towards the Sun, and rotates once per orbit to look in the opposite direction to the Earth. The spacecraft attitude in the cross-scan direction[1] has a flexibility of ±1 degree about the canonical scan path.

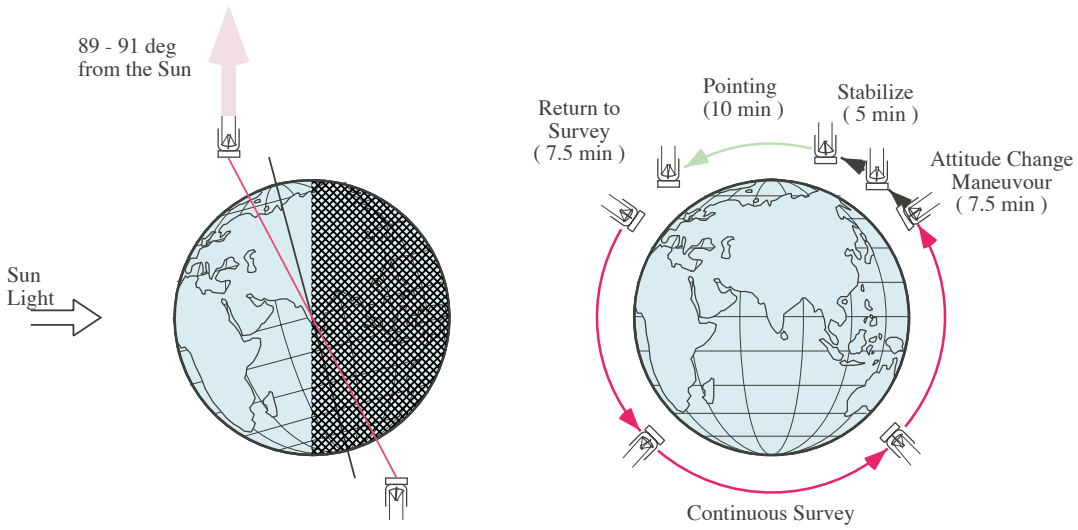

Figure 3.1.1: The in-orbit attitude of ASTRO-F (left) and the pointed observation maneuver (right).

Observations by ASTRO-F will be carried out either in survey mode or pointing mode. In the survey mode, the satellite is operated such that the telescope scans the sky with a constant speed (3.6 arcmin / sec) usually along the great-circle at a solar-elongation of 90 degrees. In the pointing mode, the telescope can point at an area of the sky along the scan path for up to 10

[1] the direction perpendicular to the scanning (in-scan) direction.

minutes, with the total cost of 30 minutes including maneuver for the operation. Fine control of the observing position in a pointing operation is possible. Observations in the pointing mode will be defined by a set of Astronomical Observation Templates (AOT; see Sections 4.4 and 5.5).

Table 3.1.1: ASTRO-F Orbit.

Altitude	745 km (−0 km +145 km)
Orbital Period	100 min

The satellite attitude and orbit control system (AOCS) has the capability of determining / controlling the absolute attitude to an accuracy of 30 arcsec. The dominant source of the pointing uncertainty is the alignment of the focal-plane axis with respect to the AOCS reference frame on the bus module and its time variation due to thermal distortion of the spacecraft.

Table 3.1.1 summarizes the nominal operation parameters and expected performance of the ASTRO-F AOCS for astronomical observations.

3.2 Attitude Operation Modes for Observations

3.2.1 Survey Mode

In the survey mode, ASTRO-F performs a continuous scan of the sky. The spacecraft spins around the Sun-pointed axis once every orbit, keeping the telescope pointed toward the opposite direction to the Earth (see left-hand of Figure 3.1.1); as a result, the telescope traces a great circle with a solar elongation of 90 deg. The orbital period of 100 minutes corresponds to a scan-speed of 3.6 arcmin s^{-1}. In Table 3.2.2, the specification and performance of the survey mode operation are summarized.

Table 3.2.2: Summary of Survey mode operation (nominal).

Specification of Survey mode operation	
Survey Scan Speed	3.6 arcmin s^{-1}
Survey In-scan Stability[1]	≤ 0.1 per cent
Survey Cross-scan Stability[1]	$\sim 3 \times 10^{-5}$ deg/sec (3σ)
Pointing determination error (goal)	
On-board	< 30 arcsec (in-scan and cross-scan)
G-ADS	15–30 arcsec (in-scan and cross-scan)
Pointing Reconstruction (During Mission)	< 5 arcsec (in-scan), < 7 arcsec (cross-scan)
Pointing Reconstruction (Post-Mission)	< 3 arcsec (in-scan), < 5 arcsec (cross-scan)

[1] Based on the performance evaluation tests.

The accurate position of the survey scan path on the sky will be determined during the pointing reconstruction processing. There are three levels of the processing: on-board determination by the attitude and orbit control system (AOCS), on-ground processing using the same dataset (G-ADS), and detailed analysis together with the Focal-Plane Star Sensor (FSTS) and IRC survey data.

The outline of the attitude determination process is summarized in Figure 3.2.2. The on-board attitude analysis has an absolute error of $\sim$ 30 arcsec. The main source of this error is the alignment uncertainty between the satellite AOCS and the telescope's focal-plane. The results of the on-board analysis are downloaded to the ground with the sensor signal data. The data is re-analyzed by the G-ADS for cross-check and to prepare the initial pointing data for reconstruction. At this stage, the pointing data (in the survey mode) still has an error of 15–30 arcsec.

Then, the data from the FSTS and the IRC survey will be analyzed together with the initial pointing data for refinement (pointing reconstruction). The ESA European Space Astronomy Centre (ESAC) is in charge of the final pointing reconstruction. The goal of the pointing accuracy after the reconstruction is 5 arcsec (in-scan) and 7 arcsec (cross-scan) during the survey. This accuracy will be improved to 3 arcsec (in-scan) and 5 arcsec (cross-scan) when the survey is completed and all data are analyzed and reprocessed.

3.2.2 Pointing Mode

In the pointing mode, ASTRO-F will observe a specific sky position. Both imaging and spectroscopic observations with longer exposure times than the survey are possible. A single pointed observation consists of four continuous operations (Figure 3.1.1, right);

1. Slewing maneuver to point the telescope at the target position,

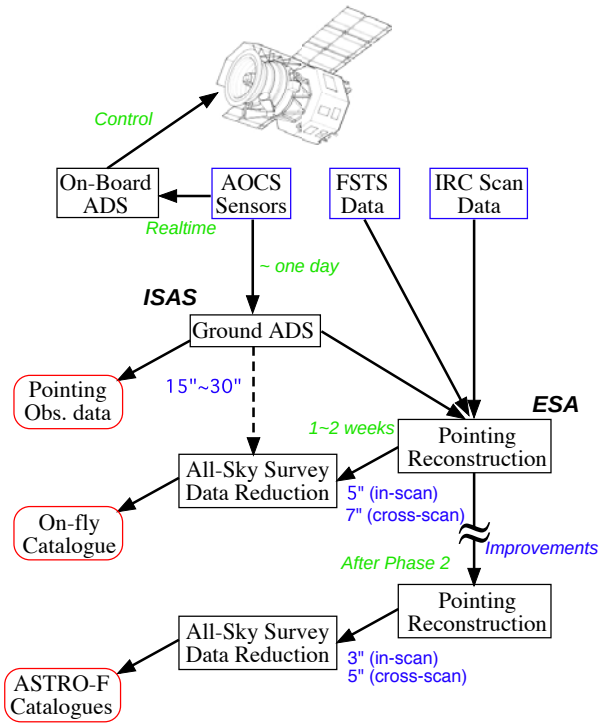

Figure 3.2.2: The outline of the ASTRO-F attitude determination for the All-Sky Survey, including time scales and envisioned accuracy improvement. Note that the pointing reconstruction by ESA will not be carried out for the pointed observations.

2. Stabilization of the telescope,
3. Observation of the target,
4. Returning to the survey mode.

The total operation is completed in 30 minutes. This means that the maximum number of pointed observations per orbit is three, if and when we can find a suitable set of targets separated by $\sim$ 120 deg. The actual net observation time per pointing is however limited to 10 minutes. To increase the flexibility of the observation opportunity for any target, the telescope can point at any position on the sky in a stripe of 2 degree ($\pm$1 deg) perpendicular to the nominal scan path. However, this allowance is much smaller than previous missions such as IRAS, ISO and Spitzer. Observers have to understand that the visibility of ASTRO-F to observe a specific target is extremely limited.

In order to avoid the Earth-light, the satellite starts slewing back to the survey mode automatically if the avoidance angle exceeds the limit. This happens without notifying the instruments to complete the observation. As a result, the very last part of some observation data may be lost in some unfortunate cases. In Table 3.2.3, we summarize the specifications of the pointing mode.

The FoV is allowed to shift by a small amount in a pointed observation in the way summarized in Table 3.2.4. The Step-Scan and the Micro-Scan are essentially the same operation, being different only in the amount of shift for one step. For the Slow-Scan operation, the spacecraft scans the sky with constant speeds of 1–15 arcsec/sec. An additional speed of 30 arcsec/sec may be available if it is validated during the PV Phase.

These fine control operations are all included in the AOTs, and users do not have to concern themselves with them. An IRC observation uses Micro-Scan for dithering. The FIS imaging observations are carried out in Slow-Scan mode in the in-scan direction with the Step-Scan used

Table 3.2.3: Summary of Pointing mode operation (nominal)

Specification of Pointing mode operation	
Total operation time	30 min
Maximum observation time	10 min
Absolute accuracy of pointing	30 arcsec
Cross-scan Offset	±1 deg
Performance	
Pointing Stability[1]	$\leq$ 1 arcsec (peak-to-peak) in 1 minutes

[1] Based on the performance evaluation tests.

to shift the FoV in the cross-scan direction. See the AOT description page of each instrument for more details.

Table 3.2.4: Pointing adjustment during a Pointed observation.

	Amount of shift	Direction	Purpose
Micro-Scan	15–30 arcsec/step	arbitrary	Dithering of IRC imaging
Step-Scan	3–7 arcmin/step	arbitrary	Cross-scan shift of FIS imaging
Slow-Scan	1–15(–30) arcsec/sec	arbitrary	FIS imaging

Use of these operations are defined in the AOT and little room for the observers to change.

The Step-Scan and Micro-Scan will cause a disturbance of the satellite attitude at the level of a few arcsec. Therefore, each exposure has to be started after waiting for the stabilization of the telescope attitude. The IRC waits for notification from the AOCS and then starts an exposure. This waiting time will be a dead time for observers. The dead time for Micro-Scan and Step-Scan operations are typically about 30 sec and 40–50 sec, respectively. It is noted that the actual stabilization time varies depending on the given condition. The Slow-Scan operation needs 30–40 seconds until the scan speed becomes stable after the change.

These dead times are taken into account in the AOTs of the IRC and the corresponding sensitivity estimates. The amplitude of the disturbance is much smaller than the spatial resolution of the FIS. Hence the FIS may simply wait for a certain small amount of time after an operation.

No pointing reconstruction using the Focal-Plane instruments is planned for the pointed observations. The users will receive position information from the G-ADS. Since the source of the pointing uncertainty is the alignment of the telescope and the AOCS, it is expected that the accuracy will be improved as the analysis progresses. The users can refine the position using the data themselves for the IRC imaging observations. It is under discussion if it is feasible to carry out the pointing reconstruction for the FIS scanning observation.

3.3 Mission Phases

The mission lifetime of ASTRO-F, expected to be 550 days, is divided into three observation phases after a performance verification (PV) phase.

Phase 0 (PV Phase) The first two months after the launch are assigned to the PV phase. In this period, a check out of the spacecraft system and the Focal-Plane Instruments will be made, and then the in-flight performance will be evaluated and the initial calibration of the Focal-Plane Instruments will be carried out. Test observations will be performed accordingly.

Phase 1 Approximately the first half year, by which time ASTRO-F will have scanned the entire ecliptic longitude is referred to as Phase 1. In this period, the Large Area Survey Programmes, namely the All-Sky Survey and the NEP / LMC pointing surveys will be carried out with the highest priority. Some Mission Programme observations are also carried out.

Phase 2 This phase will continue until all liquid Helium evaporates ($\sim$300 days for the nominal case). Many pointed observations of Mission Programmes and Open Time proposals will be performed as well as supplemental scan observations to complete the All-Sky Survey. We expect that supplemental survey observations will be especially required and performed near the ecliptic plane, where the scan paths are relatively sparse. Since Phase 2 is expected to last for 10 months, about 2/3 of the sky area will be observed twice in this phase. The regions of second observation opportunity depend on the launch date and can be checked with available visibility maps and visibility tools (see section 3.4).

Phase 3 After the boil-off of the liquid Helium, the mechanical coolers will keep the temperature low enough to observe with the IRC/NIR camera. Phase 3, where only the IRC/NIR camera is operated, will continue until any on-board instruments (the NIR camera itself, mechanical coolers etc.) cease to function.

3.4 Sky Visibility

As noted earlier, the direction of the telescope pointing is always perpendicular to the direction toward the Sun with a flexibility of ±1 deg in the cross-scan direction. Since ASTRO-F is in a polar-orbit, the visibility, defined as the number of scan paths covering a particular sky position, is a strong function of ecliptic latitude. Targets in the ecliptic pole regions are observable on a number of orbits, while targets near the ecliptic plane are visible by ASTRO-F for only two days (29 orbits) in a half year at the most. In addition, visibility is also affected by the SAA (South Atlantic Anomaly; where a large flux of charged particles disturbs the observation when the satellite pass through the region) and the Moon (the moonlight can enter the telescope aperture. The avoidance angle is 33 deg).

Figure 3.4.3 shows the ASTRO-F visibility for Open Time observations from October 24, 2006 to August 21, 2007 (current estimates of Phase 2). The visibility map updated from Observer's Manual Version 3.0 indicates more practical numbers than previously given. The visibility is calculated based on the simulation of observation scheduling. In the calculation, the nominal orbit of the spacecraft, the ±1 deg cross-scan offset operation, Moon avoidance angle, and South Atlantic Anomaly are taken into account. The available resources for Open Time observations are the reserved orbits (6 per 29 orbits) and the orbits that are not used by either the Large Area Surveys (including complementary scans for the All-Sky Survey to satisfy the 2 orbital passes over every point on the sky, the NEP and LMC surveys) or the Mission Programme observations. At every point on a 20 arcmin resolution grid, 50 observations are requested and the number of successfully allocated observations is regarded as the visibility. The data are then smoothed with a 40 arcmin Gaussian to remove over detailed information that may change easily in the real scheduling. The number indicated by the tool is the best estimate of the visibility at present, but **may not necessarily be true in the actual mission operation**.

Observers should understand that opportunities to observe particular objects or fields with ASTRO-F are strictly limited and are a strong function of the visibility.

It is strongly recommended to the observers to check the visibility at each target position. A Web interface visibility check tool is provided, with which the observers can check the visibility either interactively or in a batch file mode.
(http://www.ir.isas.jaxa.jp/ASTRO-F/Observation/vis/otvis/)

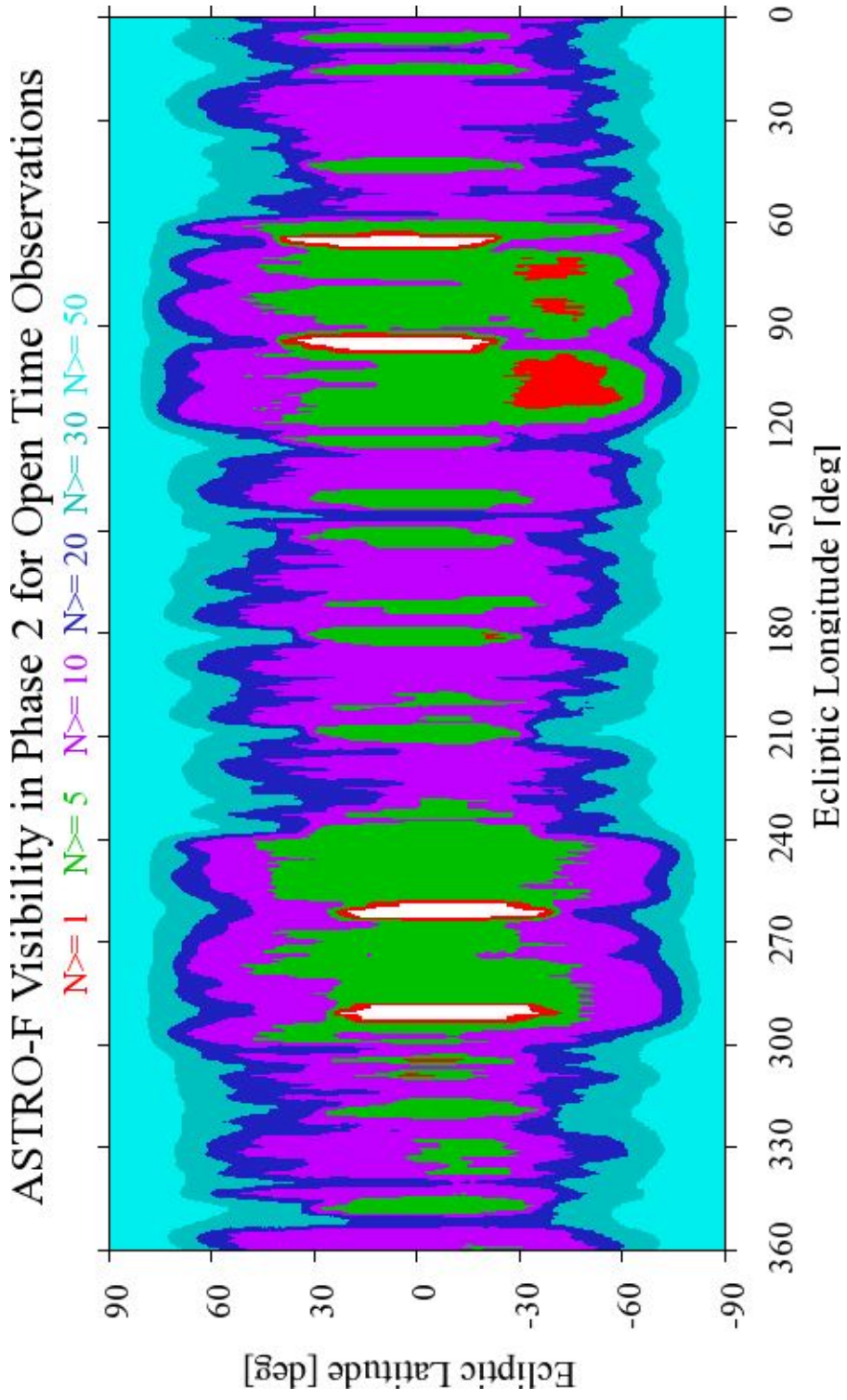

Figure 3.4.3: ASTRO-F Visibility for Open Time Observations during the Phase 2 period (current assumption: from October 24, 2006 to August 21, 2007) in Ecliptic coordinates. The notations are the maximum possible number of observations that can be allocated at any position. In this map, the number given is limited to up to 50 by computational constraints. The calculation was carried out on a 20 arcmin resolution grid which was then smoothed with a 40 arcmin Gaussian to remove over detailed information that may change easily in the real scheduling. The number indicated by the tool is the best estimate of the visibility at present, but may not necessarily be true in the actual mission operation.

[Notes for the Solar System Observation]

Due to the severe visibility constraint, observation planning for Solar System Targets requires additional procedures. The following steps are suggested.

1. Calculate the target position for corresponding observation dates. This can be done with NASA/JPL's HORIZON system (http://ssd.jpl.nasa.gov/cgi-bin/eph) by giving the condition of solar elongation angle as 90 ± 1 deg.

2. Use the original visibility tool (http://www.ir.isas.jaxa.jp/ASTRO-F/Observation/vis/, or follow the link from the Open Time visibility tool page) to check if the target is really visible at that position at that date.

3. Create the Target List with the coordinates. The corresponding observing date has to be given in the comment field of the Target List.

4. Check the visibility again with the Open Time visibility tool.

Chapter 4

FIS: Far-Infrared Surveyor

The FIS is designed primarily to perform the All-Sky Survey in four wavelength bands. The instruments are operated such that data acquisition is continuously made as the telescope scans the sky, resulting in sets of strip data of sky brightness. This operation can also be used for pointed observations in a Slow-Scan mode. The FIS is also equipped with a Fourier Transform Spectrometer (FTS) that enables imaging spectroscopy over the full FIS wavelength range. FTS observations are only made as pointed observations.

4.1 Hardware Specification

4.1.1 Overview

The specifications of the FIS instrument are summarized in Table 4.1.1. It provides four photometric bands between 50 and 180 μm, two broad bands and two narrow bands. Individual detector systems are implemented for the two short and two long wavelength bands, respectively. The FTS covers the entire FIS wavelength range with a resolution of ~ 0.36 cm^{-1} ($R = 450$–150) or ~ 2.4 cm^{-1} ($R = 75$–23).

Table 4.1.1: Hardware Specifications of the Far-Infrared Surveyor (FIS)

Photometric mode				
Band	N60	WIDE-S	WIDE-L	N160
Wavelength Range (μm)[1]	50–80	60–110	110–180	140–180
Central Wavelength (μm)	65	90	140	160
Band Width (μm)[2]	21.7	37.9	52.4	34.1
Detector	Monolithic Ge:Ga[3]		Stressed Ge:Ga	
Array size	20×2	20×3	15×3	15×2
Operational Temperature	~ 2.2 K		~ 2.0 K	
Pixel size (arcsec)[4]	26.8		44.2	
Pixel pitch (arcsec)[4]	29.5		49.1	
Readout	Capacitive Trans-Impedance Amplifier (CTIA)			
Spectroscopic mode				
Spectrometer	Martin-Puplett type Fourier transform spectrometer			
Wavelength (μm)	N/A	60–110	110–180	N/A
Resolution (cm^{-1})	N/A	0.36 / 2.4		N/A

[1] The detector responsivity is higher than 20 per cent of the peak.
[2] As defined by the bandwidth equation below
[3] The SW detector was manufactured by NICT.
[4] The values may change as more accurate telescope parameters become available.

The Central Wavelength is given to be a representative number of the band near the weight center of the band profile. The band width is then defined by the following equation for a flat spectrum, νF_ν =const.

$$\Delta\nu \equiv \frac{\int r(\nu)T(\nu)F_\nu(\nu)d\nu}{r(\nu_c)T(\nu_c)F_\nu(\nu_c)} = \frac{\int r(\nu)T(\nu)d\nu/\nu}{r(\nu_c)T(\nu_c)/\nu_c}. \quad (4.1.1)$$

4.1.2 Optics and Filters

The FIS Optics

Figure 4.1.1 shows the bottom view looking out of the telescope (telescope and the sky are into the page) from the FIS instrument. The light path is indicated by the dash-dotted arrows. Optical elements are labeled. There are three moving parts, a shutter at the light entrance, a filter wheel, and the moving mirror of the FTS. The filter wheel can be rotated to switch between photometric and spectroscopic (FTS) modes. The shutter will be closed occasionally to obtain instrumental dark levels.

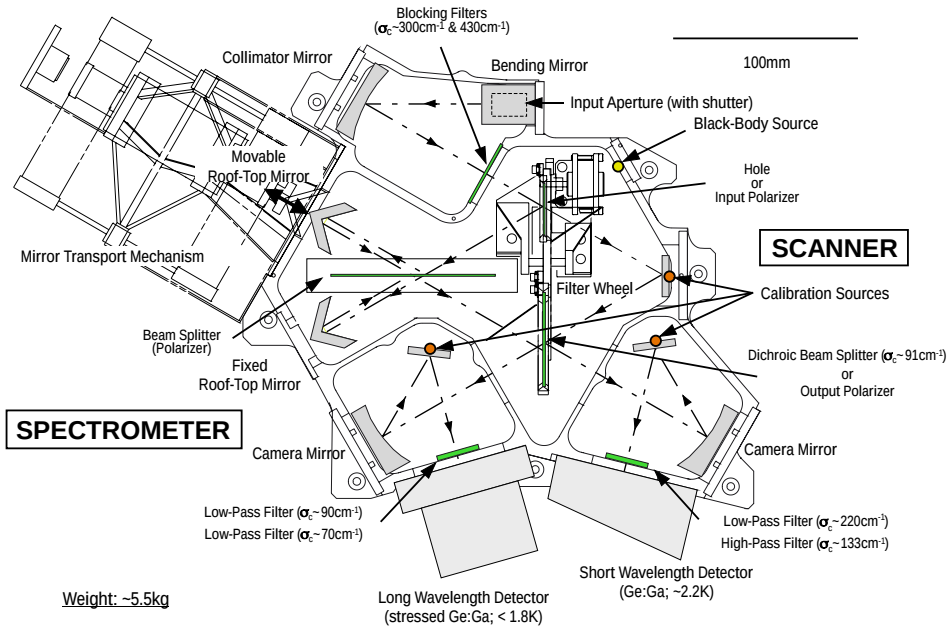

Figure 4.1.1: The optical paths within the FIS. Locations of the calibration lamps are indicated.

Filters and Photometric bands

Figure 4.1.2 describes the filter configuration of the FIS photometric bands. The LW narrow band filter was replaced in 2004 with a new filter with a cut-off at 70 cm^{-1} (143 μm). This extended the band profile shortward and results in better effective responsivity. Following this change, we now denote the longest FIS band as "N160" instead of the previous name N170.

Calibration Lamps

Two sets of calibration lamps are installed in the FIS. The Cal-A system consists of two lamps placed in front of the SW and LW detector arrays. They can be operated individually so that the optimal calibration procedure for each detector array can be realized. An important role of the Cal-A lamp is to produce a pulse flash to simulate the passage of a real point source. The pulse flashes are planned periodically (e.g., every minute) to monitor and correct the time variation of the detector responsivity[1]. Occasionally the lamps are continuously turned on to provide a stable irradiation. In addition, the Cal-B system is a lamp located in the middle of the FIS optical path. Its' light passes through the beam splitter reaching both detector arrays. This Cal-B system will be used as a backup for the Cal-A system. Both of these two sets of

[1]In the current calibration plan the duration of pulse is as long as 0.5 sec

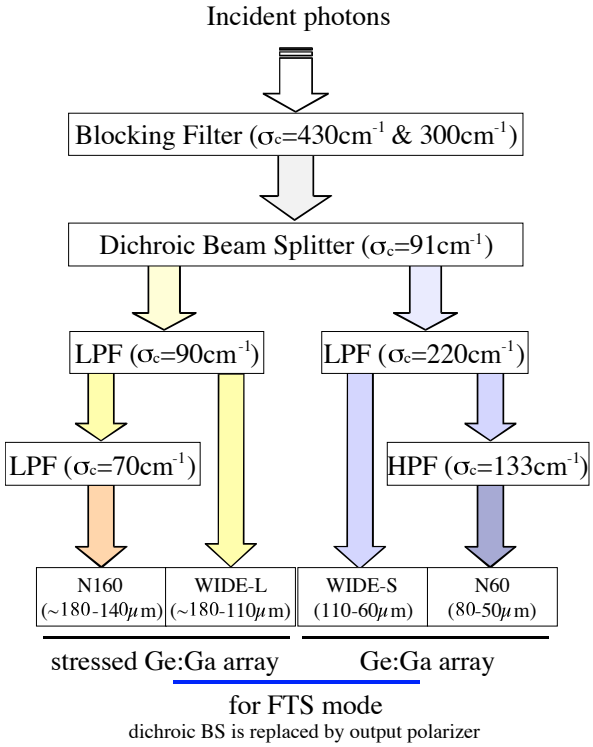

Figure 4.1.2: The filter configuration of the FIS photometric bands. LPF is the Low Pass Filter.

lamps are used solely for monitoring the relative responsivity variation of the detectors. The absolute flux calibration will be made with celestial objects.

In addition to the calibration lamp sets, there is a black body source on the inner wall. It is used for calibration of the FTS.

Shutter

There is a shutter at the entrance aperture of the FIS. The instrumental dark level can be measured by closing the shutter. Leakage at the 1/200 (TBC) level has been observed. During the All-Sky Survey we plan to close the shutter periodically to monitor the dark level.

The internal calibration sequence, calibration lamps and shutter operation for pointed observations are described in the AOTs (Astronomical Observation Templates).

4.1.3 Detector System

Arrays

The FIS has two kinds of detector arrays, a set of two monolithic Ge:Ga arrays[2] for the SW-channel (50–110 μm) and a stressed Ge:Ga array for the LW-channel (110–180 μm). They are operated at $\sim$ 2.2 (SW) and $\sim$ 2.0 (LW) K respectively. Both the SW and LW channels consist of two photometric bands; i.e, the FIS will have four bands in total, which are operated simultaneously in scan mode.

Figure 4.1.3 shows the FIS detector arrays in detail on the Focal-Plane. The upper detectors with three rows are the WIDE-S and WIDE-L bands, and the lower ones with two rows are the N60 and N160 bands. The FIS detector arrays are tilted with respect to the scan direction by 26.5 deg such that the interval between the neighbouring scan paths of the detector pixels is one half of the physical pitch of the pixels. As noted above, the SW and the LW detector arrays observe almost the same area on the sky. The slight difference in the sky coverage is due to the difference of the projected array size.

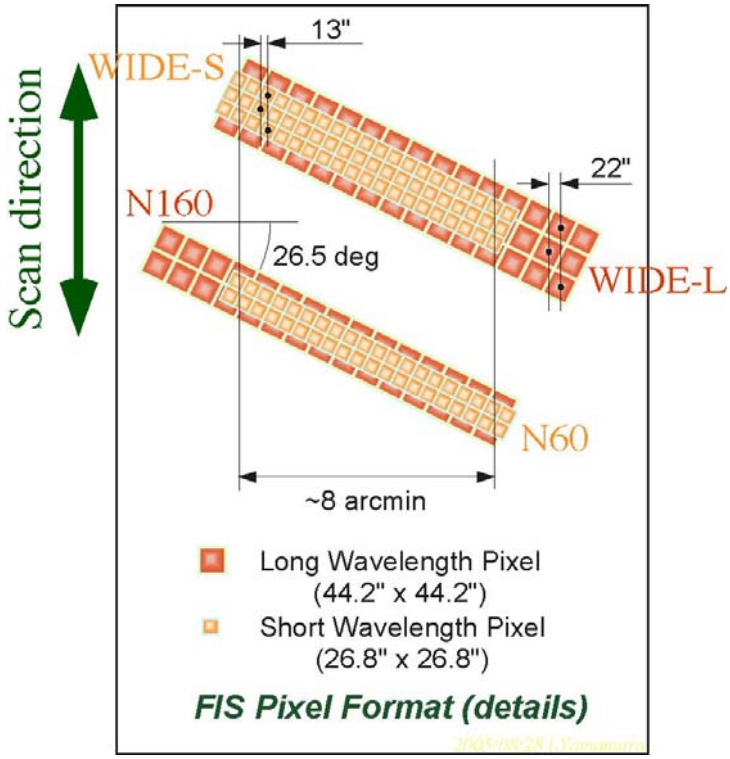

Figure 4.1.3: Focal-Plane layout of the FIS detectors.

Detector Readout Modes

The readout circuit of the FIS is a Capacitive Trans-Impedance Amplifier (CTIA). The signal from each pixel is accumulated in the capacitor as the detector observes far-infrared photons. The voltage at the capacitor is then read out at appropriate intervals. The charge level in the capacitor is periodically reset in order to avoid saturation. The accumulated signal between two resets is called a *Ramp*. Differentiation of the Ramps provides the data that should be proportional to the flux of the incoming radiation. The reset operation of the FIS detectors is

[2]The SW detector was manufactured by NICT.

synchronous, i.e., resets are inserted with a given time interval, regardless of the signal level of each pixel. Although the reset interval is carefully optimized to maximize the instrument performance, bright objects passing through the FIS FoV will possibly cause saturation of the detector signal.

Three different detector readout modes are considered.

Simple sampling mode is the basic operation sequence. Each sampled signal is downlinked to the ground after A/D conversion.

Co-add mode samples the ramps at a higher rate, then the sums of every n samplings are transfered to the ground. This can reduce the noise by a factor of $\sim \sqrt{n}$ while preserving the data size, (n is fixed as 6 in the current design). **This mode will most likely be used in flight unless it has unexpected side effects.** Hereafter we also refer to this mode as the *Nominal mode*.

CDS (Correlated Double Sampling) mode is designed to avoid saturation in very bright regions, such as the inner galactic plane. The detectors are reset at every two samplings, and on board differentiation of these two samplings is retrieved as the signal. Therefore, the downlinked data is already differentiated. **Performance of this readout mode has not been fully assessed. There is a possibility that observers will be asked to change their plan according to the flight performance evaluation.**

Evaluation of the readout sequences has been made during the ground tests, but the final decision will be made during the PV phase. In principle we will use the the same operation mode throughout the survey. However, the possibility of switching the operation mode corresponding to the sky brightness (galactic plane / other sky) has *not* been ruled out.

Bias Light for the LW detectors

The Ge:Ga detectors generally have a strong transient response, i.e. the detector does not respond instantaneously to the incoming flux but rather has a delay of a few – hundreds seconds time scale (see Section 4.2.2). In the All-Sky Survey, a point source passes across a detector pixel in 1/4–1/7 seconds. This is too short for the detectors to reach a steady level corresponding to the source flux. Accordingly the point source sensitivity decreases. This effect is particularly serious for the LW detectors (stressed Ge:Ga detectors), and in the low flux condition (dark sky + weak sources).

In order to reduce the impact of this effect, we decided to add a 'bias light'. This takes the form of a set of thin stainless wires put in front of the LW aperture. During the survey a constant current will be used to give a steady photon flux into the detector array. The point source sensitivity in the All-Sky Survey is expected to recover by a factor of a few with this 'bias light'.

The SW detectors do not require such a mechanism.

4.1.4 The Fourier Transform Spectrometer (FTS)

Note: The FTS mode is available to the Open Time users with several constraints. Users are kindly requested to read the notes in Section 4.2 as well as the Call for Proposals document.

The FIS provides the opportunity for imaging spectroscopy over its full wavelength range (60–180 μm) using the two wide-band arrays (WIDE-S and WIDE-L). The Fourier transform spectrometer of the FIS is of the Martin-Puplett type (Figure 4.1.4). This polarizing type Michelson interferometer uses input and output polarizers to create a linearly polarized beam, and another polarizer to split the beams to a fixed and moving mirror to make the interferogram. The input and output polarizers are mounted on the filter wheel. These polarizers reduce the optical efficiency of the instruments by 1/4 (ideal case) compared to the photometric mode. The total optical efficiency is thus 10–20 per cent. The moving mirror, driven by an electromagnet, can shift ±9.2 mm from its physical center. The optical center (zero path position) is displaced by 4.6 mm from the physical center and the optical path length is asymmetric to the center.

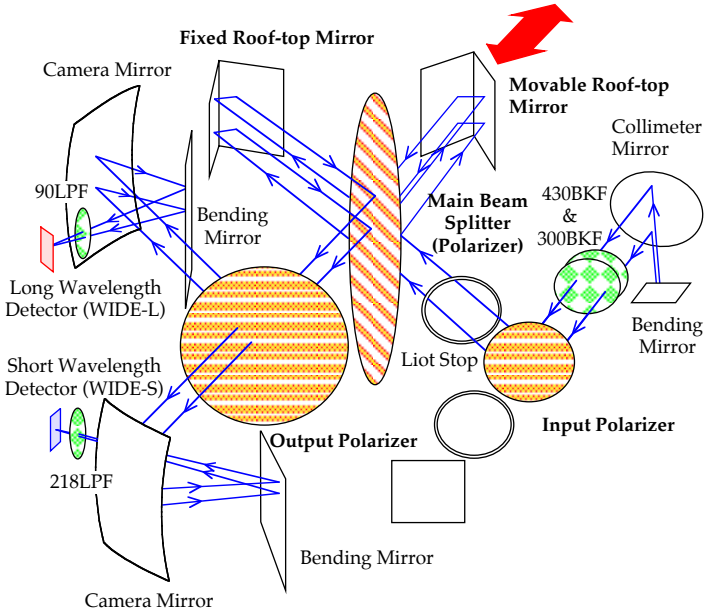

Figure 4.1.4: The optical diagram of the FIS Fourier Transform Spectrometer (FTS).

Two preset operation modes are provided for observers; *Full-resolution mode* and *SED mode* (Figure 4.1.5). They are in principle different only in the mirror scan path length, and accordingly in the resultant spectral resolution. The Full-resolution mode uses the full physical path length, while the SED mode scans ±4.6 mm with respect to the optical center. The mirror moving speed is always a constant 0.38 mm/sec. Taking an interferogram (scanning one-way) takes 48 sec in Full-Resolution mode and 12 sec in SED mode.

The spectral resolution, defined as $1/L$ (L is the optical path length) is about 0.36 cm^{-1} for the Full-Resolution mode and 2.4 cm^{-1} for the SED mode, respectively. Note that these values assume apodization at the spectrum reconstruction. Better spectral resolution may be obtained by optimizing the data reduction procedure. The specification of the FTS mode is summarized in Table 4.1.2.

In FTS mode, the WIDE-S and WIDE-L are operated simultaneously, with a higher sampling rate than in the photometric mode in order to properly sample the interferogram. The narrow band detectors, N60 and N160, are not used.

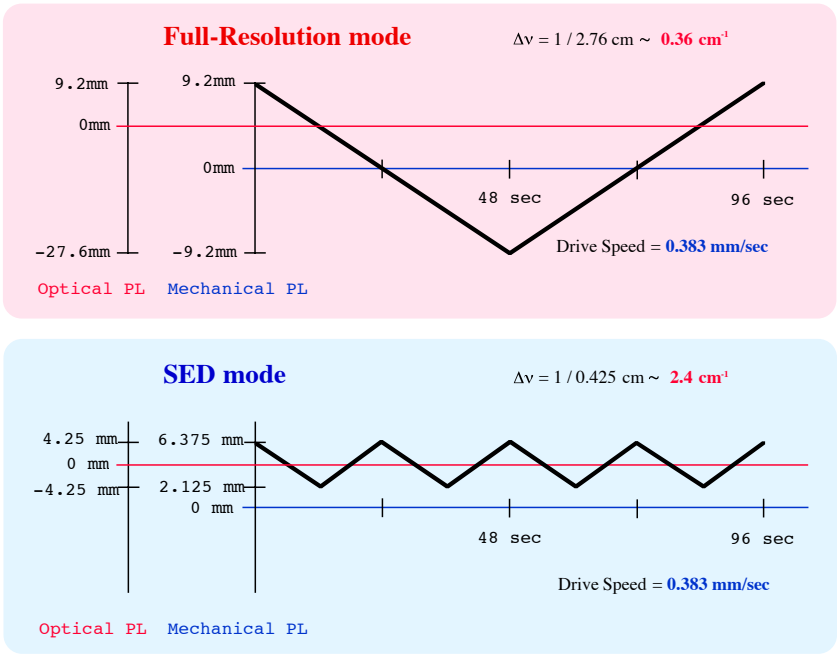

Figure 4.1.5: The mirror driving patterns of the FIS/FTS. There are two modes, *Full-Resolution mode* and *SED mode*.

Table 4.1.2: Specifications of the FIS Fourier Transform Spectrometer (FTS) mode.

Wavelength (μm)	60–110 (WIDE-S), 110–180 (WIDE-L)	
Operation mode	Full-Resolution	SED
Mechanical Path Length (mm)	−9.2–+9.2	+2.1–+6.3
Optical Path Length (mm)	27.6 mm	4.2mm
One scan time (sec)	48	24
Resolution (cm^{-1})	0.36	2.4
Resolution $\lambda/\Delta\lambda$	450–150	75–23

4.1.5 Instrument Operation

The data acquisition process of the FIS is programmed into the hardware sequencer. When an observation is started, a preset specified sequence pattern is repeatedly carried out and the data are packed into telemetry packets and sent to the satellite's main computer (Data Handling Unit: DHU). The data sampling timing is as accurate as the FIS internal clock and is quite stable. Detector level reset and calibration pulse are controlled by the FIS on-board software with an accuracy as good as the readouts. They can alternatively be operated by commands. Open and close of the shutter and continuous irradiation by the calibration lamps are made by commands. The status of the shutter and calibration lamps are all recorded for the data processing.

The survey observation sequence and the AOTs (Astronomical Observation Templates) are designed by combining these elemental operation units. Usually users are not aware of the details of the operation for the preparation of observations. However, such information may be useful for the data reduction.

4.2 Pre-flight performance

The expected performance of the FIS instrument is discussed in this section. The information is derived from the data taken during the FIS single component tests, the FPI evaluation tests in combination with the IRC, and the performance evaluation tests in the flight configuration during 2003–2005. Limitations of the test environment and data analysis mean that some values noted here are still preliminary or have uncertainties. Users should bear this in mind for the observation planning.

4.2.1 Optics

Imaging Quality

It was impossible for the ASTRO-F team to carry out an end-to-end performance test for the telescope and instruments in the cryogenic environment. Therefore, imaging quality through solely the FIS optics was measured. During the laboratory evaluation tests, a pin-hole mask was placed at the focus of the instrument and the light from a blackbody source placed behind was observed. The mask was smoothly moved along the short side of the detector (not titled as in the flight configuration) to simulate the scanning observation. Figure 4.2.6 shows the raw image of the pin-hole passage observed by one of the rows (20 pixels) of the SW detector.

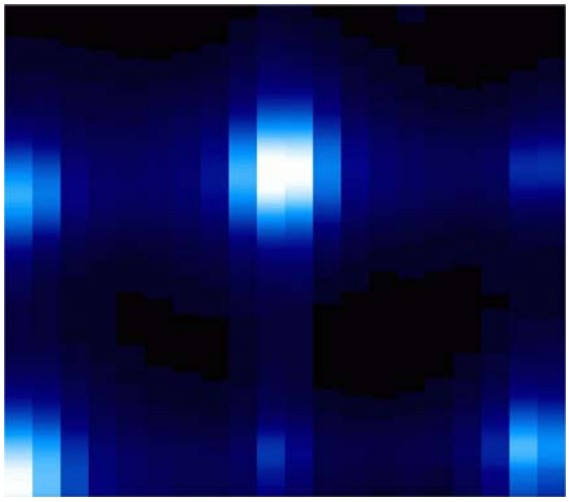

Figure 4.2.6: Pin-hole image observed by the SW detector. Signals from the 20 pixels in one of the five rows are displayed. Each stripe indicates the time profile of the output signal as the pin-hole moves from top to bottom.

The signal profile from a pixel as the pin-hole moves across it is presented in Figure 4.2.7. The profile is very symmetric with respect to the peak. In the SW detector, the width of the observed profile is slightly larger than that expected from the optics. The reason for this difference is not well understood. Possible reasons are (1) cross-talk between the pixels, (2) unknown optical aberration, (3) the mask was slightly off-focus in the test configuration.

The actual PSF of the LW detector is almost consistent with the model calculation.

Careful measurement of the PSF is planned during the PV phase.

Figure 4.2.8 shows the signal change of the LW detector as the pin-hole moves along the detector array. When the image of the hole is located at the Column-3 pixels, the Column-4 pixels also output a signal. The possibility of electrical cross-talk may be ruled out. Concerning optical ghosting, an aperture mask has been added in front of the detector mount to avoid

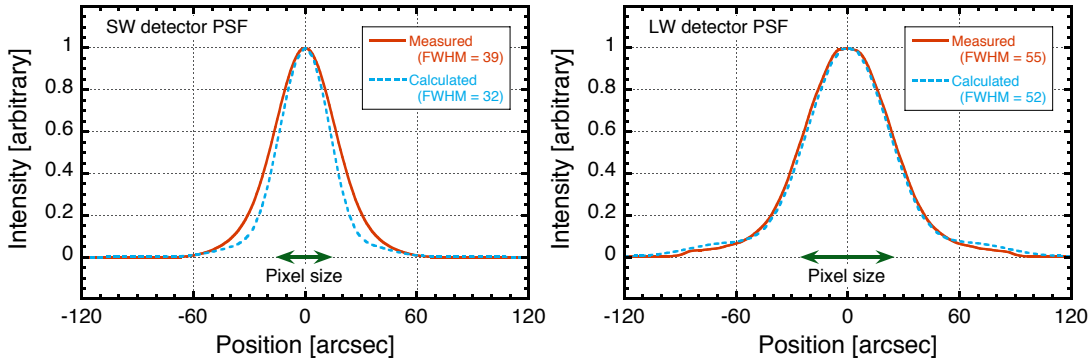

Figure 4.2.7: The signal profile for a pin-hole scan along a pixel in the WIDE-S (left) and WIDE-L (right) array. It is recognized that the observed profile (red) is broader than the expected one from the model (blue). The physical size of the detector pixels is indicated in the plots.

reflection of the light. However, no pin-hole measurements were made after this installation and we will not know whether the ghosting has been successfully removed until we will have the flight data.

The SW array also had a ghosting problem during the component evaluation tests due to the reflection from a part of the arrays themselves. It has been successfully removed by adding an aperture mask in front of the detector arrays to cover the reflective part.

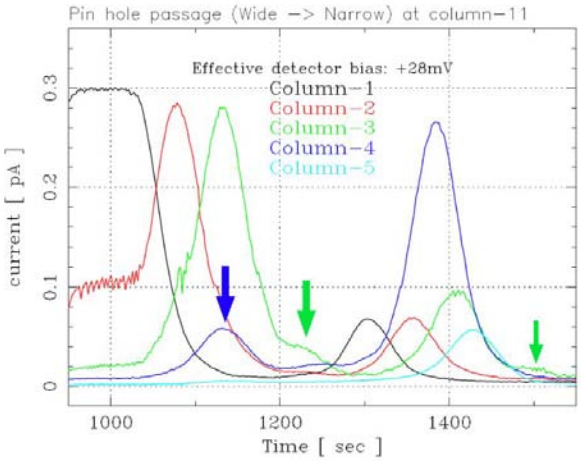

Figure 4.2.8: The detector signal as a pin-hole moves along the detectors from upper-right to lower left in Figure 4.1.3 in parallel to the detector rows. Columns 1,2,3 are the WIDE-L detectors and 4 and 5 are of from N160. Ghosting features are indicated by arrows.

Spectral Responsivity

The relative spectral responsivity of the FIS system is presented in Figure 4.2.9. The responses are normalized at their peaks. The filter transmittance as well as the efficiency of the optical elements, and the detector spectral responsivity are taken into account. The filters and optics were measured in the end-to-end system configuration at room temperature. The narrow band filters for N60 and N160 were measured individually at the cryogenic temperature, since it was known that these filters showed a temperature dependent variation.

The detector spectral responsivity was evaluated using the FTS of the FIS itself, with a blackbody source at different temperatures. Each pixel of the detector shows a different spectral response. This difference is larger in the LW detector, due to the non-uniform effective stress on the detector tips. The plots in Figure 4.2.9 are regarded as the 'typical' profiles. Pixel by pixel profiles are being prepared for the calibration.

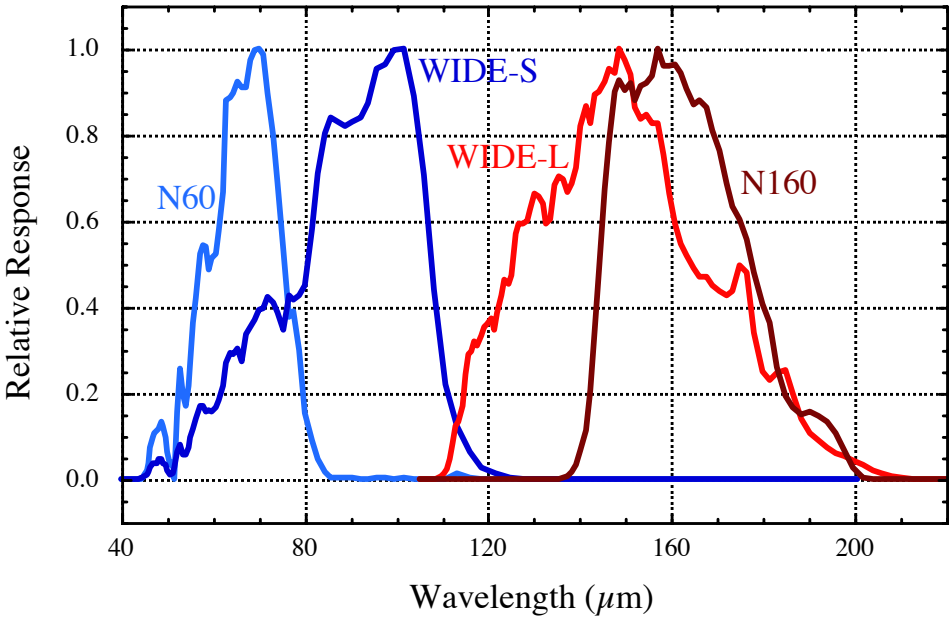

Figure 4.2.9: The spectral response curves of the four FIS photometric bands normalized at the peak of each band. These profiles should be regarded as 'typical' for the bands.

The spectral responsivity data shown in the plots are also available on the ISAS user support web page.

Leakage

A combination of two blocking filters at the entrance aperture are expected to reduce the short wavelength light leakage to factors of 10^{-5} at 10 μm and 10^{-9} at 0.5 μm optimally. However, no end-to-end measurement has been made and the leakage could be as worse as 10^{-5}–10^{-6} at 0.5 μm.

Distortion

Figure 4.2.10 shows the detector shape projected onto the sky. Due to the fact that the FIS aperture entrance is about 20 arcmin away from the center of the focal plane (boresight), and that the FIS optics are an off-axis design, significant distortion of the detector shape is observed (red lines). The shape without optical distortion is also plotted for comparison (blue). The distortion will be further evaluated during the PV phase, and information necessary for the correction will be provided. It is not necessary for observers to take these effects into account in the observation planning.

Polarization

The dichroic beam splitter used in the FIS is known to have polarization. In Figure 4.2.11 the transmittance and reflectivity of the filter is given. The reflection was measured at two different

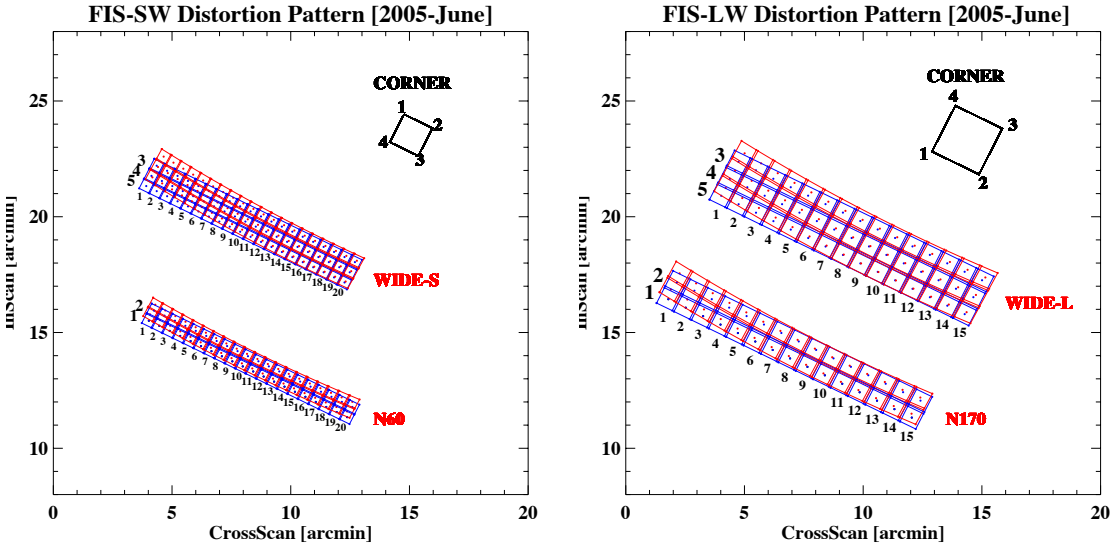

Figure 4.2.10: The FIS detectors projected onto the sky, with (red) and without (blue) optical distortion.

angles perpendicular to each other. A difference in performance at a few specific wavelengths at approximately 160 and 180 cm^{-1} (corresponding to 63 and 55 μm, respectively) was observed. Unfortunately the angle of the filter in the flight module instruments is not accurately known, and this difference will result in an uncertainty in the measurement of the polarized light.

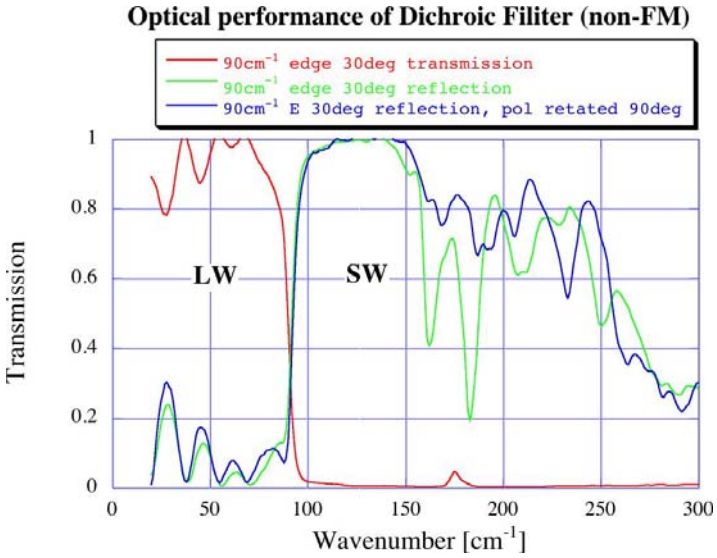

Figure 4.2.11: The reflectivity and transmittance of the dichroic beam splitter. The blue and green curves are the reflectivity in the SW channel side. The two curves deviate around 160 and 180 μm.

4.2.2 Detector system

Dead pixels

The SW- and LW-arrays are known to have 4 and 7 dead pixels, respectively. In addition one SW pixel has a large noise level and an unstable signal output. Figure 4.2.12 shows the positions of the dead and badly performing pixels.

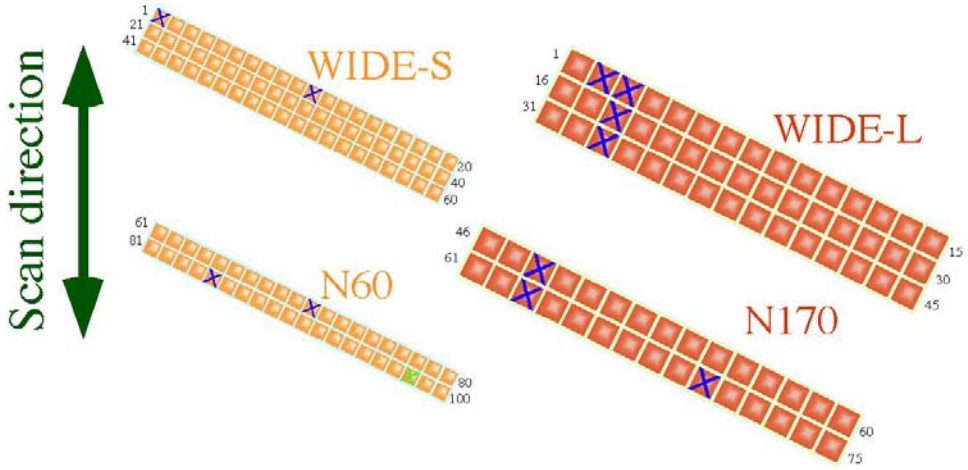

Figure 4.2.12: The positions of dead (blue cross) and badly performing (green cross) pixels in the FIS detector arrays. Definitions of the pixel numbering indices are also presented.

Responsivity and Uniformity

Figure 4.2.13 shows the responsivity of all the SW detector pixels. The values are calculated for a $\nu I\nu$ = constant spectrum at the central wavelength defined in Table 4.1.1. Similar information presented in a different form is shown for the LW detectors (Figure 4.2.14). The variation (1σ) is 25–30 per cent.

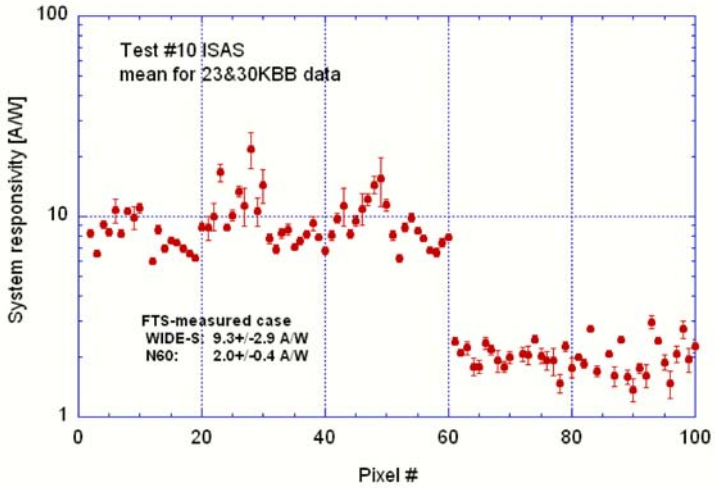

Figure 4.2.13: Responsivities of all pixels in the SW detector arrays. See figure 4.2.12 for the definition of the pixel number.

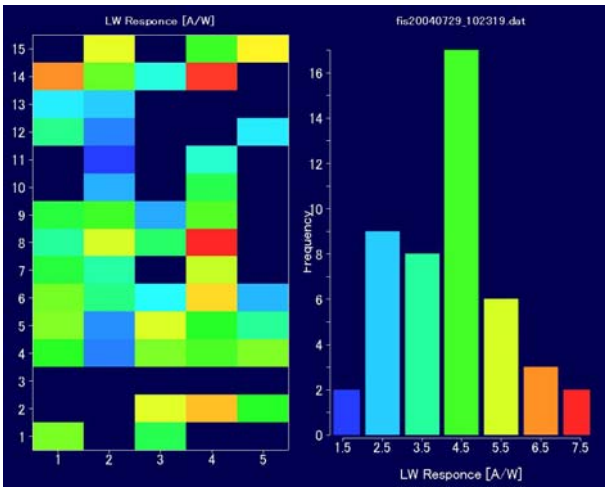

Figure 4.2.14: Pixel by pixel responsivity variation of the LW detector arrays.

Noise

After the results of the early FM performance tests, the FIS introduced two noise filters, the first in the cryogenic part near the detector and the other outside the cryostat. These filters successfully reduced the noise significantly.

There are noise components at specific frequencies in the SW detector (Figure 4.2.15). It is suspected that the components are residuals of electrical interference from the other instruments that could not be removed by the filters. The frequency of the components move as the instrument status changes. The power of these excess components is roughly one half of the total noise power. Attempts to reduce these noise components in the data reduction process are being considered.

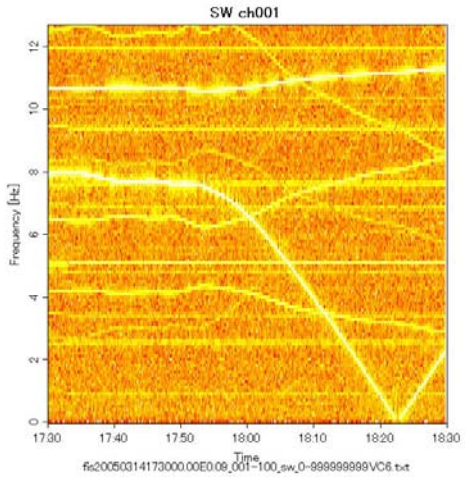

Figure 4.2.15: Noise spectral profile of a SW detector pixel. Time variation of the noise spectra taken during the laboratory test under dark conditions. White stripes are excess noise components. We observe a number of components at specific frequencies. Some of them move with time.

Ramp curve

Ideally the output signal of the FIS detector should be proportional to the number of incoming photons, but this is not the case in reality. The actual ramp curves show deviations from the optimal linear line even when the data is taken under constant incoming radiation. The SW detector shows this effect more prominently (Figure 4.2.16). As the slope of the ramp curve gives the instantaneous flux, any deviation from linearity means that the responsivity changes along a ramp. Currently, the SW ramp curve becomes flatter as an integration progresses. Therefore, if one wishes to observe a faint target, it is more efficient to insert a reset frequently and to use the linear and steep part of the ramps (see Section 4.4.1). The non-linearity of the LW detector is 5–10 per cent.

If the shape of the ramp curve is reproducible, and if the curve is monotonic with incoming flux, it will be possible to correct this effect. We have repeated many tests to check the reproductivity of the ramp curves under various flux /detector conditions. We confirm that the ramp shape is stable at least over a few days time scale if the detector driving parameters and detector temperature remain unchanged. Ramps taken under such conditions can be corrected almost perfectly. However, we also see a large discrepancy over several pixels or under strong radiation. The current correction method results in a residual error of the order of 10 per cent in flux. More studies are needed.

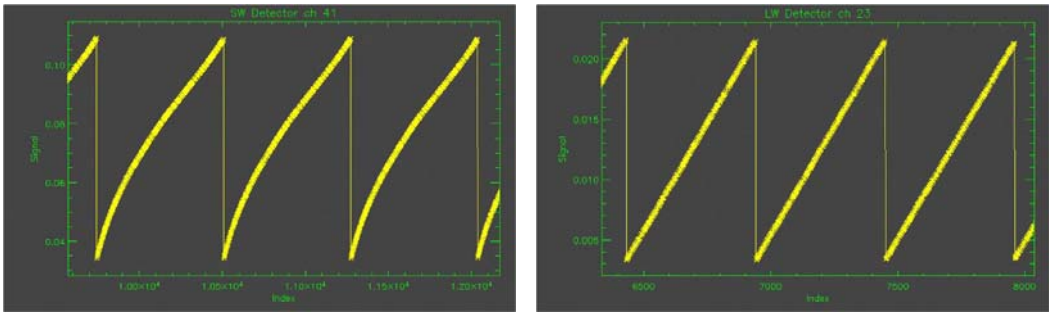

Figure 4.2.16: Comparison of integration ramps under constant irradiation levels. The LW detector (right) shows an almost linear response while the SW signal (left) deviates from linearity as the integration progresses.

Saturation After Effect

It is found that the saturation of the detector is followed by a decrease in the signal level (Figure 4.2.17). This effect is more obvious in the LW channel. The effect appears more significantly when the saturation is heavier. It seems that the effect is already present when the integrated signal has reached about half of the full saturation level. The recovery time scale is of the order of a minute. This effect is still under quantitative analysis.

It is recommended to set the reset interval so as to not cause saturation of the detector, although at the cost of sensitivity. The saturation level given in the following section approximately considers this effect.

Transient response

It is known that the Ge:Ga type detectors show a strong transient response; the detector output signal does not respond instantaneously to a change of incoming flux but rather has a delay of a few – hundreds seconds time scale.

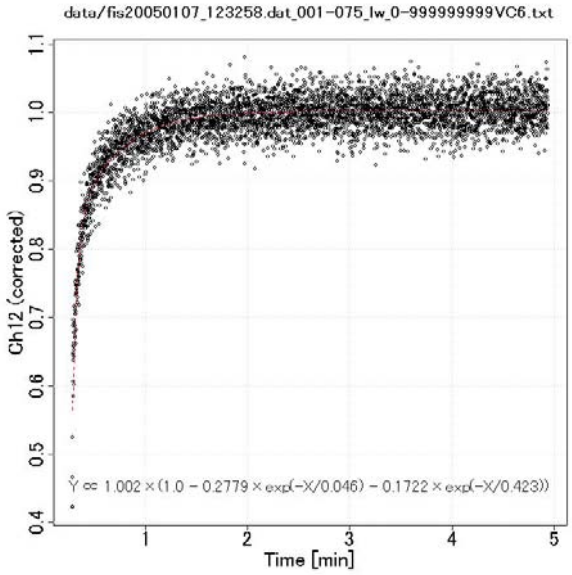

Figure 4.2.17: An example of Saturation after effect for a LW detector pixel. The differential signal for a constant irradiation is plotted against time after the saturation. In this figure an attempt is made to fit the data by a two component exponential function. More detailed analysis is ongoing.

Figure 4.2.18 demonstrates how the transient response of the FIS detectors changes with a step change of incoming flux. In order to simulate the real flight conditions, a calibration lamp is turned on weakly to provide a background level for the SW detector, and a *Bias Light* (Section 4.1.3) is used for the LW array. In both these cases, the time constants are 10–30 sec.

Since the ASTRO-F/FIS almost always observes the sky in scanning mode, an understanding of the effect of the transient response to the observed data is essential. The most extreme case is the All-Sky Survey, in which a point source is scanned in only 0.2–0.4 sec, much smaller than the transient time constant, resulting in a lower output signal than expected by factor of a few (Figure 4.2.19). This also affects the detection limits. The effect is not so severe for the Slow-Scan mode for the pointed observations.

Ideally, the transient response should be understood and reproduced by modeling the charge transfer in the detector element. However, strong non-linear physics prevent us from making a perfect model, although the analysis is continuing. For the All-Sky Survey data, the point source flux is planned to be corrected empirically by tables comparing the signals for the instantaneous and continuous flux levels.

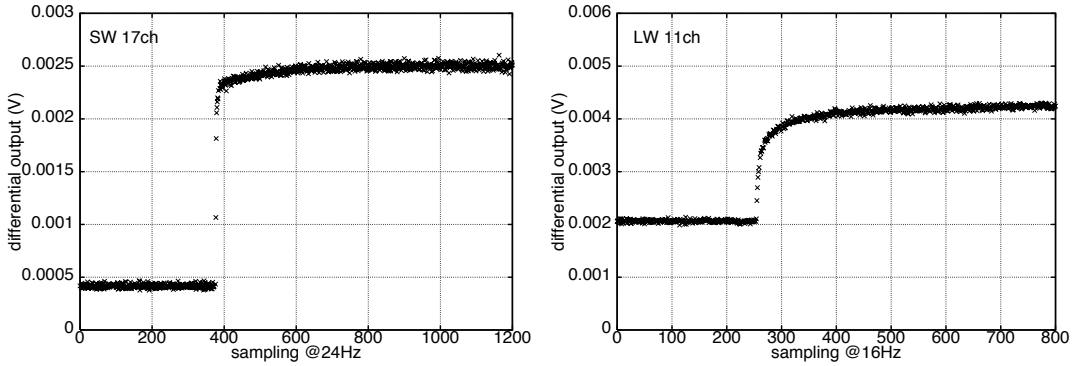

Figure 4.2.18: Examples of transient response for the FIS detectors for a step-wise change of the incident flux.

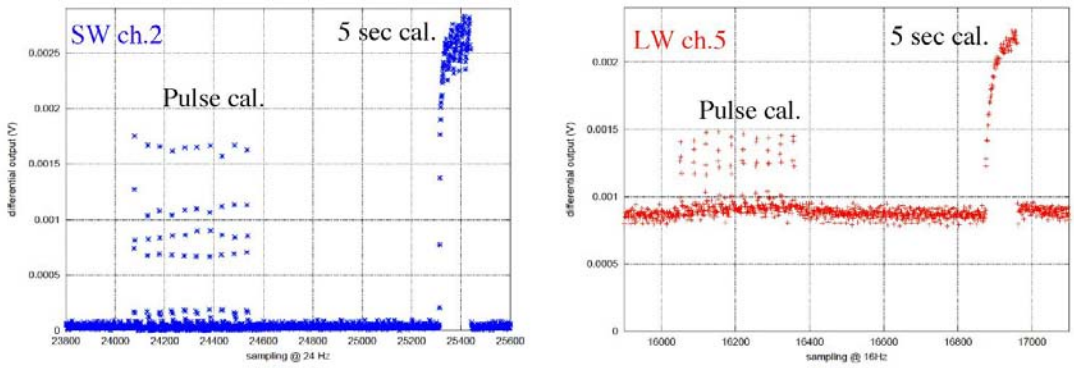

Figure 4.2.19: Transient response to pulse irradiation. On the left side of the each figure the calibration lamps are flashed at very short periods simulating the passage of a point source in the All-Sky Survey. While on the right, the lamps are turned on continuously for 5 sec. The intensity of the calibration lamps was the same for both cases. Although 5 sec is not enough time for the detectors to reach a constant output level, it is obvious that the output signal for flashes is smaller than that of the 5 sec case. This ratio will be used for the flux calibration of point sources.

Cross-talk

Cross-talk between the detector pixels will broaden the effective FWHM of a point source image. Moreover, it will increase the effective number of glitches, and complicate the transient response. This effect may be more serious in the SW detector, which is a monolithic structure. The cross-talk effect for point sources was measured by a pin-hole mask image, as explained in Section 4.2.1. From this measurement, it appears that the non-stationary cross-talk is not significant. The measured FWHM of a point source image is consistent with a cross-talk level of about 20 per cent. However, other explanations cannot yet be ruled out.

So far no clear evidence of cross-talk observed in the LW detectors (Section 4.2.1). More analysis is required to a give clear answer to this phenomenon.

Spectral responsivity

The LW detectors of the FIS are of the stressed Ge:Ga type. The stronger the stress (pressure) on the detector element, the longer the wavelength limit can be extended. It is observed that the cut-off wavelength (the longest wavelength at which the detector is sensitive) varies from one pixel to another, probably because of inhomogeneous stress among the pixels. Figure 4.2.20 demonstrates the pixel by pixel variation of the spectral responsivity of the LW channel. It is seen that the cut-off wavelength ranges from 165–185 μm. The N160 band extends longer than the WIDE-L band as the detectors are under even higher pressure.

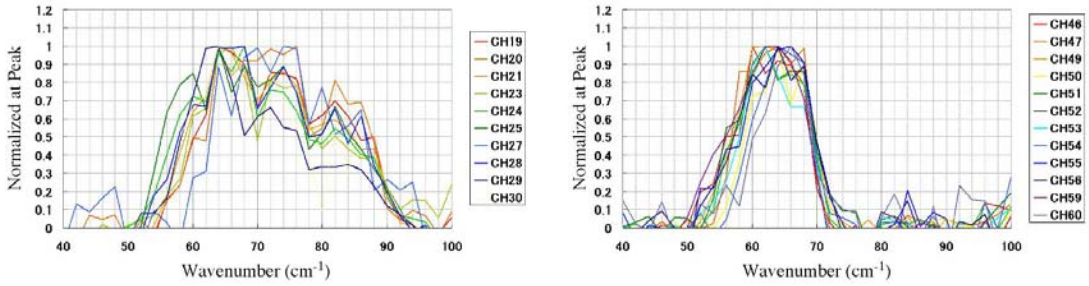

Figure 4.2.20: Pixel by pixel variation of the spectral response of the LW detector.

The difference in wavelength profile directly influences the photometric accuracy, especially for cool targets such as molecular clouds. The error in photometry is less than a few per cent for sources warmer than 100 K, but is more than 10 per cent for a target of 30 K.

4.2.3 FTS mode

Technically, the FTS mode of the FIS is very challenging. In addition to the various instrumental behaviors noted earlier, there are more issues to be considered. Observers who are considering observations with the FTS mode should carefully read the following notes and investigate if their observations are feasible with the instrument. Please note that according to the performance measured during the PV phase, there remains the possibility that observations with this mode may be canceled.

Transient Effects on the FTS data

In the FTS mode, the detectors have to observe a rapidly changing signal from the interferogram. Naturally, strong transient effects appear in the output signal. Figure 4.2.21 plots the interferograms corresponding to the *forward* and *backward* motion of the mirror. Large deviations are seen.

For the moment we do not have perfect correction methods for the transients, and the correction of this effect is rather empirical. It is known that the strength and time constant of the transient effect is a function of the irradiating flux level. Therefore, we first observe the internal calibration lamp whose SED is known. The brightness of the lamp is adjusted to that of the target. The data from the calibration lamp is reduced without transient correction. By comparing the results and the black body spectrum of the lamp in the calibration data, we can derive a correction factor between the observed and "true" spectrum. This correction factor is then applied to the target spectrum.

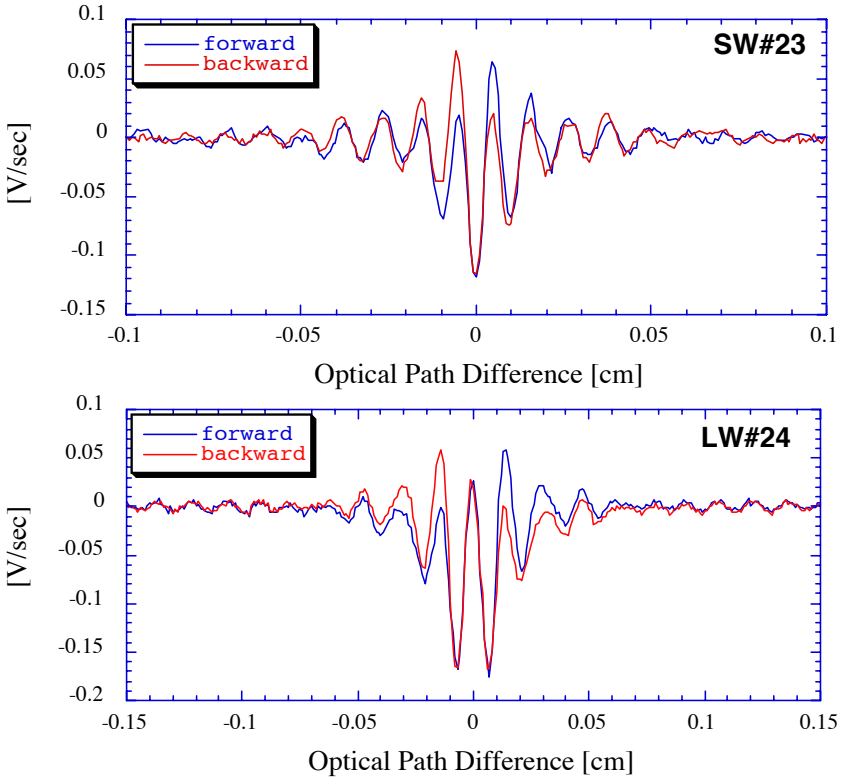

Figure 4.2.21: Comparison of forward (blue) and backward (red) interferograms. The difference between the two interferograms is thought to be due to detector transients.

Detector Response Inhomogeneity

As described above, pixels in the detector arrays do not have a uniform responsivity. Figure 4.2.22 indicates the relative responsivity variation of the detector pixels in FTS mode at different wavelengths. The majority of the pixels are within 20 per cent (SW) and 50 per cent (LW) of each other. There are several pixels with extremely high responsivity; namely pixel 23 (and several nearby ones) of the SW and pixel 31 of the LW array. These high responsivity pixels are used to estimate the initial center of the interferogram.

In addition to the responsivity variation, there is variation in the wavelength profile (long wavelength cut-off) in the LW detectors.

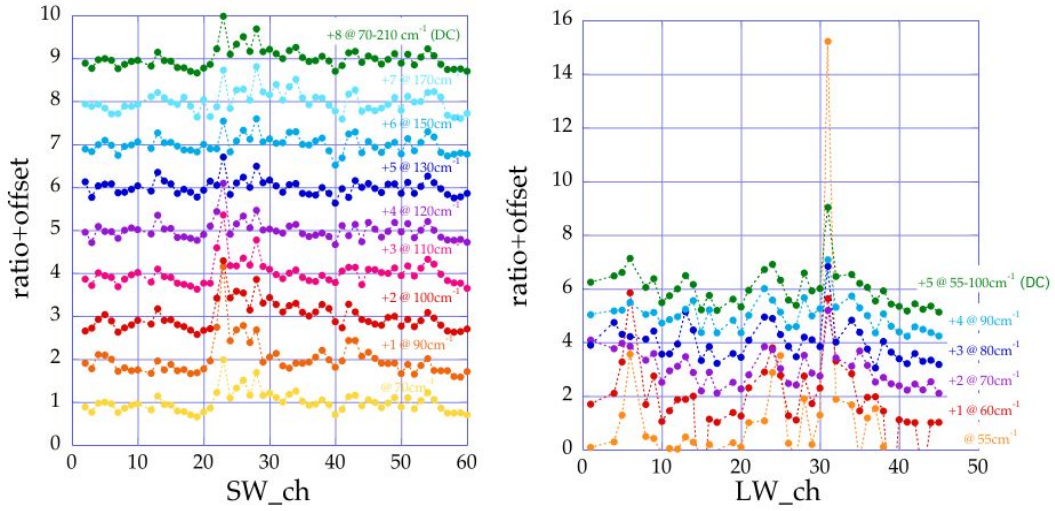

Figure 4.2.22: The pixel by pixel variation of detector response in FTS mode. There are a few pixels showing significantly high values.

Spectrum Reproductivity

In order to evaluate the stability of the spectroscopic data, three spectra were taken during the laboratory tests. The first two were taken with a one hour interval, then the third one was obtained after three hours. These were independently reduced and are overlaid in Figure 4.2.23. Although the spectra of the SW channel show large amplitude fringes, we see that the three spectra are almost equivalent to each other to within about 10 per cent.

Note that these spectra were taken one after the other in a continuous test session. It has not yet been evaluated whether the same result holds true for the spectra taken between long intervals or after turbulence (e.g., SAA).

Fringes

The SW channel suffers from strong fringes in the spectra. Figure 4.2.24 shows an enlargement of the fringe patterns in the Full-Resolution mode and the SED mode respectively. The cause of the fringes is thought to be a reflection within the detector element, by the parallel surface of the chip (therefore it should also present in the photometric mode). Throughout the laboratory measurements, the fringe pattern remains at the same position, implying that it can be easily removed. However, it is not clear whether this will hold for the flight data, especially for point sources. Observations of sharp lines on the fringe shoulders will require special care.

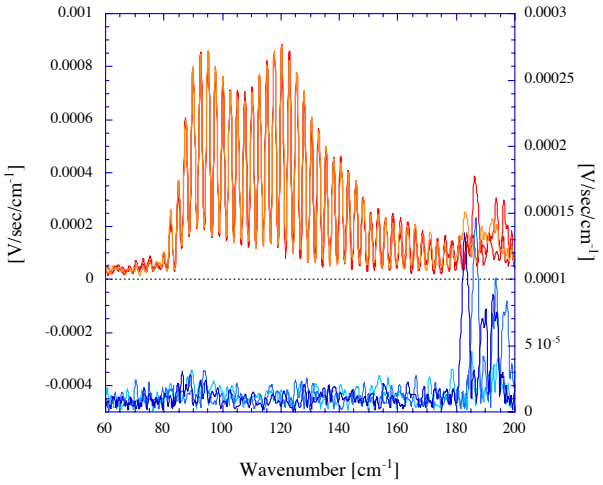

Figure 4.2.23: Three FTS spectra taken one and three hours after the initial spectrum are overlaid. They are almost equivalent. The bottom plot is the difference between the spectra. It is seen that the difference looks random but is within about 10 per cent. The large deviations beyond 180 cm^{-1} are due to excess noise.

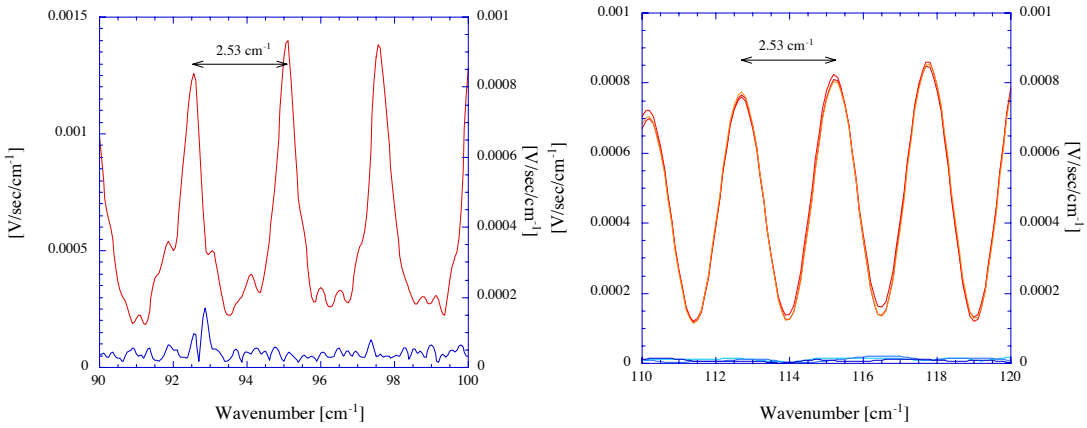

Figure 4.2.24: Fringe pattern of the FTS spectra in Full-Resolution mode (left) and SED mode (right). In Full-Resolution mode, the fringe pattern is resolved out and an "Airy pattern" of the Fabry-Perot interference is clearly seen.The blue lines in the bottom panel are the rms noise level. The three lines in the right panel are different measurements, and match each other indicating that the fringe pattern is well repeated.

Interference from the Cryocooler

It is known that the vibration from the cryocooler interferes the FTS mirror drive. The vibration appears as a change of the mirror scan speed of up to 50 per cent, periodically with a frequency of 15 Hz. As the detector readout is at a constant frequency, this means that the sampling of the interferogram is at inhomogeneous intervals of the optical path. As the results the FFT technique cannot be applied. It may also have an effect on the transient behaviour and change the observed spectra. No clear influence on the resultant spectra has been observed at this stage of the data analysis.

4.3 The FIS All-Sky Survey

The FIS is designed primarily to perform the All-Sky Survey in 4 photometric bands at wavelengths of 50–180 μm. The goal is to observe the entire sky on at least two independent orbits. Although most of Phase 1 will be dedicated to observing time for the All-Sky Survey, supplemental survey operations will also be needed in Phase 2 to fill in the gaps remaining from Phase 1. A dedicated team within the ASTRO-F Project will handle all responsibility for the operation and the data reduction of the FIS All-Sky Survey. Products will be distributed to the science users. (see Section 6).

4.3.1 Operation

During the survey, the detectors are readout continuously with a constant sampling rate for each array. At a fixed interval (TBD, ~ 2 seconds) the detectors are reset. Pulse flashes of the calibration lamps are inserted periodically every 1 minute while keeping the shutter open in order to monitor the detector responsivity. About twice per orbit as well as before and after pointed observations, the shutter is closed to measure the dark level, and the calibration lamp is turned on continuously to monitor the detector responsivity in its steady state. The time constants of the above sequence will be adjusted during the PV phase. The resets and calibration operations will obviously cause gaps in the scanning data.

4.3.2 Expected Performance

Detection Limits

Table 4.3.3 tabulates the 5σ detection limits of the FIS survey for point sources and diffuse radiation. The estimates are based on the simulation of Jeong et al. (2003) that assumed rather ideal conditions.

The numbers are for a single scan with the detector array (not per pixel). Two readout modes, namely Nominal and CDS modes (see Section 4.1.3) are considered. **Note that the performance of the CDS mode has not yet been fully confirmed.**

The estimates of sensitivity are based on the latest information of the detector performance and the optical efficiency. Known detector characteristics, such as noise levels, responsivity, dark current, transient effects, spectral response, expected effects of charged particle hits, etc., as well as the optical efficiency are taken into account. The numbers should be treated as the best estimates of the FIS sensitivity, however, there may still be uncertainty of up to a factor of a few. Time variation of the detector responsivity and noise are not accurately included. Pixel by pixel variation of the sensitivity is as much as a factor of two. In particular, it is noted that the long-wavelength cut-off of the LW detector is different for different pixels, due to inhomogeneous stress on the array. This means that the pixel by pixel relative responsivity changes as a function of the SED of a target.

The LW detector has a very long time constant for the transient response, which results in a lower sensitivity in the survey operation (see Section 4.2.2). The effect of the bias light has already been taken into account in the table, but not fully confirmed.

It is possible that the high redundancy of data taken at high ecliptic latitude regions will improve the detection limits if the data is suitably processed. Such a process will be applied for the generation of the *Faint Source Catalogue*. The *Bright Source Catalogue* is constructed from individual scans and the sensitivities in this table should be adopted.

Table 4.3.3: The FIS All-Sky Survey 5σ detection limits per single scan.

	Point Source (mJy)	Diffuse Source (MJy/sr)
N60	1000	20
WIDE-S	200	4
WIDE-L	400	2
N160	800	4

The actual detection limits at the longer wavelengths may be dominated by the sky confusion. Sky confusion is not considered in the current sensitivity estimates. The observers are suggested to refer to Appendix A for discussions of the the sky confusion. An independent estimate can be found on the Observer Support page of the ISAS Web page (in Japanese).

Saturation Limits

Since the FIS detectors use charge integrating type circuits for data acquisition, the detector signal will saturate when the accumulated charge between resets reaches a certain limit. This means that the saturation does not take place spontaneously by a single bright source but depends on the brightness distribution along the entire scan path between resets. Once the detector saturates, all the information in that detector is lost until next reset. Impacts of charged particles could also cause saturation (Section 4.4.6).

Table 4.3.4 gives the saturation level of the FIS All-Sky Survey. The point source saturation limit is defined as where the ramp curve reaches a level where the reproductivity of the ramp

curve shape becomes bad (e.g., more than 10 per cent) by a point source passage. The diffuse saturation level is determined as where the ramp reaches the same level in a 2 sec integration.

Table 4.3.4: The FIS All-Sky Survey saturation limits.

Band	Point source (Jy)	Diffuse Source (GJy/sr)
N60	500	1.0
WIDE-S	100	0.2
WIDE-L	100	0.1
N160	300	0.5

Our simulation (Jeong et al. internal report) concludes that with a 2 sec reset interval, about 2 per cent of the sky will be lost to saturation. These areas will be mostly on the inner galactic plane. Use of a shorter reset interval or the CDS mode is under consideration for these areas.

4.4 The FIS Pointed Observations: AOTs

4.4.1 FIS01: Photometry / Mapping of Small Area

The **FIS01** AOT is designed for photometry of point sources and/or mapping of small areas up to $\sim 25 \times 10$ arcmin^2.

Table 4.4.5: FIS01 summary.

Fixed parameters	
Observing Mode	Photometry
Band	N60, WIDE-S, WIDE-L, N160
Scan pattern	Two round-trip scans with a cross-scan shift
User defined parameters	
Sampling mode	Nominal or CDS
Reset interval	0.5 or 1 or 2 sec (for Nominal sampling mode)
Slow-Scan speed	8 or 15 arcsec/sec
Shift length	70 or 240 arcsec

[Instrument Operation]
The instrument is operated in the photometry/imaging mode; all four FIS photometric bands (N60, WIDE-S, WIDE-L, N160) retrieve data. The detector operation parameters are fixed at the recommended values provided by the instrument team. Users can specify only two parameters; the readout mode (Nominal / CDS) and if the Nominal mode is selected, the reset interval.

[Scan Operation]
An observation consists of two sets of round-trip scans in the in-scan direction with a shift in the cross-scan direction. The round trip scan is mandatory to ensure data redundancy. The cross-scan shift is used to increase the redundancy or to observe a wider area of the sky. The scan speed is either 8 or 15 arcsec/sec. These speeds are selected to maximize the performance (sensitivity) while enabling observations of a certain size area of sky.

[User specified parameters]
The following inputs can be given by the observer.

Detector readout mode (Nominal / CDS) CDS mode should only be used for the brightest targets that would normally saturate the detector in Nominal mode. See Section 4.1.3 for the details of the readout methods, and Sections 4.4.2 for the sensitivity and saturation levels.

Reset interval This parameter is only relevant for the Nominal readout mode and is chosen based on the brightness of the targets. Generally, a long reset interval improves sensitivity in the amplifier but at the same time increases the risk of saturation (please be reminded that once a detector is saturated all information until the next reset is lost, and that the saturation can also be caused by charged particles). On the other hand, a shorter reset looses more data points at the resets. For the SW detectors, intervals longer than two seconds are not recommended even for faint sources since the responsivity drops due

to nonlinear effects. Here we present three choices for the reset interval in Table 4.4.5. Shorter (0.25 sec) and longer (4 or 8 sec, only for the LW channel) reset intervals may be added after performance evaluation during the PV phase.

By default, the SW and LW detectors (i.e., all four FIS bands) are always reset simultaneously. As the SW detector has a tighter constraint on the reset interval because of its non-linearity, we recommend the following procedure to decide the reset interval.

1. In the case of a faint target where sensitivity is important, look at Table 4.4.9 and pick the reset interval such that the target flux does not exceed the limit. As the same reset interval has to be applied to both the WIDE-S and N60, the numbers for the WIDE-S band, are usually sufficient.
2. If the target is bright and sensitivity is not essential, consult Table 4.4.8 and choose the reset interval such that the target flux does not exceed the saturation limits for any of the four FIS bands.
3. For very bright sources consider CDS mode. However, this readout mode is not yet fully verified, and may have a large flux uncertainty. A decision will be made in the PV phase.

Scan parameters Two numbers have to be given to define the scan pattern; A scan-speed and a cross-scan shift length. A scan-speed of 8 arcsec/sec balances depth and sensitivity with scan area for data redundancy and is recommended for photometry of small numbers of sources. A higher scan speed of 15 arcsec/sec is used to observe larger areas to a slightly shallower sensitivity.

A cross-scan shift length of 70 arcsec is prepared for point source photometry, and 240 arcsec for small area mapping. In the latter case, it is expected that the observation will be repeated on the successive orbit to extend the mapping area, with enough overlap to ensure redundancy.

A round trip scan takes approximately $t_{scan} = (l/s + t_{acc}) \times 2$ seconds where l is the scan length in arcsec, s is the scan speed and t_{acc} is the time needed for scan acceleration. t_{acc} is roughly 30 sec (8 arcsec/sec) and 40 sec (15 arcsec/sec). Deadtime for a cross-scan shift is roughly estimated as 35 sec for a 70 arcsec shift and 45 sec for 240 arcsec shift (see Section 3.2.2 for details). As the total observing time for a pointing opportunity is limited to 10 minutes, the scan length is uniquely determined once the scan speed and shift length are set. Table 4.4.6 shows approximate scan lengths and corresponding observation efficiencies for combinations of scan speed and cross-scan shift lengths. These values will be updated when more accurate numbers for the dead time become available. Data are also retrieved during the acceleration. These data may be usable but it has yet to be confirmed.

Target position The satellite is operated such that the target position is located at the center of the scanned area.

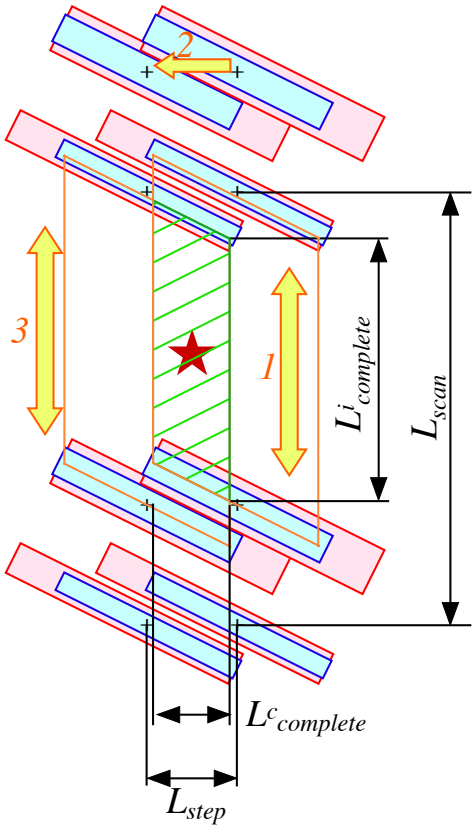

Figure 4.4.25: The scan sequence of the AOT FIS01. (1) First round-trip scan, (2) Step-Scan, (3) Second round-trip scan. The area indicated by the green hatch is scanned four times (two round-trips) by all four detector arrays with more than two pixels of each array. The area inside the orange line is scanned by four bands at least twice (one round-trip). The dimensions in the figure are given in table 4.4.6 for each scan parameter set.

Table 4.4.6: Approximate estimates of scan lengths for different scan parameter in FIS01.

(1) Scan speed (arcsec/sec)	(2) $L_{\rm step}$ (arcsec)	(3) $L_{\rm scan}$ (arcsec)	(4) $L^{\rm i}_{\rm complete}$ (arcsec)	(5) $L^{\rm c}_{\rm complete}$ (arcsec)	(6) Efficiency
8	70	890	580	420	0.74
8	240	870	560	240	0.73
15	70	1520	1210	420	0.68
15	240	1480	1170	240	0.66

(1)(2) Scan parameters.
(3) Scan length with a steady speed.
(4) Scan length observed by all four detector arrays with more than two pixels per band.
(5) Cross-scan length observed by both first and second round-trip scans.
(6) Fraction of time used for taking usable data to the total observing time (600 sec).

4.4.2 Expected Performance of FIS01

Detection Limits

As we explained in Section 4.4, photometry (imaging) observations by the FIS in pointed observation mode is always carried out with the Slow-Scan operation. Therefore the estimates in this section are given by scaling the All-Sky Survey detection limits by some factors which are functions of the scan speed. However, because of the nonlinear responsivity, transient effects, and other complicated characteristics of the instruments, the scaling law is not always straightforward. Table 4.4.7 lists the sensitivities for the two scan speeds, 8 and 15 arcsec/sec, used for the AOTs. Note that confusion is not included in these estimates.

The numbers in the table are for a single scan. Therefore one can imagine that four scans in FIS01 should improve the detection limit by factor of 2. On the other hand, this redundancy can alternatively be used to increase the reliability of the results. In such a case, the detection limit remain unchanged. We leave this at the discretion of the user. As the "standard" rule of thumb, we propose to apply the numbers per one round-trip scan. So for FIS01, which carries out two round trips, a sensitivity of $1/\sqrt{2}$ of the value in the table can be assumed.

Table 4.4.7: The 5σ detection limits for AOT FIS01. Numbers are per scan. See text for details.

Point Source (mJy)								
Scan speed	8 arcsec/sec				15 arcsec/sec			
Reset	0.5 sec	1.0 sec	2.0 sec	CDS	0.5 sec	1.0 sec	2.0 sec	CDS
N60	90	60	45	1600	140	100	70	2500
WIDE-S	18	12	9	320	28	20	14	500
WIDE-L	24	12	6	460	36	18	9	700
N160	48	24	12	920	72	36	18	1400
Diffuse Source (MJy/sr)								
Scan speed	8 arcsec/sec				15 arcsec/sec			
Reset	0.5 sec	1.0 sec	2.0 sec	CDS	0.5 sec	1.0 sec	2.0 sec	CDS
N60	2	1.5	1	40	3	2	1.5	50
WIDE-S	0.4	0.3	0.2	8	0.6	0.4	0.3	10
WIDE-L	0.18	0.09	0.04	2.5	0.24	0.12	0.06	3.5
N160	0.36	0.18	0.08	5.0	0.48	0.24	0.12	7

Saturation Limits

Table 4.4.8 gives the saturation levels for the AOTs FIS01 and FIS02. The saturation limits are functions of the reset interval only. These limits are defined such that the integration ramps of the high sensitivity pixels reach a level where the reproductivity of the ramp shape becomes bad. Beyond this level we still obtain data from the lower-sensitivity pixels but photometric accuracy and quality of reconstructed image map may be significantly degraded.

Linearity Limits

The linearity limit is only relevant for the SW detector which shows a large non-linearity in the integration ramp. The limits are defined such that the ramp reaches to the level where the slope (i.e. sensitivity) becomes approximately half of the value at the beginning of the ramp. It is recommended to carry out any observations below this limit for efficient measurement of faint sources.

Table 4.4.8: The saturation limits for FIS01 and FIS02. See text for details.

Point Source (Jy)				
Reset (sec)	0.5	1.0	2.0	CDS
N60	280	140	70	3600
WIDE-S	60	30	15	700
WIDE-L	120	50	15	1500
N160	300	130	60	3500
Diffuse Source (GJy/sr)				
Reset (sec)	0.5	1.0	2.0	CDS
N60	4.0	2.0	1.0	50
WIDE-S	0.8	0.4	0.2	10
WIDE-L	1.0	0.42	0.12	13
N160	2.5	1.10	0.5	30

Table 4.4.9: The linearity limits for the SW detectors for FIS01 and FIS02.

Point Source (Jy)			
Reset (sec)	0.5	1.0	2.0
N60	60	30	15
WIDE-S	13	6	3
Diffuse Source (GJy/sr)			
Reset (sec)	0.5	1.0	2.0
N60	0.9	0.4	0.2
WIDE-S	0.2	0.1	0.05

4.4.3 FIS02: Mapping of large area

The **FIS02** AOT is designed for mapping of relatively large areas. An observation covers a long strip of ~ 1 degree.

Table 4.4.10: FIS02 summary.

Fixed parameters	
Observing Mode	Photometry
Band	N60, WIDE-S, WIDE-L, N160
Slow-Scan speed	15 or 30 arcsec / sec
Scan pattern	One round trip scan
User defined parameters	
Sampling mode	Nominal* or CDS
Reset interval	0.5 or 1.0 or 2.0 sec
Slow-Scan speed	15 or 30 arcsec/sec

* = Co-add mode

[Instrument operation]
The operation of the instrument with this AOT is the same as FIS01, except that FIS02 carries out a single round-trip only, and that the choice of scan speed is 15 or 30 arcsec/sec. [3]

[Scan operation]
The difference of this AOT from FIS01 is that an observation consists of only a single round-trip scan. The scan speed is chosen from 15 or 30 arcsec/sec. Unlike FIS01, no cross-scan shift is operated during a pointed observation in order to maximize the scan length. It is expected that an adjacent area of the sky will be observed on a successive (or later) orbit. It is strongly recommended to observe the same area of the sky at least twice with different pointing opportunities (i.e. total two round trips at any point) to acquire enough redundancy. It is the observer's responsibility to allocate the scans to cover the required area and/or to obtain the redundancy. With the currently assumed deadtime for acceleration, the scan length is approximately 1 and 2 deg. depending on the scan speed.

[User specified parameters]
The following inputs have to be given by the observer.

Detector readout mode (Nominal / CDS) Same as FIS01.

Reset interval Same as FIS01. See section 4.4.2 and 4.4.2 for the sensitivity and saturation levels.

Target position The satellite is operated such that the target position is located at the beginning of the scan strip.

[3] 30 arcsec/sec is a new addition for Open Time observations

4.4.4 Expected Performance of FIS02

Detection Limits

Table 4.4.11 lists the sensitivity for the two scan speeds, 15 and 30 arcsec/sec, used for the AOTs. Note that confusion is not considered in these estimates.

The detection limits in the table are per single scan. Read also the notes in Section 4.4.2 for estimating the detection limits for multiple observations.

Table 4.4.11: The 5σ detection limits for AOT FIS02.

Point Source (mJy)								
Scan speed	15 arcsec/sec				30 arcsec/sec			
Reset	0.5 sec	1.0 sec	2.0 sec	CDS	0.5 sec	1.0 sec	2.0 sec	CDS
N60	140	100	70	2500	220	150	150	4000
WIDE-S	28	20	14	500	45	30	30	800
WIDE-L	36	18	9	700	70	35	20	1300
N160	72	36	18	1400	140	70	40	2600
Diffuse Source (MJy/sr)								
Scan speed	15 arcsec/sec				30 arcsec/sec			
Reset	0.5 sec	1.0 sec	2.0 sec	CDS	0.5 sec	1.0 sec	2.0 sec	CDS
N60	3	2	1.5	50	4	3	3	70
WIDE-S	0.6	0.4	0.3	10	1	0.6	0.6	15
WIDE-L	0.24	0.12	0.06	3.5	0.35	0.17	0.10	7
N160	0.48	0.24	0.12	7	0.70	0.35	0.20	14

* Values for 15 arcsec/sec are identical to those in for the FIS01.

Saturation Limits

Since the FIS detector saturation depends only on the reset interval, this is the same table as for FIS01 (Table 4.4.8 on page 56).

Linearity Limits

Since the FIS detector saturation depends only on the reset interval, this is identical to FIS01 (Table 4.4.9 on page 56).

4.4.5 FIS03: FTS Spectroscopy

Observations with the FIS/FTS are very challenging. Due to the low sensitivity and narrow dynamic range, careful selection of the target is needed. There are various instrument anomalies that have to be settled and corrected. Reduction of the FTS data will consist of many iterative procedures and trial processing. Any observers who plan to observe in this mode are kindly requested to carefully read the following section as well as the performance section (Section 4.2) and to optimize their observation plan to maximize the scientific output.

AOT description

The **FIS03** AOT is designed for spectroscopic observations with the FTS.

Table 4.4.12: FIS03 summary.

Fixed parameters	
Observing Mode	Spectroscopy
Band	WIDE-S, WIDE-L
Scan pattern	Staring (no Step-Scan)
User defined parameters	
Sampling mode	Nominal (fixed)
Reset interval	0.1, 0.25, 0.5, or 1.0 sec (see text)
Resolution	Full-resolution / SED

[Instrument operation]
The instruments are set up for the FTS mode. The filter wheel is rotated to switch from the empty hole to the polarizer. Detector readout mode is switched to high-frequency sampling mode. Only data from the WIDE detector arrays are acquired. During the observation, the moving mirror is driven. Two path lengths, i.e., spectral resolutions, are available (See Section 4.1.4). The spectral resolution is ~ 0.36 cm^{-1} for the *Full resolution* mode and ~ 2.4 cm^{-1} for the *SED* mode. The SED mode provides better quality spectra than the Full-resolution mode spectra after being smoothed to a corresponding resolution. There are five choices for the reset interval, similar to the other FIS AOT's. However, CDS readout mode is not available.

[Scan operation]
The FTS spectroscopic observation is operated in a staring pointing mode. To minimize the dead time, No Step-Scan, Micro-Scan, nor Slow-Scan is carried out during a pointed observation. If the observer needs accurate spatial-spectroscopic information, one must repeat the observation of the same area with a slightly shifted target position. Observations of a wider area should repeat the observations on different orbits.

[User specified parameters]
The following inputs have to be given by the observer.

Resolution mode Full-resolution or SED. See the description above.

Reset interval Four choices from 0.1[4], 0.25, 0.5, and 1.0 sec are available. As the CDS mode for the brightest targets cannot be used for the FIS03 AOT, a shorter reset interval of 0.1 sec is alternatively provided. This shortest reset interval is available thanks to the 5–7 times faster detector sampling rate in this operation mode. As with the other observing modes, the longest reset interval that does not cause saturation of the detectors is preferable. If the target flux is uncertain, a shorter reset interval is safer.

Target position The target position is observed at the center of the WIDE-S array. A small adjustment may be applied according to the in-flight performance.

Expected Performance

[**Detection Limits**]
The 5σ detection limits for the FTS observations in one pointing opportunity are shown in Table 4.4.13. In fact, the sensitivity of the FTS has a wavelength dependency. The sensitivity is better near the band center and drops toward the band edges, following the spectral response of the system. The SW channel shows a further decrease in sensitivity below 80 μm due to a decrease in the interferometric efficiency. In addition, interference occurs within the detector elements of the SW array (Section 4.2.3. This results in strong fringes in the spectra. Due to these fringes, the sensitivity is a rapid function of wavelength. More detailed information will be given later.

It should be noted that the sensitivity is significantly lower than the numbers previously announced (before Observer's Manual ver. 2.0).

Table 4.4.13 summarizes the detection limit of the FIS03 mode for various wavelengths, and Table 4.4.14 shows the detection limits for major FIS observable far-infrared lines. Figure 4.4.26 shows the 5σ detection limits profile for continuum and line observations.

Table 4.4.13: Detection limits of the FTS for the exposure of 500 sec (5σ).

			Line	Continuum			
			(10^{-15} W/m2)	Point (Jy)		Diffuse (MJy/sr)	
Wavelength	Wavenumber	Detector	Resolution				
(μm)	(cm$-$1)		Full	Full	SED	Full	SED
60	170	SW	33	710	100	15000	2130
90	111	SW	4.8	100	14	2200	320
110	90	SW	2.4	63	9	1400	200
110	90	LW	37	510	73	7300	1040
140	71	LW	8.4	160	23	2000	280
170	60	LW	24	440	63	4700	670

[4]The actual reset interval is 0.14 sec.

Table 4.4.14: Detection limits of the FTS for major far-infrared lines (500 sec, 5σ).

Line	Detector	Wavelength	Wavenumber	Detection Limit
		(μm)	(cm−1)	(10^{-15} W m^{-2})
[N III]	SW	57.32	174.47	580
[O III]	SW	51.83	192.99	400
[O III]	SW	88.36	113.18	19
[O I]	SW	63.18	158.27	40
[O I]	LW	145.53	68.72	11
[N II]	LW	121.80	82.10	12
[C II]	LW	157.74	63.95	15

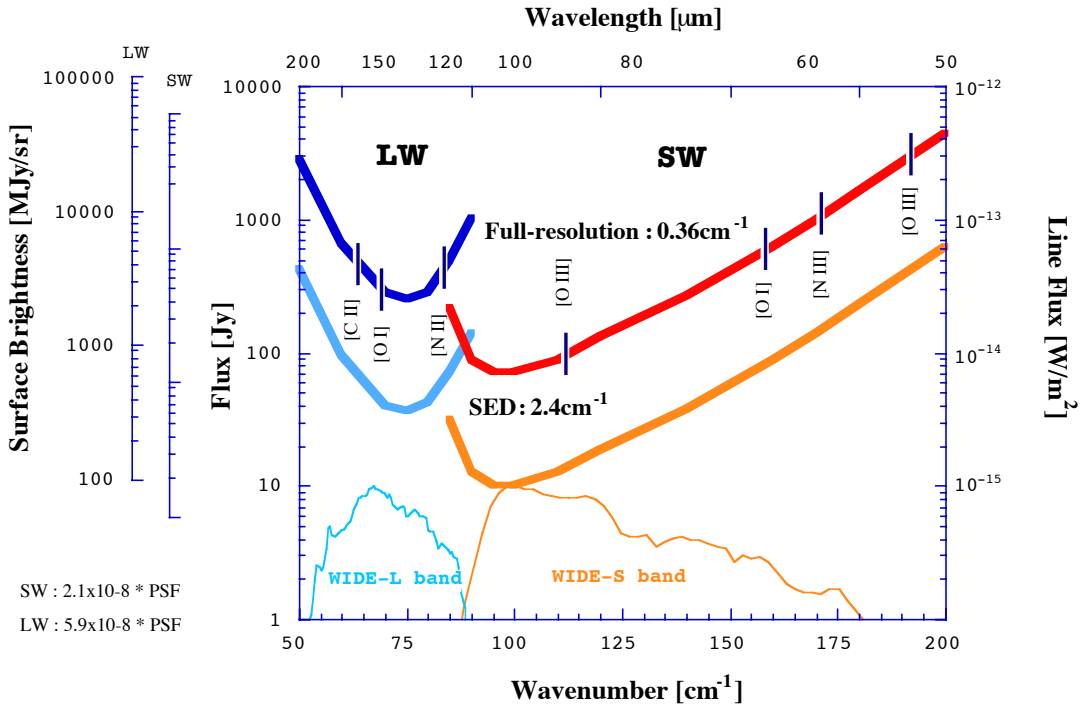

Figure 4.4.26: The 5σ detection limits profile of AOT FIS03 mode. The axes are for diffuse radiation (LW and SW detectors respectively), point source continuum flux, and line emission, respectively from left to right.

[Saturation Limits]

Table 4.4.16 shows the saturation level in the FTS mode. These estimates are based on the photometric mode data scaled by factors of instrumental efficiency. The polarizer used in the FTS system reduces the optical throughput by a factor of 4. Higher detector sampling rates also help to push the saturation level up higher. The numbers still have large uncertainties and should be treated as "of order" estimates.

Table 4.4.15: This table is not available any more. Caption remains to keep the table numbers.

Table 4.4.16: Saturation limits for FIS03.

Point Source (Jy)				
Reset (sec)	0.1	0.25	0.5	1.0
SW(WIDE-S)	1100	520	260	130
LW(WIDE-L)	2000	960	400	170
Diffuse Source (GJy/sr)				
Reset (sec)	0.1	0.25	0.5	1.0
SW(WIDE-S)	13	6.7	3.4	1.7
LW(WIDE-L)	17	8.0	3.4	1.4

4.4.6 Remarks and Constraints of the FIS Observations

1. **Hits of charged particles**
   Impacts of charged particles on the detector arrays produce glitches or spikes. A particle hit could saturate the detectors. In addition "tails" with decay time-scales of a few tens–few thousands seconds are observed after glitches. They are regarded as a temporal variation in the detector responsivity. The frequency of impacts heavy enough to be recognized as glitches are estimated to be 0.1–a few per minute per pixel.

2. **The South Atlantic Anomaly (SAA)**
   The SAA is a region where the radiation belt surrounding the Earth reaches to a lower altitude than at other places. In the SAA, a significant number of charged particles hitting the detectors prevent ASTRO-F from any observation. The responsivity of the detectors also change after the passage of the SAA, with a recovery time-scale of a few thousand seconds. About a half of the orbits per day are affected by the SAA. We will carry out a *Bias boost* (increasing detector bias to wash out charge carriers generated in the SAA) for curing the detectors. This reduces the temporal variation of the detector responsivity, but we still have a significant time variation. We will attempt to correct these effects by monitoring the detector response by calibration lamp pulses and in the data reduction process.

3. **Observation of extended sources**
   It is known that Ge:Ga detectors have various complicated characteristics such as transient effects and after effects of charged particle hits etc. These characteristics make the data reduction and calibration difficult. Although the data reduction of the pointed observations are the users responsibility, close communication with the project team is inevitable. In particular, observers who are interested in imaging observations should not be overly optimistic. We are open to any observers wishing to participate in the data reduction activity. We also plan to organize a user consortium for the FIS observations in particular.

4. **Observation with FTS mode**
   Again, we would like to emphasize thats observation with the FTS (FIS03) is not easy. Therefore following conditions are given for the Open Time Proposals:

   (a) The number of FTS observations in open time will be limited to no more than 5 per cent of the total number of open time pointed observations.

   (b) Proposers are strongly recommended to confirm the feasibility of proposed observations with the condition that the signal-to-noise ratio be larger than 10 for any single pointed observation.

   (c) Successful proposers are required to work closely with the FIS/FTS team for the data reduction. A dedicated contact point will be given.

Chapter 5

IRC: Infrared Camera

The Infrared Camera (IRC) on board ASTRO-F is designed to carry out deep imaging observations in pointed observing mode. It's unique wide field coverage of 10×10 arcmin^2 is ideal for survey-type observations. The IRC's low-resolution spectroscopic capabilities in the imaging field are also well suited for multi-object spectroscopic surveys. A scanning operation has been developed with the cameras enabling us to extend the ASTRO-F All-Sky Survey wavelength coverage into the Mid-Infrared range.

5.1 Hardware Specification

5.1.1 Overview

The IRC consists of three cameras: NIR, MIR-S and MIR-L. Covering the wavelength ranges of 2–5, 5–13, 12–26 μm, respectively. In Table 5.1.1, the specifications of each camera are tabulated. See also figure 2.4.5 and 2.4.6.

Table 5.1.1: Specifications of the Infrared Camera (IRC).

Channel	NIR	MIR-S	MIR-L
Detector	InSb(SBRC-189)	Si:As (CRC-744)	Si:As (CRC-744)
Array	512×412	256×256	256×256
Imaging FoV (arcmin^2)[1]	9.5×10.0	9.1×10.0	10.3×10.2
Imaging Area (pixel^2)[1]	391×412	233×256	246×256
Pixel Size (arcsec)	1.46×1.46	2.34×2.34	2.51×2.39
Wavelength (μm)	1.7–5.5	5.8–14.1	12.4–26.5
Filters	N2, N3, N4	S7, S9W, S11	L15, L18W[2], L24
Dispersion Elements	NP, NG	SG1, SG2	LG2

[1]Cross-scan $\times$ in-scan. Masked areas are excluded.

Each camera is equipped with three filters and two dispersion elements. The filter selection is preset in the Astronomical Observation Templates (AOTs; Section 5.5) and cannot be freely chosen by the observers.

5.1.2 Optics

All three cameras of the IRC are off-axis, refractive optical systems. Each camera uses 2–5 lenses. A Ge beam-splitter divides the light between the NIR and MIR-S cameras. Transmitted light comes into the NIR channel. Chromatic aberration does exist in the cameras and is largest in the MIR-S camera which uses only two lenses.

A filter wheel is placed at the iris of each camera. Three filters, two dispersion elements, and a blind mask are prepared for each camera. The blind position will be used for dark measurements during the flight operation.

5.1.3 Filters and Dispersion Elements

Table 5.1.2 shows the filters and the dispersion elements of the IRC.

Each camera is equipped with three broad band filters and two dispersion elements. The NIR camera covers three independent wavelength bands that very roughly correspond to the well known K, L, and M bands. The two MIR cameras each have two narrow filters which cover the shorter and longer half of the wavelength range of the cameras,and a wide filter that overlaps the two narrow filters.

The two dispersion elements of the NIR camera provide different spectral resolutions over a similar wavelength range. In the MIR-S and MIR-L, each dispersion element covers about half of the camera's wavelength range. However, unfortunately one of the elements of MIR-L, LG1, was degradated during the ground tests. Thus only LG2 will be used for observations, resulting in a gap in the wavelength range corresponding to the LG1 element.

Table 5.1.2: IRC Filters and Dispersion Elements

(1) Channel	(2) Name	(3)	(4) Wavelength (μm)	(5) Center (μm)	(6) Width (μm)	(7) Resolution ($\lambda/\Delta\lambda$)
NIR	N2	filter	1.7–2.7	2.43	0.68	—
	N3	filter	2.7–3.7	3.16	1.12	—
	N4	filter	3.7–5.5	4.14	1.22	—
	NP	prism	1.7–5.5	—	—	22 @3.5 μm
	NG	grism	2.5–5.0	—	—	135 @3.6 μm
MIR-S	S7	filter	5.8–8.4	7.3	2.6	—
	S9W	filter	6.5–11.6	9.1	4.3	—
	S11	filter	8.6–14.1	10.7	4.7	—
	SG1	grism	5.5–8.3	—	—	47 @6.6 μm
	SG2	grism	7.4–13.0	—	—	34 @10.6 μm
MIR-L	L15	filter	12.4–19.4	15.7	6.20	—
	L18W[1]	filter	13.9–25.3	18.3	10.0	—
	L24	filter	20.4–26.5	23.0	5.4	—
	LG1[2]	grism	— Not available —			
	LG2	grism	17.7–25.0	—	—	27 @20.2 μm

(4) Defined as where the responsivity for a given energy is larger than $1/e$ of the peak.
(5) Central wavelength of the filter band.
(6) Effective bandwidth.
(7) From Table 5.5.10. Dispersion power of prism depends on wavelength. This number is an average of the values at both ends of the wavelength range (4).
[1]Renamed from L20W. No change of the wavelength profile itself.
[2]LG1 was degraded during the ground test and will not be used for observations.

5.1.4 Field of View (FoV)

Figure 5.1.1 shows the location of the FoV of the three IRC cameras on the Focal-Plane projected onto the sky (See also Figure 2.4.8). As noted earlier, the NIR and MIR-S cameras observe the same FoV on the sky simultaneously. The MIR-L camera looks to a position offset by $\sim$ 20 arcmin from the other two cameras. This means that at least two pointed observations on different revolutions are needed to observe a particular position by all three cameras. Step-Scan operation (Section 3.2.2) will *not* be used because of its large dead time.

Reference positions for the AOT configurations for pointed observations are indicated in blue in Figure 5.1.1. Two reference positions for imaging observations (AOT IRC00, IRC02, IRC03, and IRC11; see Section 5.5), namely the centers of the NIR/MIR-S and MIR-L cameras, are labelled as 'N' and 'L', respectively. Reference positions for spectroscopic observations (AOT IRC04) are explained in the following section.

The numbers in Table 5.1.1 and Figure 5.1.1 were derived from the data after the final integration of the instrument into the FM cryostat and can be regarded as the final pre-flight values. An uncontrollable alignment error shifted the NIR and MIR-S FoV slightly toward the slits, resulting in a smaller imaging area than the original design. On the other hand, the FoV of the MIR-L has been enlarged by the successful refurbishment of the camera optics after 2003.

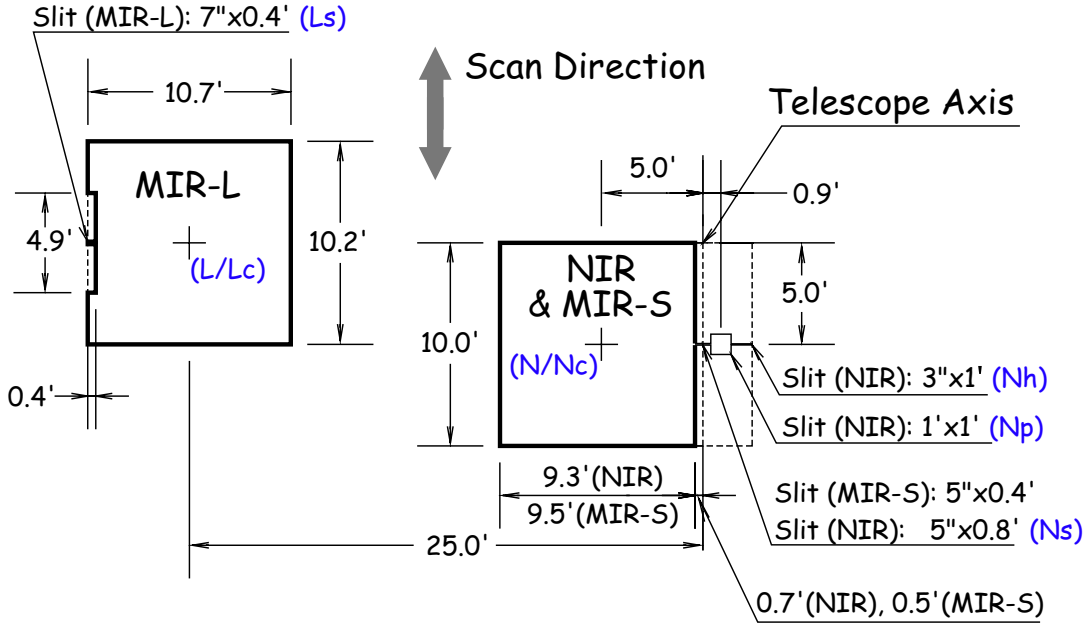

Figure 5.1.1: Focal-Plane layout of the IRC cameras. Reference positions for pointed observations are indicated in blue.

5.1.5 Slits for Spectroscopy

The dispersion elements of the IRC are set into the filter wheel so that all the light in the FoV is dispersed. A spectrum is obtained in the direction parallel to the scan path (in-scan direction), which runs along the vertical direction in Figures 2.4.8 and 5.1.1. Slits are provided for each camera (Figure 5.1.1) in order to avoid contamination by nearby sources / diffuse radiation. The slits are primarily designed for extended sources and it should not be assumed that they can be used to guide a point source into the slit, except for the NIR camera which has an aperture for point sources. The current design is the following.

- The slit for the NIR camera consists of three parts of different widths. The left most (closest to the imaging area) has a 5 arcsec width and will be mainly used for simultaneous observations of diffuse light with the MIR-S camera. This slit position is labeled as 'Ns' for IRC04 AOT observation parameter. Both the NP (low-resolution prism) and NG (high-resolution grism) will be used with this slit. The middle $1' \times 1'$ square part, referred to as 'Np' is for spectroscopy of point sources. The aperture is large compared to the absolute pointing accuracy of the satellite (designed to be better than 30 arcsec) to ensure that the target can be accurately guided into the area. Note that for observations of faint sources, confusion due to galaxies may be a serious problem. The NG (grism) is assumed to be used with this aperture. The rightmost (outer) part ('Nh') has a 3 arcsec width and is used for the highest resolution spectroscopy of diffuse radiation with the NG (grism).

- The MIR-S has a slit of 5 arcsec width for diffuse light. As this slit overlaps with innermost slit for the NIR camera, it is also referred to as 'Ns'. We assume that the point source density in the mid-infrared range is low enough to avoid serious confusion, such that spectroscopy of point sources can be made in the imaging field.

- The MIR-L has a 7 arcsec slit for diffuse light similar to that of the MIR-S camera. This position is referred to as 'Ls'.

5.1.6 Detectors

The detectors of the IRC are provided by Raytheon IRCoE. The NIR camera has an InSb detector array of 512×412 pixels (SBRC-189), in which 391×412 pixels are used for imaging and the other 121×412 pixels are for slit spectroscopy. The two detectors for the MIR cameras are both Si:As type (CRC-744) with a format of 256×256 pixels. There are some, but few dead / hot pixels in the detectors.

It is known that the detector performance sensitivity changes with temperature. All detector arrays are equipped with thermometers to monitor the module temperature during their operation.

5.2 Pre-flight performance

5.2.1 Optics

Field of View (FoV)

As already explained in the previous section, The FoV of the IRC cameras differ slightly from the original design specification values. The MIR-L has wider FoV of 10.3 (cross-scan) $\times$ 10.2 (in-scan) arcmin^2. The FoV of the NIR is different for different filters depending on the alignment of the filters. A summary is given in Table 5.2.3.

Table 5.2.3: Final FoV size of the NIR camera.

Band	FoV (arcmin^2)
N2	9.2×10.0
N3	9.5×10.0
N4	9.5×10.0

Point Spread Function (PSF)

The expected performance of the ASTRO-F telescope was to be diffraction limited at ~ 6 μm. This means that the PSF is more extended than the diffraction limits in the NIR camera. The PSF of each band was measured by putting an aperture mask at the focus of the cameras. The PSF was measured by putting a pin-hole mask at the focus of each camera. The FWHM of the measured PSF is larger than the designed value except for the L18W and L24 bands where the images are diffraction limited. The PSF becomes elongated at the edges of the imaging area. Table 5.2.4 shows the Full-Width Half Maximum (FWHM) of the PSF for the imaging bands of the IRC cameras. Note that because of differences between the laboratory measurements and flight configuration, the real value may be slightly different from those listed in the table.

Table 5.2.4: Full-Width Half Maximum (FWHM) of the PSF for the IRC imaging bands measured in the ground tests.

(1)	(2)	(3)
Channel	Band	FWHM (pix)
NIR	N2	1.85
	N3	1.47
	N4	1.34
MIR-S	S7	1.22
	S9W	1.39
	S11	1.52
MIR-L	L15	2.13
	L18W	2.22
	L24	2.45

In Section 5.5.1 we discuss the optimized photometric aperture size and the detection limits.

Chromatic Aberration

The NIR camera has chromatic aberration of 0.3–0.4 mm, which is in fact larger than the designed value. The most likely cause is the uncertainty of the optical characteristics of the elements under cryogenic temperature. The mean amount of aberration is comparable to that of the diffraction limited optics at 2 μm and thus effects the image quality.

Optical Transmittance

The throughout transmission function (RSRF: Relative Spectral Response Function) of the IRC broad band filters are shown in Figures 5.2.2, 5.2.4, 5.2.6. The filters and optical components as well as the detector response are taken into account to produce the curves[1]. These RSRFs can be directly integrated over spectra given as F_λ to obtain the in-band fluxes.

Figures 5.2.3, 5.2.5, 5.2.7 show the RSRFs of the dispersion elements. In the figures they are given as per photon.

This data, in digital format, are also available on the Observer's support page.

[1]These RSRFs have been prepared in collaboration with Dr. Martin Cohen to ensure a common calibration of the IRC with other missions and ground-based instruments, including Subaru/COMICS, in the framework of the absolute calibration network provided by him and his colleagues.

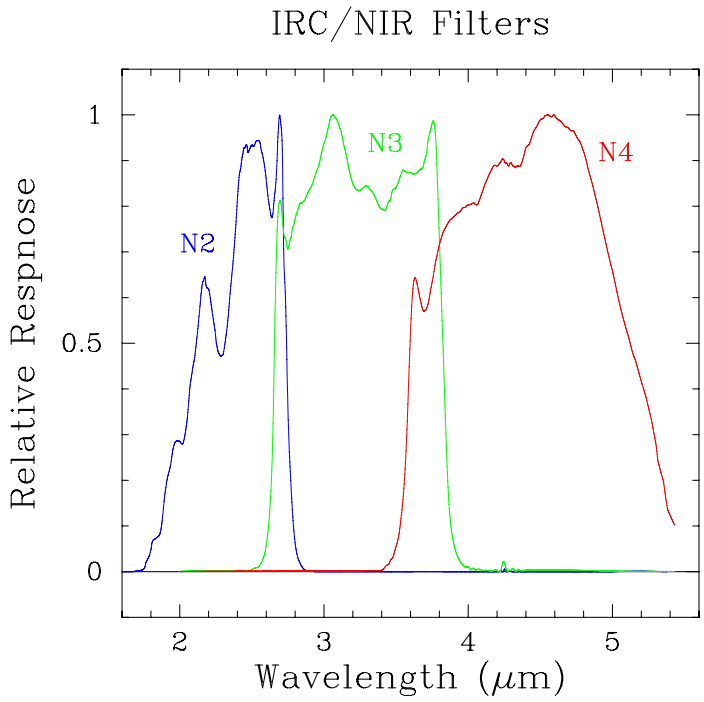

Figure 5.2.2: The Relative Spectral Response Function of the IRC/NIR Camera for F_λ.

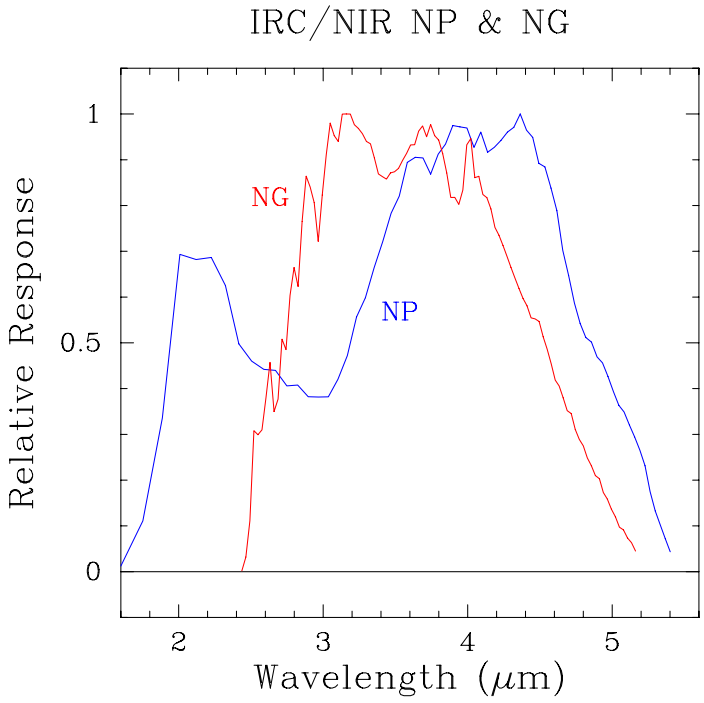

Figure 5.2.3: The Relative Spectral Response Function of the IRC/NIR dispersion elements per photon.

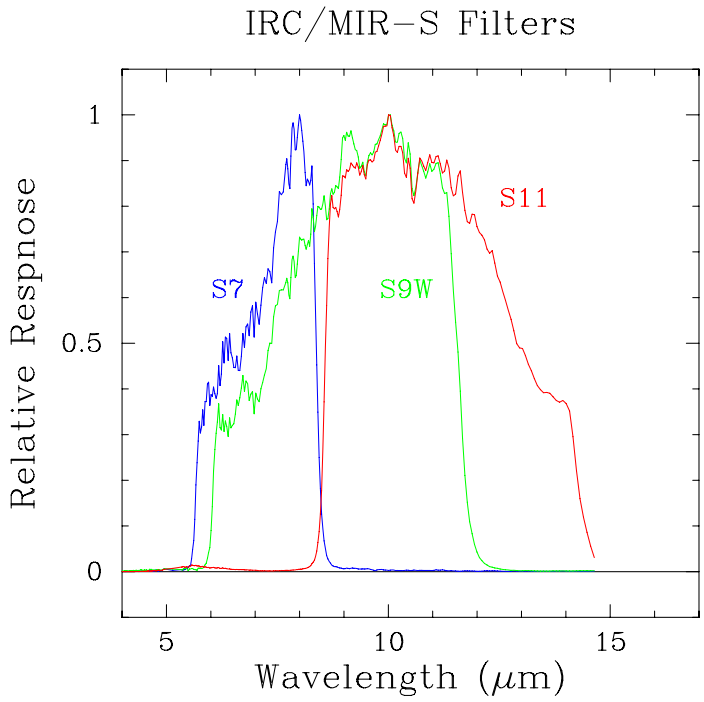

Figure 5.2.4: The Relative Spectral Response Function for F_λ of the IRC/MIR-S Camera.

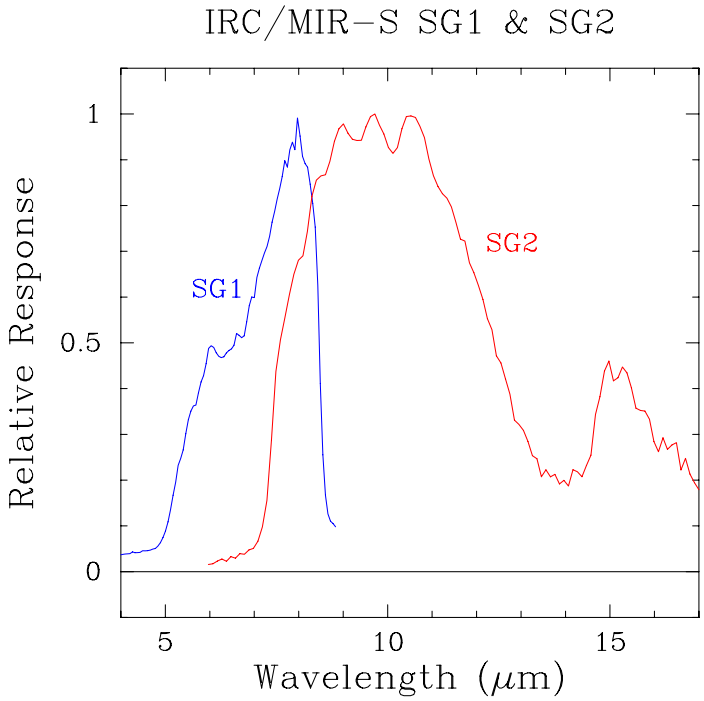

Figure 5.2.5: The Relative Spectral Response Function of the IRC/MIR-S dispersion elements per photon.

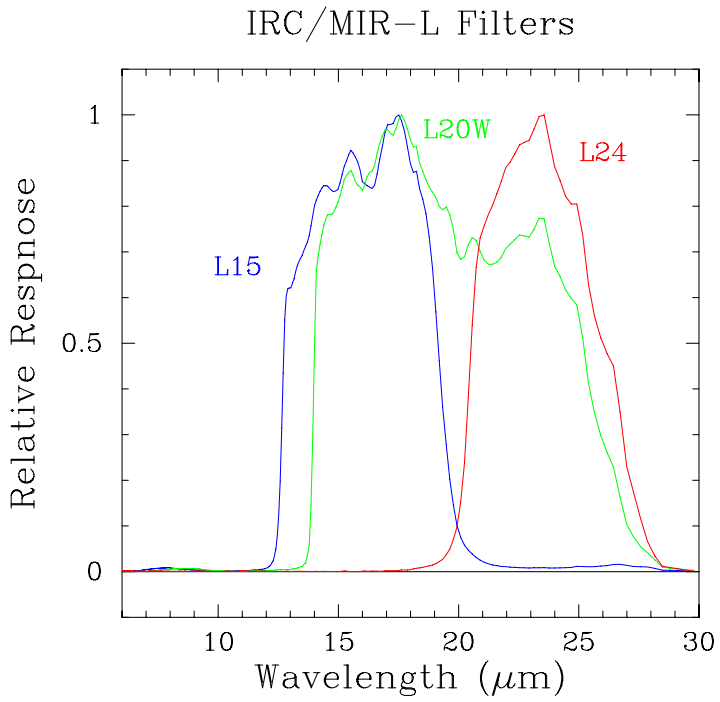

Figure 5.2.6: The Relative Spectral Response Function of the IRC/MIR-L Camera for F_λ.

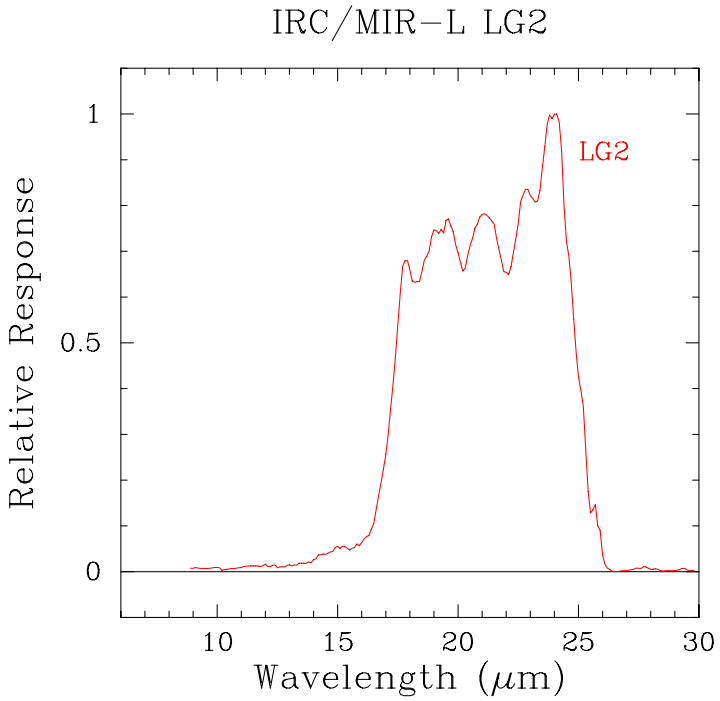

Figure 5.2.7: The Relative Spectral Response Function of the IRC/MIR-L dispersion element per photon. LG1 will not be used for astronomical observations due to degradation. Data shown here is 2nd order light subtracted.

Leakage

Leakage has been investigated for the MIR filters. Figures 5.2.8 shows the filter transmittance profiles of the flight backup filters. All filters show an indication of short wavelength leakage around 1/2 of the main passband. In addition, long wavelength leakage is also found in the S7 and S11 filters. The contribution of these short wavelength leaks in the photometry for stars $> 3000K$ is about 0.6 per cent in the S7 and S9W band, 1–2 per cent in the S11 and L24 bands, and 3–4 per cent for the L15 and L18W bands.

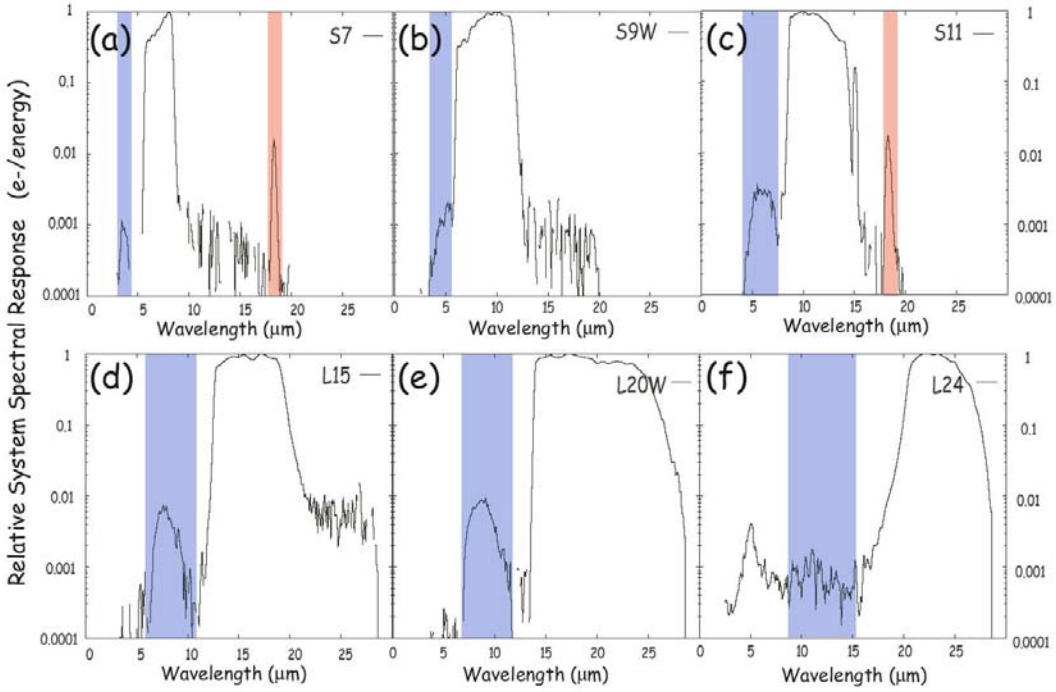

Figure 5.2.8: Possible leaks in the IRC/MIR filters. Leaks are indicated by blue or red masks.

Distortion

Image distortion of the IRC FoV is illustrated in Figure 5.2.9 (Kim et al. 2005; Fujishiro et al. 2005) for three filter bands. They are calculated by optical simulation software with the parameters reflecting the results of the laboratory measurements.

Distortion is largest in the NIR camera with a shift of up to 10 pixels near the edge. It is about 7 pixels in the MIR-S camera. The MIR-L camera shows little distortion, 1.5 pixels at the most. The image distortion will be also measured during the PV phase and a correction will be applied in the data reduction.

Ghosting

Ghosting is found in the NIR and MIR-S cameras. Figure 5.2.10 shows NIR and MIR-S images of a pin-hole mask at the aperture. The pin-holes are at regular grid intervals and are seen as bright spots. The ghosting images of the holes appear between the bright spots.

The cause of the ghosting has been understood as reflection inside the beam-splitter. The relative position between the true image and the ghost image is predictable. The energy ratio of the ghost image with respect to the true image is about 0.7 per cent for the NIR bands and

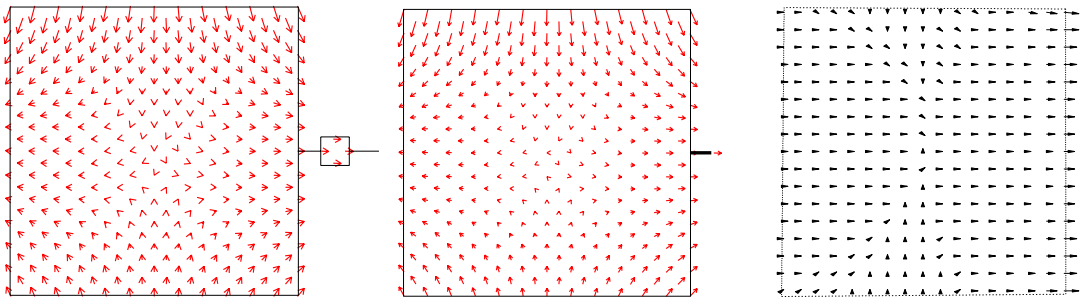

Figure 5.2.9: Image distortion pattern of the IRC cameras. From left to right, NIR (N2), MIR-S (S7), and MIR-L(L18W). Distortion is emphasized by the arrow lengths. The maximum distortion is about 10 pixels in NIR, 7 pixels in MIR-S, and 1.5 pixels in MIR-L, respectively (Kim et al. 2005; Fujishiro et al. 2005).

about 0.75 per cent for S7 and S9W bands. The S11 band shows the highest ratio of 3.8 per cent, due to the characteristics of the A/R coating of the beam splitter.

Since the ghosting is predictable, it is, in principle, possible to remove it at the data reduction stage. Nevertheless, observations of faint sources nearby strong sources will require special care.

No obvious ghosting was detected in the MIR-L camera.

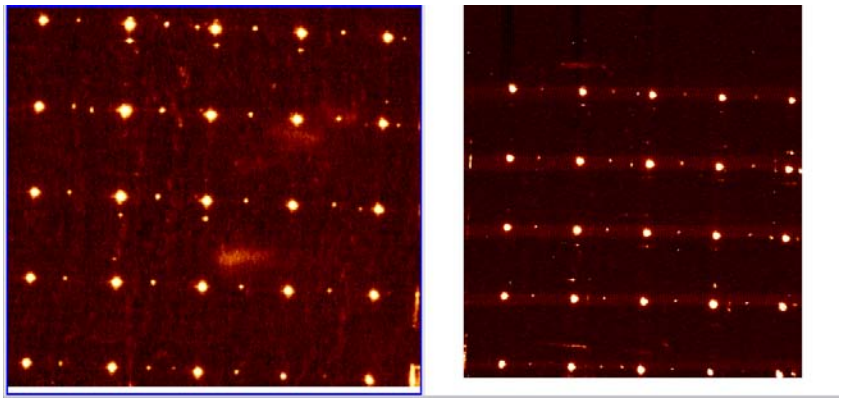

Figure 5.2.10: Ghost image of the NIR (right) and MIR-S (left) cameras. These images are obtained by putting a pin-hole mask at the entrance aperture. The bright spots are pin-holes, and weak spots between the bright spots are the ghost images. The slits are on top of each image. Extended features seen in the MIR-S data are due to the measurement configuration and will not appear in the flight data.

5.2.2 Detector system

Bad Pixels

There are some dead / bad pixels reported in each camera of the IRC. The numbers are much less than 0.1 per cent in the NIR and MIR-S, and are about 0.3 per cent in the MIR-L camera [2]. The bad pixels are usually independent or clustered over a several pixels. Only the MIR-L shows a relatively large cluster near the middle and at one of the corners (Figure 5.2.11). The one in the corner is probably due to effects from the detector readout circuit.

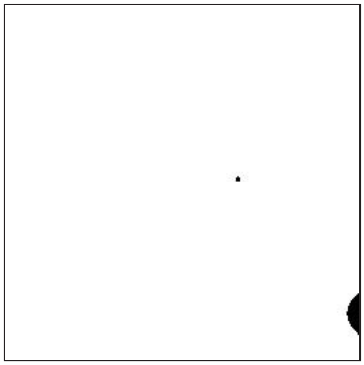

Figure 5.2.11: Bad pixels on the MIR-L detectors. The dimensions of the image correspond to the FoV geometry projected onto the sky. A large clustering at the bottom-right corner is probably due to effects from the detector readout circuit.

Dithering observations are essential to minimize the effect of bad pixels and are included in AOT IRC02 and 03 Section 5.5). It is the users' responsibility to repeat observations in different pointing opportunities for IRC00 and 04 (and probably 03) observations.

Noise

Transient effects of the detectors are expected to be very small, and may be negligible in most cases. The stability of the responsivity after irradiation by charged particles (especially in SAA) has not been evaluated quantitatively.

Linearity

The linearity of the IRC detectors has been measured. Plotted in Figure 5.2.12 are the deviations from linearity of the detector output signal against the readout signal in ADU. It is seen that the three detectors follow a similar non-linear pattern and stay within 10 per cent deviation up to $\sim$ 12000 ADU. This results in a dynamic range of over four orders in magnitude. Current investigation shows that the non-linearity correction can improve the linearity to the few per cent level.

[2]Here we define bad pixels as those signals in which the dark image deviates by 3σ from the average.

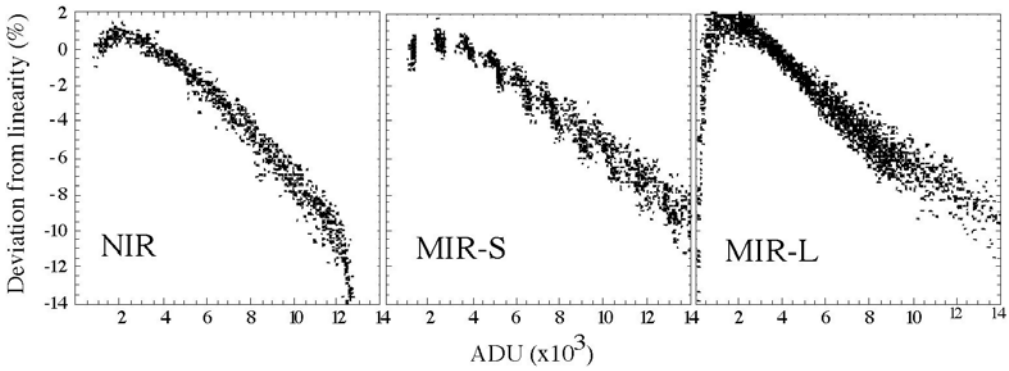

Figure 5.2.12: Deviation from linearity plotted against the readout signal level in ADU for the three IRC detectors.

5.3 The IRC Instrument Operation

5.3.1 Pointed Observations

Exposure cycle

The minimum observation unit of the IRC is called an *exposure cycle*. An IRC pointed observation consists of an n times repeated *exposure cycle* with operations such as a filter change and Micro-Scan inserted between them. The operation sequence of the exposure cycle is designed by the IRC team to optimize the performance of the instrument and observation efficiency. The current (and expected to be the flight) design of an exposure cycle is illustrated in Figure 5.3.13.

The unit time length for a detector driving is ~ 0.58 seconds, which corresponds to the time for the MIR-S/L detectors to access all pixels in the array. The NIR detector takes 4 times longer. Time durations in the exposure cycle are always a multiple of this unit time.

One exposure cycle takes about 72.5 sec, for both the NIR and MIR channels. The three cameras are operated synchronously. However, use of this exposure cycle is different in the NIR and MIR channels. The NIR detector carries out one short (2.3 sec) and one long exposure (51 sec) in a cycle, while the MIR detectors do one short (0.6 sec) and three long (19 sec) exposures. These short exposures correspond to one detector driving unit time. The short exposures are useful for bright stars that may saturate the detectors. However, the photometric accuracy of the short-exposure is probably much worse than the long-exposure. *Fowler 4* sampling is taken for the longer integrations of all detectors, to reduce the readout noise by a factor of two.

Two images from the NIR channel and four images from each MIR channel are produced in one exposure cycle. They are stored in the frame memory buffer, then divided into telemetry packets and down-linked to the ground. The on ground data reformatting software will reconstruct the frame memory buffer and eventually a set of images, which are then passed to the observers.

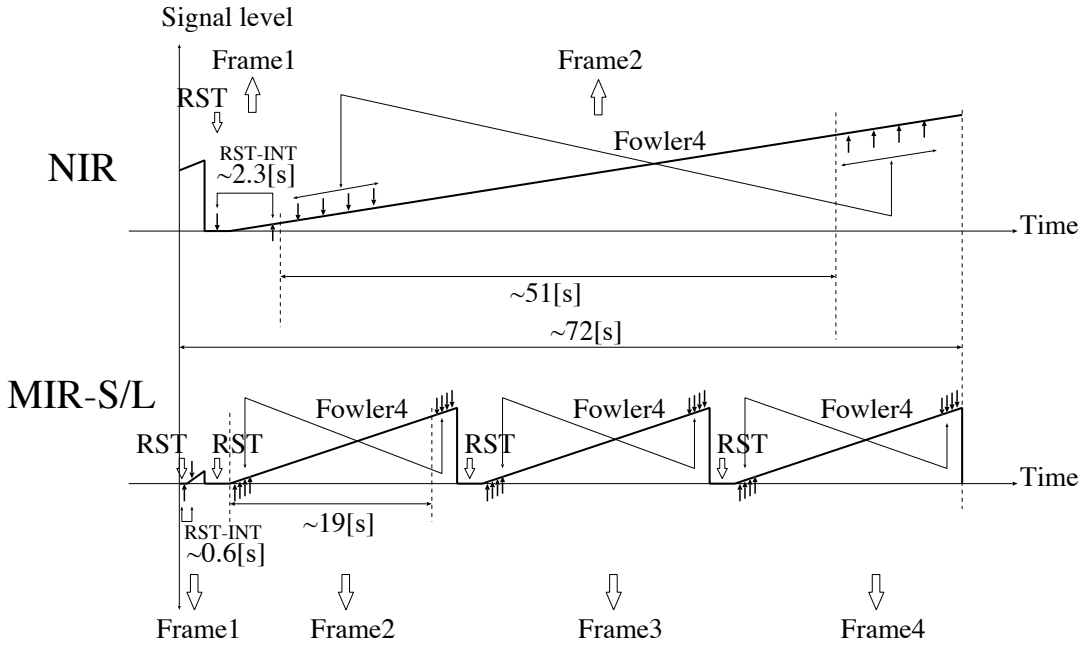

Figure 5.3.13: An illustration of the operation of one exposure cycle. A pair of short and long exposures are carried out for the NIR camera while one short and three long exposures are prepared for the MIR channels. **RST** indicates a reset of the detector.

A pointed observation is carried out by repeating the exposure cycle with Micro-Scans and filter changes inserted between them. These operations cause dead time due to the operations themselves and stabilization of the satellite attitude. Current estimates of the dead time are 20–80 seconds, depending on the operation and the performance of the attitude control system. Additional time for sending the data to the satellite's data processor (DHU) is also needed. These operations and dead-times are taken into account in the design of the Astronomical Observation Templates (AOT; section 5.5).

During a pointed observation, the IRC on-board controller communicates with the Attitude and Orbit Control Unit (AOCU) via the DHU. When the IRC requests a Micro-Scan for dithering, it asks the AOCU to carry out the operation. The AOCU drives the satellite, then waits for the stabilization. When the AOCU decides that the satellite has stabilized, with a preset criteria, it sends back a signal to the IRC (via the DHU) to start the next exposure cycle. This sequence continues until the AOT is completed. If, by some reason, the attitude of the spacecraft exceeds the allowed range of the angle with respect to the Earth, the AOCU stops the pointing mode attitude and returns back to the survey attitude, regardless of the observation. The IRC will continue its programmed exposure sequences but of course those data acquired during the maneuver are useless and will not be provided to the users. Current AOTs assume that one pointed observation could last longer than 10 minutes and add extra exposure cycles at the end.

5.3.2 The IRC Scan Observation

The two MIR cameras are able to operate in a "Scan Mode". This operation mode will be used for the IRC All-Sky Survey. An AOT to use this mode for pointed observations is also available.

The scan operation is realized by operating a part of the two-dimensional detector arrays. Namely, one line of a detector array, perpendicular to the scan direction, is repeatedly readout as the satellite scans the sky resulting in an image strip along the path. The NIR array has a technical difficulty for such operation from the detector structure and will therefore not be used in this observation mode.

Due to the strong constraint of the data down-link rate, it is impossible to transfer individual pixel data to the ground in this mode, so some on-board preprocessing will be carried out . The data from every four physical pixels are summed up to form one virtual pixel. By adjusting the detector readout interval and scan speed, the shape of a virtual pixel can be controlled. The current plan is to compose an almost square shape virtual pixel from four physical pixels for the All-Sky Survey, i.e., the pixel size will be about 9.4 arcsec^2 for the MIR-S channel, and 10.0×9.4 arcsec^2 for the MIR-L channel, respectively. The same sampling interval is applied for the Slow-Scan observations in pointed mode, resulting in a very elongated virtual pixel size. A smaller virtual pixel size, 2×2 mode, could be implemented technically and such a high resolution operation may be carried out if the necessary down-link rate can be guaranteed.

5.4 The IRC All-Sky Survey

The IRC All-Sky Survey will be performed in parallel with the FIS All-Sky Survey, by using the S9W and L18W filters on the MIR-S and MIR-L, respectively. Since the scan path will shift by 4 arcmin per orbit in the cross-scan direction at the ecliptic plane, and the FoV size of the IRC detector is 10 arcmin, every sky position will ideally be observed at least twice. At present, the following spatial resolutions are considered for the IRC All-Sky Survey. The virtual pixel size may be changed depending on the availability of the down-link rate.

Table 5.4.5: Current Specification of the IRC All-Sky Survey

Camera	Filter	Virtual pixel size
MIR-S	S9W	9.4×9.4 arcsec^2
MIR-L	L18W	10.0×9.4 arcsec^2

cross-scan $\times$ in-scan

The ASTRO-F team is responsible for the planning and the data reduction of the IRC All-Sky Survey, and will distribute catalogues to science users, as in the case for the FIS All-Sky Survey.

5.4.1 Operation

During the survey observation, the detector is sampled continuously in the Scan mode. At every 9 sec interval, the charge in the capacitor is reset. A reset causes a gap in the scan strip corresponding to 2–5 sampling intervals. The width of the gap depends on any reset anomaly in flight.

5.4.2 Expected Performance

Detection Limits

Expected 5σ detection limits of the IRC All-Sky Survey are summarized in Table 5.4.6. They are estimated based on the latest performance evaluated in the ground tests. The IRC detection limits are generally influenced by the background radiation, especially the Zodiacal light in the Mid-Infrared range. In the case of All-Sky Survey, detector noise dominates the detection limits so that only one set of numbers are given.

Table 5.4.6: 5σ Detection limits for the IRC All-Sky Survey

Camera	Filter	Point source	Diffuse source*
		(mJy)	(MJy/sr)
MIR-S	S9W	80	25
MIR-L	L18W	130	32

*Detection limits for diffuse source are per virtual pixel.

Saturation Limits

The saturation limits are given as the flux level at which the detector signals deviate from linearity by 10 per cent. In fact, it is rather a rapid change from these levels to the absolute saturation and it is reasonable to use these levels as the saturation limits.

Table 5.4.7: Saturation Limits for the IRC All-Sky Survey

Camera	Filter	$F_{\rm sat}$ (Jy)
MIR-S	S9W	36
MIR-L	L18W	93

5.5 The IRC AOTs

The Astronomical Observation Templates (AOTs) of the IRC are summarized in Table 5.5.8. Five AOTs are defined for the instrument.

Table 5.5.8: IRC AOTs and user parameters.

AOT	Purpose	# of filters per ch.	Dithering	Parameters	
				Filter	Pointing
00	Deep imaging	1	No	3 choices	N, L
02	Imaging with 2 filters/ch.	2	3 pos/filter	N/A (fixed)	N, L
03	Imaging with 3 filters/ch.	3	2 pos/filter	N/A (fixed)	N, L
04	Spectroscopy	1 or 2	No	2 choices	Ns, Np, Nh, Nc, Ls, Lc
11	Slow-Scan	1	N/A	3 choices	Scan speed

The procedures for the AOT operations for IRC00, 02, 03 and 04 are shown in Figure 5.5.14. As explained in the previous section (5.3.1) an AOT consists of a combination of exposure cycles (indicated as "Exp. C"), Filter Wheel rotations ("W") and Micro-Scan operations ("M"). They are optimized such that the maximum exposure time is obtained. The AOTs are designed to use more than 600 sec in the case that extra observation time is available. However, such extra time cannot be guaranteed at present.

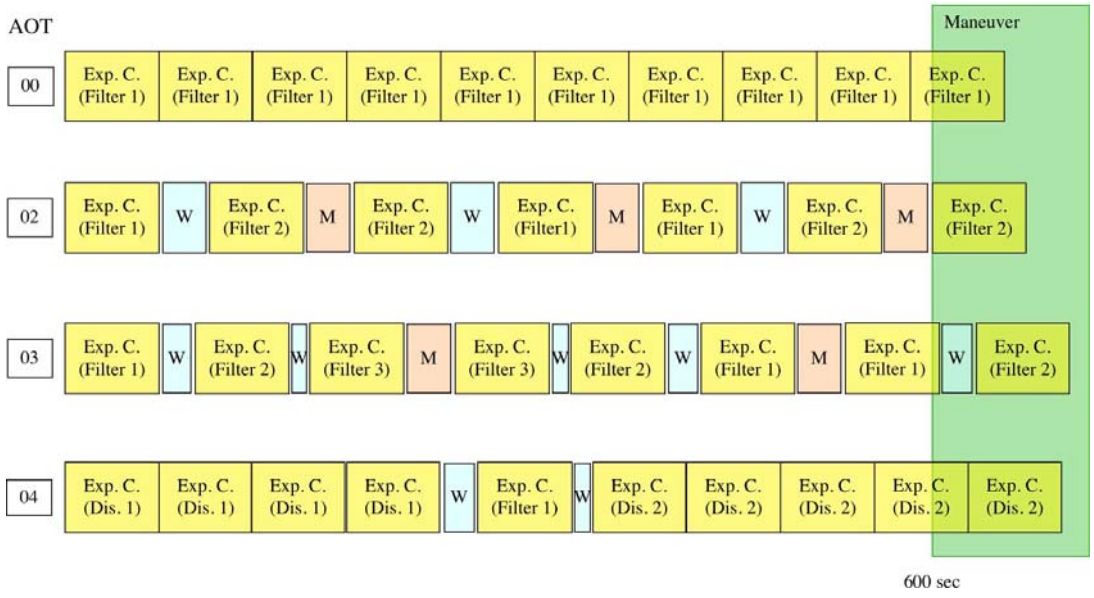

Figure 5.5.14: Observation sequences of the AOT IRC00, 02, 03, and 04. Yellow boxes indicated as "Exp. C." with filter / dispersion element names are exposure cycles. Orange boxes with "M" are Micro-Scan operations including stabilization, and light-blue boxes with "W" are Filter Wheel rotations. Dead time for a Filter Wheel change depends on the relative position of the elements. The Green area on the right side is the extra observation time which is not guaranteed.

5.5.1 Detection Limits and Saturation Limits: General Remarks

In the following sections, the expected detection limits for corresponding AOTs are given. These are 5σ detection limits per single pointing opportunity, estimated based on the latest performance evaluated in the ground tests. Realistic exposure times in the operation sequence are considered, i.e., dead time due to *Micro-Scan* and filter change are taken into account. Repeating an observation of the same region with the same AOT improves the sensitivity by a factor of $\sqrt{n}$, where n is the number of pointing opportunities.

Detection limits in the imaging mode assumes aperture photometry of a well isolated source. The photometry aperture is optimized for each band such that the signal (photons from the source) to noise (dark + readout + sky background) ratio is maximized. The dark and readout noises are estimated from laboratory measurements. Table 5.5.9 lists the best aperture radius and the energy from the source falling into that radius. Table 5.5.10 summarizes the estimated performance parameters of the spectroscopic mode used to calculate the detection limits.

Table 5.5.9: Photometry radius and corresponding encircled energy fraction.

(1) Camera	(2) Filter	(3) Aperture radius (pixel)	(4) Encircled energy (per cent)
NIR	N2	1.90	70
	N3	1.90	65
	N4	1.93	62
MIR-S	S7	0.63	27
	S9W	0.77	32
	S11	0.77	31
MIR-L	L15	1.00	34
	L18W	1.20	33
	L24	1.67	38

(3) The optimized aperture radii that maximizes the S/N of the source.
(4) The fraction of energy within the aperture.

Table 5.5.10: Performance of the IRC Spectroscopic Mode

(1) Camera	(2) Element	(3) Resolution ($\lambda/\Delta\lambda$)	(4) Dispersion (μm/pixel)	(5) Res. bin (pixel)	(6) Slit width (arcsec)	(7) Slit width (pixel)
NIR	NP	22@3.5 μm	0.058	2.7	3.0	2.05
	NG	135@3.6 μm	0.010	2.7	3.0	2.05
MIR-S	SG1	47@6.6 μm	0.057	2.5	5.0	2.13
	SG2	34@10.6 μm	0.101	3.1	5.0	2.13
MIR-L	LG1	— N/A —				
	LG2	27@20.2 μm	0.153	4.9	7.0	2.92

(4) Length of the resolution element ($\Delta\lambda$) in pixel.
(6)(7) Slit width for the diffuse source spectroscopy.

Detection limits are given for two regions on the sky; at the Ecliptic Pole and the Ecliptic Plane. The difference is simply due to the difference in the photon noise level of the zodiacal emission. Detection limits for intermediate positions are provided by the Instrument Perfor-

mance Tool available on-line. It is noted that the current estimates have an uncertainty due to the laboratory measurement setup with the assumed telescope performance. We believe that the values are reliable to ~ 30 per cent accuracy under the expected performance of the spacecraft and the telescope.

The saturation limits are given as the flux level at which the detector signals deviate from linearity by 10 per cent. In fact, it is a rather rapid change from these levels to the absolute saturation and it is reasonable to use these levels as the saturation limits.

5.5.2 IRC00: Deep Imaging Mode

Recommended Usage

IRC00 mode is prepared for deep imaging observations of high visibility regions where more than 6 pointed observations can be easily obtained. This mode is also available for the Open Time users under this constraint.

Description

The mode is designed to maximize the exposure time during a pointing opportunity. The exposure cycle is simply repeated until the end of the pointed observation. No filter change nor dithering operation is inserted. It is expected that observations with other filter(s) and data redundancy by dithering are taken on additional pointing opportunities. It is strongly recommended to observe the same sky position with at least three independent pointings with the same filter setting. The necessary number of pointings is then multiplied by the number of filters. This means that this AOT is only applicable in very high visibility regions, at high ecliptic latitudes. It is recommended for observers to use this mode only in areas of the sky that can be observed more than 6 times (three dithers, two filters) by each of NIR/MIR-S or MIR-L. Due to operational constraints it is very difficult to ensure such high visibility for Open Time and thus use of this mode has to be planned with great care.

Parameters

There are two parameters for this mode. The first parameter specifies the filter combination. To simplify the operation and data handling, three preset filter combinations are defined in Table 5.5.11.

Table 5.5.11: Filter combinations of IRC00

Set	NIR	MIR-S	MIR-L
a	N2	S9W	L18W
b	N3	S7	L15
c	N4	S11	L24

The second parameter designates the FoV reference position to be pointed to the target.

Table 5.5.12: Target position parameter for IRC00

Code	Description
N	Target position is placed at the center of the NIR/MIR-S cameras.
L	Target position is placed at the center of the MIR-L camera.

Same as IRC02 and IRC03.

5.5.3 Expected Performance

Detection Limits

The expected 5σ detection limits of the IRC00 observing mode are given in Table 5.5.13.

Table 5.5.13: Detection limits for AOT IRC00

(1)	(2)	(3)	(4)	(5)	(6)
Camera	Filter	Point source		Diffuse source	
		(μJy)		(MJy/sr)	
		Pole	Plane	Pole	Plane
NIR	N2	7.9	8.7	0.033	0.036
	N3	3.7	4.3	0.014	0.017
	N4	7.2	8.8	0.026	0.032
MIR-S	S7	35	51	0.062	0.091
	S9W	29	47	0.050	0.081
	S11	38	63	0.064	0.11
MIR-L	L15	68	120	0.093	0.17
	L18W	84	160	0.091	0.17
	L24	180	330	0.16	0.30

(3)–(6) 5 σ detection limits for a pointed observation: 9 exposure cycles for one filter in a pointing opportunity.
(3)(5) Pole = at Ecliptic pole.
(4)(6) Plane = at Ecliptic plane.
(7) Estimated as the 10 per cent linearity range for an exposure time of 2.3 sec and 0.6 sec for NIR and MIR-S/L, respectively.

Saturation Limits

The saturation limits of the IRC00 mode are given in Table 5.5.14. These limits are defined as the 10 per cent linearity range for the short exposure (2.3 sec and 0.6 sec for NIR and MIR-S/L, respectively) of the exposure cycle.

Table 5.5.14: Saturation limits for IRC00

Camera	Filter	$F_{\rm sat}$
		(mJy)
NIR	N2	780
	N3	250
	N4	360
MIR-S	S7	1800
	S9W	1000
	S11	1800
MIR-L	L15	2500
	L18W	3200
	L24	23000

5.5.4 IRC02: Imaging with Two Filters

Recommended Usage

IRC02 mode is prepared for general purpose imaging observations. This mode can be used at any sky position even in low visibility regions.

Description

A sky position is observed with two filters each of which consist of three images with small position shifts by dither. i.e., this AOT can provide a self-standing data set in just a single pointing. The net exposure time per filter is about 1/3 of IRC00.

Parameters

The filters used in this AOT are fixed as the following. The filter set can cover the whole IRC wavelength range except for that of N2 (wide bands are not included).

Table 5.5.15: Filter combination of IRC02

Camera	NIR	MIR-S	MIR-L
Filter	N3 & N4	S7 & S11	L15 & L24

A parameter specifying the reference to the target position must be given for this AOT.

Table 5.5.16: Target position parameter for IRC02

Code	Description
N	Target position is placed at the center of the NIR/MIR-S cameras.
L	Target position is placed at the center of the MIR-L camera.

Same as IRC00 and IRC03.

5.5.5 Expected Performance

Detection Limits

The expected 5σ detection limits of the IRC02 observing mode are given in Table 5.5.17.

Table 5.5.17: Detection Limits for IRC02

(1)	(2)	(3)	(4)	(5)	(6)
Camera	Filter	Point source		Diffuse source	
		(μJy)		(MJy/sr)	
		Pole	Plane	Pole	Plane
NIR	N3	6.4	7.4	0.025	0.029
	N4	13	15	0.046	0.056
MIR-S	S7	60	82	0.11	0.16
	S11	66	110	0.11	0.18
MIR-L	L15	120	210	0.16	0.29
	L24	310	570	0.29	0.51

(3)–(6) 5 σ detection limits for a pointed observation: 3 exposure cycles per filter in a pointing opportunity. Numbers for N2, S9W, and L18W are only for reference. These filters are not used in the IRC02.
(3)(5) Pole = at Ecliptic pole.
(4)(6) Plane = at Ecliptic plane.

Saturation Limits

The saturation limits of the IRC02 mode are given in Table 5.5.18. These limits are defined as the 10 per cent linearity range for the short exposure (2.3 sec and 0.6 sec for NIR and MIR-S/L, respectively) of the exposure cycle.

Table 5.5.18: Saturation Limits for IRC02

Camera	Filter	Saturation Limit
		(mJy)
NIR	N3	250
	N4	360
MIR-S	S7	1800
	S11	1800
MIR-L	L15	2500
	L24	23000

5.5.6 IRC03: Imaging with Three Filters

Recommended Usage

IRC03 is used for general purpose observing. It observes a target with all three filters of each camera. This mode is *not* recommended for sky areas of low visibility where two pointed observations cannot be guaranteed.

Description

IRC03 is similar to the IRC02 mode but differs in the number of filters and dithering positions in one pointing opportunity. The target sky position is observed by three filters of each camera. Instead, only one *Micro-Scan* (2 dithered images) is applied for each band. To obtain reliable results it is recommended to have sufficient redundancy by observing the same sky position at least twice on different orbits. The net exposure time per filter is thus 2/9 of the IRC00.

Parameters

IRC03 uses all filters of the IRC.

Observers should be reminded that the wavelength coverage of the S9W and L18W filters overlap with the two other filters in the same camera. The advantage of using this mode instead of IRC02 has to be carefully considered from the scientific viewpoint of each observation.

Table 5.5.19: Filter combination of IRC03

Camera	NIR	MIR-S	MIR-L
Filter	N2 & N3 & N4	S7 & S9W & S11	L15 & L18W & L24

The position reference has to be given as with IRC00 and 02.

Table 5.5.20: Target position parameter for IRC03

Code	Description
N	Target position is placed at the center of the NIR/MIR-S cameras.
L	Target position is placed at the center of the MIR-L camera.

Same as IRC00 and 02.

5.5.7 Expected Performance

Detection Limits

Expected 5σ detection limits of the IRC03 observing mode is given in Table 5.5.21.

Table 5.5.21: Detection limits for IRC03

(1)	(2)	(3)	(4)	(5)	(6)
Camera	Filter	Point source		Diffuse source	
		(μJy)		(MJy/sr)	
		Pole	Plane	Pole	Plane
NIR	N2	17	18	0.069	0.076
	N3	7.8	9.1	0.030	0.035
	N4	15	19	0.056	0.069
MIR-S	S7	74	110	0.13	0.19
	S9W	62	100	0.11	0.17
	S11	81	130	0.14	0.22
MIR-L	L15	140	260	0.20	0.36
	L18W	180	330	0.20	0.36
	L24	380	690	0.35	0.63

(3)–(6) 5 σ detection limits for a pointed observation: 2 exposure cycles per filter in a pointing opportunity.
(3)(5) Pole = at Ecliptic pole.
(4)(6) Plane = at Ecliptic plane.

Saturation Limits

The saturation limits of the IRC03 mode are given in Table 5.5.22. These limits are defined as the 10 per cent linearity range for the short exposure (2.3 sec and 0.6 sec for NIR and MIR-S/L, respectively) of the exposure cycle.

Table 5.5.22: Saturation Limits for IRC03

Camera	Filter	Saturation Limit
		(mJy)
NIR	N2	780
	N3	250
	N4	360
MIR-S	S7	1800
	S9W	1000
	S11	1800
MIR-L	L15	2500
	L18W	3200
	L24	23000

5.5.8 IRC04: Spectroscopic mode

Recommended Usage

IRC04 is for spectroscopic observations with the IRC. Observation with this mode can be made in regions of moderate to high visibility which allow two or more pointed observations at each target position.

Description

In this mode, the IRC dispersion elements are used to take spectra of the targets. The MIR-S cameras always use two dispersion elements to cover their full wavelength range. However, due to the loss of the LG1 grism, the MIR-L camera uses LG2 only. This results in an unavoidable gap between 13–18 μm. The wavelength coverage of the NP (moderate resolution) and NG (high resolution) are similar to each other, and the user should choose one of these two for this AOT.

As we explain in section 5.1.5, a slit is provided in each camera in order to observe diffuse radiation. The NIR camera also has an entrance aperture (slit) for a point source, to enable confusion-less spectroscopy. It is used with the NG in high-resolution mode (see below). The point source density in the FoV of the MIR-S/L cameras is expected to be low enough that they will be able to observe point sources directly in the imaging field.

A short exposure image in the N3, S9W, and L18W filters, is taken by each camera respectively, for pointing alignment.

No dithering operation is carried out during one pointing in this AOT. Observers are highly recommended to observe the same area of the sky on two or more independent orbits to ensure data redundancy.

Parameters

The first parameter specifies the dispersion element for the NIR camera.

Table 5.5.23: Dispersion element selection in IRC04

Set	NIR	MIR-S	MIR-L
a	NP (N3)	SG1 & SG2 (S9W)	LG2 (L18W)
b	NG (N3)	SG1 & SG2 (S9W)	LG2 (L18W)

The second parameter gives the position reference for this AOT. It is more complicated than other AOTs because of the presence of the slits. Np and Nh are intended to be used with the NG, and others with the NP. Only the Ns slit can be used with both elements.

Table 5.5.24: Target position parameter for IRC04

Code	Description
	Available for Set a (NP)
Nc	The target position is placed at the center of the NIR/MIR-S (FoV).
Ns	The target position is placed at the common slit of the NIR/MIR-S.
Lc	The target position is placed at the center of the MIR-L (FoV).
Ls	The target position is placed at the slit of the MIR-L.
	Available for Set b (NG)
Ns	The target position is placed at the common slit of the NIR/MIR-S.
Np	The target position is placed at the point source aperture of the NIR.
Nh	The target position is placed at the high-resolution slit of the NIR.

5.5.9 Expected Performance

Detection Limits

Table 5.5.25 and 5.5.26 summarizes 5 σ detection limits of the IRC04 observing mode. These numbers are for 8 exposure cycles, i.e. a single pointing opportunity. Line detection limits are given for integrated line fluxes of an isolated line that can be treated as a point source (by aperture photometry technique at the line position).

Continuum detection limits for point source (slitless or with Np) are per pixel in the direction of dispersion. In other words, they are the flux that provides a $S/N = 5$ signal after being integrated over the pixels along the spatial direction of one row in the spectral dispersion direction. Averaging over the dispersion direction can improve the detection limits with a cost of spectral resolution. q On the other hand, continuum detection limits for diffuse source (with slit) are given per pixel. Integrating over the slit length can improve the sensitivity. If you integrate the spectrum over 0.8 arcmin (about 33 pix), the NP detection limits at the Ecliptic pole can be $0.26/\sqrt{(}33) = 0.045$ [MJy/sr].

These numbers are for the monotonic limit at the wavelength band center. The spectral response functions (RSRF; Figures 5.2.3, 5.2.4, 5.2.6) have to be taken into account for the limits at other wavelengths. Moreover, the spectral resolution changes as a function of wavelength in the case of NP, the prism dispersion element, and this also has to be considered for any detailed estimate of the performance. In this case, the resolution is approximately about 1/4 of the center value (at 3.5 μm) at 2 μm and about twice at 5 μm.

Table 5.5.25: Line Detection Limits for IRC04

Camera	Element	$\lambda_{\rm center}$ (μm)	Position	Point Source (10^{-17} W m^{-2})		Diffuse Source (10^{-17} W m^{-2})	
				Pole	Plane	Pole	Plane
NIR	NP	3.5	Nc	0.18	0.26	—	—
	NP	3.5	Ns	—	—	0.13	0.13
	NG	3.6	Np	0.22	0.27	—	—
	NG	3.6	Ns/Nh	—	—	0.19	0.19
MIR-S	SG1	6.6	Nc	1.3	1.8	—	—
	SG1	6.6	Ns	—	—	0.92	0.94
	SG2	10.6	Nc	1.3	2.0	—	—
	SG2	10.6	Ns	—	—	0.63	0.68
MIR-L	LG1	— N/A —					
	LG2	20.2	Lc	2.2	3.9	—	—
	LG2	20.2	Ls	—	—	0.92	1.1

Table 5.5.26: Continuum Detection Limits for IRC04

Camera	Element	$\lambda_{\rm center}$ (μm)	Position	Point Source (mJy)		Diffuse Source (MJy/sr)	
				Pole	Plane	Pole	Plane
NIR	NP	3.5	Nc	0.05	0.08	—	—
	NP	3.5	Ns	—	—	0.26	0.27
	NG	3.6	Np	0.48	0.60	—	—
	NG	3.6	Ns/Nh	—	—	2.8	2.8
MIR-S	SG1	6.6	Nc	1.8	2.5	—	—
	SG1	6.6	Ns	—	—	3.8	3.9
	SG2	10.6	Nc	2.0	3.3	—	—
	SG2	10.6	Ns	—	—	3.5	3.9
MIR-L	LG1	— N/A —					
	LG2	20.2	Lc	5.5	9.8	—	—
	LG2	20.2	Ls	—	—	7.0	8.4

Saturation Limits

Table 5.5.27: Saturation Limits for IRC04

Band		Line limit (10^{-14} W/m^{-2})	Continuum limit	
			Point source (Jy)	Diffuse source (GJy/sr)
NIR	NP	7.4	2.2	15
	NG	11	24	160
MIR-S	SG1	55	76	230
	SG2	48	77	270
MIR-L	LG1	— N/A —		
	LG2	91	220	680

5.5.10 IRC11: Slow-Scan mode

Recommended Usage

IRC11 is recommended for observations of large areas to moderate depth.

Description

In this mode, the detectors are operated following the same procedure as the All-Sky Survey. As described in Section 5.3.2, the NIR detector is not used in this mode. Observers can choose a pair of filters from the MIR-S and MIR-L camera from three presets.

The scan pattern of IRC11 is identical to that of FIS02. One round trip scanning is carried out in a single pointing opportunity. Two scan speeds, 15 or 30 arcsec/sec are available. See Section 4.4.3 for details.

Parameters

The following three filter sets are available.

Table 5.5.28: Filter combinations of IRC11

Set	NIR	MIR-S	MIR-L
a	N/A	S9W	L18W
b	N/A	S7	L15
c	N/A	S11	L24

The second parameter designates the FoV reference position to be pointed to the target. As for FIS02, the position is regarded as the beginning of the scan.

Table 5.5.29: Target position parameter for IRC11

Code	Description
N	Target position is placed at the center of the NIR/MIR-S cameras.
L	Target position is placed at the center of the MIR-L camera.

The scan speed has to be selected for the third parameter. Current estimates of the scan length in one pointing are approximately 1 and 2 deg for 15 and 30 arcsec/sec, respectively.

Table 5.5.30: Scan speed available for IRC11

Scan speed	15 or 30 arcsec/sec

5.5.11 Expected Performance

Detection Limits

Expected 5σ detection limits of the IRC11 observing mode are given in Table 5.5.31.

Table 5.5.31: Detection limits for IRC11: Slow-Scan mode

(1)	(2)	(3)	(4)	(5)	(6)	(7)	(8)	(9)	(10)
		Point source (mJy)				Diffuse source (MJy/sr)			
Scan speed (arcsec/sec)		15		30		15		30	
		Pole	Plane	Pole	Plane	Pole	Plane	Pole	Plane
MIR-S	S7	11	12	22	23	3.8	4.1	7.3	7.7
	S9W	8	9	14	16	2.3	2.7	4.5	4.9
	S11	8	10	16	18	2.4	2.9	4.5	5.1
MIR-L	L15	13	19	24	30	3.4	4.8	6.2	7.7
	L18W	12	19	21	29	2.6	3.8	4.6	6.0
	L24	44	65	80	100	8.4	11.1	15.6	19

Saturation Limits

Table 5.5.32: Saturation limits for IRC11: Slow-Scan mode

(1)	(2)	(3)	(4)	(5)
		Point source (Jy)		Diffuse source (MJy/sr)
Scan speed (arcsec/sec)		15	30	15 & 30
MIR-S	S7	3.3	6.5	220
	S9W	1.8	3.6	130
	S11	3.0	6.0	130
MIR-L	L15	4.3	8.6	200
	L18W	4.4	8.8	150
	L24	18	23	530

5.6 Notes and Restrictions for the IRC Observations

1. **Bright sources** We believe that bright sources that saturate the detectors will not cause permanent damage. However, very bright sources are known to cause after effects (i.e. latent images, etc.), degrading the performance of the detectors for more than an hour. Therefore, some constraint for observing fields with very bright sources may be given for IRC observations, according to the results obtained in the PV phase.

2. **Effects of South Atlantic Anomaly (SAA)** We believe that the passage through the SAA does not cause serious damage to the detectors. However, detector performance may be significantly degraded immediately after the SAA. Current observation scheduling allocates IRC observations relatively close to the SAA region (say, 5 minutes after the passage). The real SAA region and its influence to ASTRO-F observations will be clear only after the PV phase. Observation of targets very close to the SAA may have to be reconsidered or may even be canceled.

Chapter 6

Data Reduction and Products

This section describes the data handling policy, current scope of the data reduction support and data products. Please note that the data reduction software are under development and only a preliminary plan is explained here. Details of the data handling and data reduction guide will be prepared in the future as User manuals.

6.1 Basic Policy

The basic policy of the ASTRO-F data reduction is the following.

- Processing of the Large Area Surveys, including the All-Sky Survey, is to be carried out in a unique and uniform manner by a dedicated team organized by the ASTRO-F Project with the products being distributed to the users. Released products are different depending on the different surveys.
- The reduction of pointing observation data is the observer's responsibility. The ASTRO-F team will provide the necessary information to handle the data, e.g., calibration data and software to correct instrument related characteristics. Astronomical analysis such as point source extraction should be carried out by commonly available software.

We welcome any users to participate in the data reduction activity at any level of the work, from giving quantitative reports of their data reduction results to proposing new algorithms to the programs.

6.2 Large Area Surveys

6.2.1 All-Sky Survey

6.2.2 ASTRO-F Point Source Catalogues

We plan to release several catalogues with different detection limits, completeness and reliability, during the progress of the data reduction. Release dates in Table 6.2.1 are internal for the ASTRO-F Project team members and are also for purposes of quality control. After one year of internal use, the data will be released to the entire world astronomical community. In the following, *BOS* is the beginning of survey which starts two months after the launch, and *EOS* is the end of survey, estimated to be about 1.5 years after the launch.

A draft of catalogue contents are listed in Table 6.2.1.

Table 6.2.1: ASTRO-F Point Source Catalogues

Catalogue	Team Release	Description
FIS Flux of Known Sources	BOS + 2 month – EOS + 2 month	FIS fluxes of known sources such as IRAS point sources. Released incrementally during the survey.
Bright Source Catalogue (BSC)	EOS+ $\leq$ 1 year	Uniform (but relatively shallow) detection limit over the entire sky. High redundancy resulting in higher reliability.
Faint Source Catalogue (FSC)	BSC + $\leq$ 1.5 year	Data redundancy is used to improve the detection limit. Generated only in regions where such improvement is effective.

BOS: Beginning of Survey; EOS: End of Survey = He boil-off

[**FIS Flux of Known Sources**]

This catalogue will be incrementally provided between BOS + 2 month and EOS + 2 month. The main purpose of this catalogue is a data consistency check with the IRAS and MSX catalogues but it will also provide new flux information beyond 100 μm for bright sources. Hence all the sources in these catalogues should already be known. The catalogue will be used as a prototype for the Bright Source Catalogue.

[**Bright Source Catalogue**]

The Bright Source Catalogue is regarded as the main product of the ASTRO-F All-Sky Survey, and is expected to be released before EOS + 1 year. The catalogue will provide a uniform quality data set over the entire sky. Sources are extracted from each single data scan and then cross-checked. This means that the high-ecliptic latitude regions where a lot of data redundancy is available will have better reliability but no advantage in sensitivity..

[**Faint Source Catalogue**]

This catalogue will be released within 1.5 years after the release of the Bright Source Catalogue but may be provided incrementally. In contrast to the Bright Source Catalogue, and rather similar to the IRAS Faint Source Catalog, all available scans for each area of the sky will be first integrated into a data set, then source extraction will be applied to this merged data. This will improve the detection limits in the more redundant areas,

i.e., the detection limit will not be uniform over the entire sky. This catalogue may be produced only where such processing is deemed to be effective.

Even deeper catalogues may be produced upon the data quality, improvement of the data processing, and scientific requirements.

Note that the above explanation was originally envisaged for the FIS All-Sky Survey. We plan that the IRC All-Sky Survey will follow the same policy and will be released together with the FIS catalogues.

The catalogues are expected to contain millions of sources, resulting in a data size of a few to ten Gigabytes. The data will be distributed primarily via the Internet with a suitable interface for data query. It is planned that the ASTRO-F database will have a standard interface to Virtual Observatory (VO). Subset contents of the catalogue may also be distributed by DVD or other appropriate media.

6.2.3 Image Maps

Release of scientific quality image maps from the ASTRO-F All-Sky Survey data has not been officially decided by the project. This is because we are not convinced that the stability of the instrument performance, especially the dark current level, is good enough to produce useful image maps. A final decision will be made after the PV phase. We expect that imagelets of small patches of the sky can be created relatively easily but large area maps will be more difficult.

Preparation for the creation of the image maps has been started, initially aiming to process pointing observation data and survey data of small sky areas with high redundancy.

Table 6.2.2 shows the preliminary plan for image maps with the ASTRO-F All-Sky Survey data.

Table 6.2.2: ASTRO-F Image Map Products

Products	Area	Description
Crude Map	TBD	For ASTRO-F team internal use only. This map will be used for the verification and testing of the data.
Imagelets	1 deg × 1 deg	Images of interesting small extended sources and regions.
Image Atlas (ver.1)	10 deg × 10 deg	Destriped image maps of wide fields (all-sky) of scientific quality.
Image Atlas (ver.2)	10 deg × 10 deg	Same as ver. 1 but the Zodiacal light is subtracted.

Processed Raw Data

The raw data of the ASTRO-F survey (with the appropriate data processing and calibration) will be available after EOS+5 year when the calibration has been stabilized.

6.3 Pointed Observation Data

In principle, the users will receive the following data set.

- Raw data in appropriate FITS format.
- Automatic Processed results from the data reduction pipeline (hereafter Pipeline output) in the same FITS format. Especially in early stage of the mission, the automatic processing may not be sufficient enough to create scientific quality data. Therefore this output should be regarded as a reference for the user's own data reduction.
- Data reduction Tool Kit package. The package will consist of modules for automatic data processing. A Pipeline with user friendly interface and additional support tools.
- Calibration data appropriate for the data.

Data will be primarily distributed on-line via ISAS's Data ARchive and Transmission System (DARTS). The Tool Kits will be provided via the User Support web page. Details will be given later.

6.3.1 FIS Data Reduction: AOT FIS01, 02

Users will receive raw and Pipeline processed data in the format of time series detector output. All information relevant for the data reduction will be stored in one FITS file along with the data itself. In addition, a simple co-add image created from the data will be attached.

In the early stages (Phase 1), the pipeline for pointed observations is expected to be quite similar to that of the All-Sky Survey. i.e., it does not use data redundancy provided by the round-trip scan efficiently. Such functions will be implemented in later releases, possibly by beginning of Phase 2. The goal for the data quality of the pipeline output is minimum scientific grade; not wrong but with large uncertainties.

Users may want to process the data by themselves with the Tool Kit, following the Pipeline processing steps interactively by adjusting the module parameters.

We will also provide an image construction tool. The minimum function of the tool will be to create a simple co-add map and optionally some kind of destriping algorithm. Data analysis with the images is expected to be made with existing software packages or users' programs. The ASTRO-F project will not support this part of the data reduction.

The software programs are currently developed on IDL 6.1.

6.3.2 FIS Data Reduction: AOT FIS03

As repeated many times, observation with this AOT is challenging and the data reduction is not an exception. Figure 6.3.1 illustrates the data reduction procedure for FTS mode. One of the most critical parts is to determine the centre positions of the interferogram for every detector pixel. The current estimates of the scope is that we will need many cut-and-try efforts. Transients are another critical issue. For the time being an empirical approach is applied for the transient correction. More sophisticated methods will be investigated.

In general, we foresee that substantial experience will be necessary to handle the FIS data, especially for the FTS observations; and therefore, close contact with specialists in the project team will be crucial. There is a plan to organize a "user consortium" to discuss various technical problems and contribute activity to the data reduction.

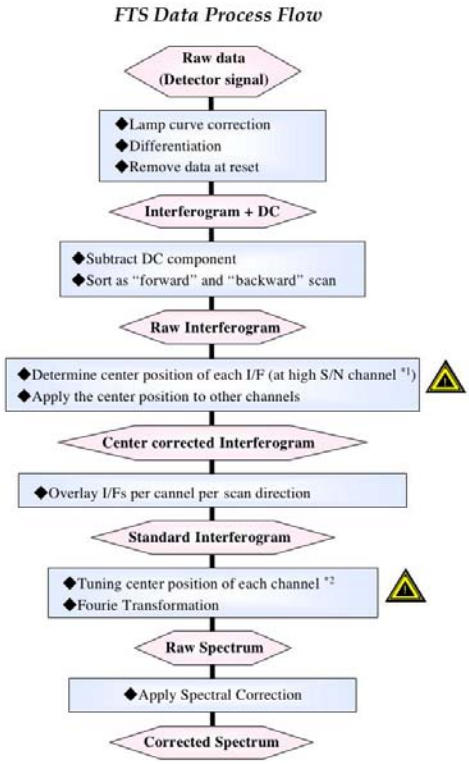

Figure 6.3.1:

6.3.3 IRC Data Reduction: AOT IRC00, 02, 03

IRC imaging mode data reduction is expected to be rather more straightforward following a similar procedure to ground base observations. In addition there will be instrument specific corrections such as removing ghost images and spikes by charged particle hits.

One of the issues to be concerned with is to ensure good quality dark frame and flat-field data. Both will be measured by the instrument team in the calibration dedicated observations through the PV phase and during the observing phases. Therefore, the calibration data will be updated and improved during the mission. Users may want to reprocess the data with updated calibration data by themselves.

Our support is limited to correction and calibration of each observation. We do not plan to support photometry of the calibrated images or mosaicing.

Currently the system is developed in the IRAF environment. Exporting it to IDL is TBD.

6.3.4 IRC Data Reduction: AOT IRC04

Data reduction of this mode is similar to that of the imaging mode for the basic processing of the dark subtraction, despiking, or bad pixel masking etc. In this AOT an image is also taken with one filters per each camera. Source positions are extracted from this image and applied to the spectroscopy images to clip each target.

Several relevant technical issues for the spectroscopic observations are listed below.

- For reliable spectroscopic observations we need accurate and wavelength dependent flat-fielding.

- Wavelength calibration is automatically made by the relationship between imaging position and the spectroscopy data. It also includes distortion correction of the image (Section 5.2.1).
- There may be confusion from nearby targets in the case of observations in crowded regions. Currently these are not decomposed but rather masked in the overlap region for the measurements.
- Measurement of the spectrum is carried out in an aperture on the spectroscopic image. The software attempts to fit an aperture automatically but the user may want to adjust this step interactively.

The tools are being written in IDL.

6.3.5 IRC Data Reduction: AOT IRC11

Data taken by this mode is processed by the pipeline developed for the All-Sky Survey. As for FIS02 (and 01), the pipeline output in the early stage of the mission may not use the data redundancy (round trip scan) efficiently.

Data reduction of this observing mode is still in the investigation phase and details will be given later.

REFERENCES

Fujishiro, N., et al., 2005, Proc. SPIE, in press
Jeong, W.-S., et al., 2003, PASJ 55, 717
Kim, U., et al., 2005, Proc. SPIE, in press
Watanabe, M., 2001, "ASTRO-F Visibility Tool", ASTRO-F internal report, 2001 Sep. 12 (in Japanese)

Appendix A

Confusion Limits and ASTRO-F

A.1 Introduction

The absolute sensitivity of a given space born instrument / telescope system is governed by 2 basic classes of noise; instrumental & photon noise and sky confusion noise. Instrumental noise is intrinsic to the system and is contributed to by such factors as readout noise, dark current fluctuations, flat-fielding uncertainties etc. On the other hand, sky confusion noise is observational dependent and can arise from both the superposition of sources in crowded fields and from extended structures which vary in surface brightness on scales of the telescope and instrument resolution. At infrared wavelengths, the major components are the sky confusion due to interplanetary dust bands (zodiacal light, in the range $5 < \lambda < 60$ μm), the sky confusion due to dust emission from irregular interstellar clouds at high galactic latitudes known as the "infrared galactic cirrus" (Low et al. 1984), confusion due to stars at near infrared wavelengths and the confusion due to the fluctuation of the extragalactic background built up by the superposition of individual faint sources below the resolution of the telescope beam.

Confusion can cause centroid position shifts and flux uncertainties leading to positional errors and spurious sources, therefore careful consideration must be given to the treatment of confusion noise and the confusion limit, as in reality, the confusion noise is a convolution of the observational phenomenon and the observing instrument.

A.2 Confusion due to Infrared Cirrus

The fluctuations in the surface brightness of extended structure on similar scales as the resolution of the telescope/instrument beam can produce spurious events that can be easily mistaken for genuine point sources, since the existence of a source is usually simply derived from the difference in signal between the on source and some background position. Such extended structure is observed in whispy neutral interstellar dust in the Milky Way that is heated by the interstellar radiation field and is known as the infrared cirrus (Low 1984). Cirrus emission peaks at far IR wavelengths (100 μm) but was detected in all 4 IRAS bands (Helou and Beichman 1990). The galactic cirrus is a function of galactic latitude and is serious for wavelengths longer than 60 μm.

Quantatively, this uncertainty in brightness between on source and background positions can be expressed as the second order structure function $C(\theta)$, of the sky brightness, where

$$C(\theta) =< |B(x) - \frac{B(x+\theta) + B(x-\theta)}{2}|^2 >_x, \tag{A.2.1}$$

is the mean difference squared over all on/off pairs, where $B(x)$ is the on source position brightness at x, and $B(x \pm \theta)$ are the off source reference position brightnesses with a separation of θ from the source (2 off source positions to correct for any gradient in the background brightness

emission). Fluctuations on scales of order θ will affect the measurements, the noise due to these fluctuations being given by σ (Jy)= $\Omega\sqrt{C(\theta)}$, where Ω is the solid angle of the measuring aperture such that the limiting noise due to the fluctuation of the sky brightness is given by the value of $C(\theta_o)$ at the resolution limit θ_o of the instrument. Thus in the case of background fluctuations with structure, the measured confusion noise is a function of both the angular separation of the source measurements and the aperture of the instrument.

Gautier et al. (1992) analysed the spatial structure of the IRAS infrared cirrus at 100 μm using the Fourier transform power spectrum of its' fluctuations and found the well known relation between the power, P and scale length, d or its' reciprocal, the spatial frequency, k,

$$P = P_o(\frac{d_o}{d})^{\alpha} = P_o(\frac{k}{k_o})^{\alpha}, \tag{A.2.2}$$

with a power P_o on a scale d_o or corresponding spatial frequency k_o. Empirically, a power spectrum of $\alpha \approx 3$ and relation between the reference power and average sky brightness, $P_o \propto< B(100\ \mu\mathrm{m}) >^3$ was found. Relating the cirrus power spectrum to the structure function, the noise scales as,

$$\sigma \propto P_o^{1/2}(\frac{d}{d_o})^{1-\frac{\alpha}{2}}, \tag{A.2.3}$$

Helou & Beichman (1990) assume the relation $P_o \propto< B >^3$ is true for all wavelengths (replacing $< B(100\ \mu\mathrm{m}) >$ with $< B(\lambda) >$) and taking the scale d as the resolution of a telescope (of diameter D), $\sim \lambda/D$ express the 1σ cirrus confusion noise in equation A.2.3 as,

$$\frac{\sigma(\lambda)}{1\mathrm{mJy}} = 0.732(\frac{\lambda}{100\mu\mathrm{m}})^{2.5}(\frac{D}{0.7\mathrm{m}})^{-2.5}(\frac{< B_\lambda >}{1\mathrm{MJysr}^{-1}})^{1.5}, \tag{A.2.4}$$

Thus the cirrus confusion noise will depend on both the variation of the surface brightness of the background structure and the resolution of the telescope, with the noise becoming less significant for larger aperture sizes such that the next generation of space telescopes (Herschel, SPICA) should not be so severely affected by cirrus confusion over most of the sky. Herbstmeier et al. (1998) have shown that assuming the sky brightness fluctuations and instrumental noise are statistically independent then the total measured noise is $\sigma^2_{tot} \leq \sigma^2_{sky} + 2\sigma^2_{inst}$, thus assuming equality a lower limit for the sky brightness noise can be estimated. Kiss et al (2001) have analysed 40 sky regions with the ISOPHOT instrument on ISO concluding that the cirrus noise was consistent within a factor of 2 to the formulation of Helou & Beichman (1990).

Applying equation A.2.4 to the ASTRO-F FIS instrument and assuming a range of average brightnesses for $< B_\lambda >$ gives us the results for the cirrus confusion noise in Table A.2.1. Note that Jeong et al. (2004) have carried out simulations of the cirrus background for the ASTRO-F FIS wide bands (WIDE-S & WIDE-L). They have concluded that the formula of Helou & Beichman (1990) systematically underestimates the cirrus noise in the dark sky case (< 1 MJy/sr) and overestimates the cirrus noise in the bright sky case (> 3 MJy/sr). Therefore the limits in Table A.2.1 should be treated as lower and upper limits accordingly. Table A.2.2 shows the corresponding estimates extrapolated to the IRC bands,

A.3 The Extragalactic Source Confusion Limit

The galaxy confusion limit is defined as the threshold of the fluctuations in the background sky brightness below which sources cannot be discretely detected in the telescope beam $\sim \lambda/D$. Thus the fluctuation noise arises from the same origin as the galaxies that one is aiming to detect! If we assume galaxies are distributed as a power law in flux, S, down to some detection limit S_{lim},

Table A.2.1: Estimated confusion limits due to galactic cirrus in ASTRO-F FIS bands assuming the model of Helou & Beichman (1990).

Band	Sensitivity	Confusion Limit (5σ, mJy) for $< B_\lambda >$		
	5σ (mJy)	0.5 MJy/sr	3 MJy/sr	10 MJy/sr
N60	600	0.37	5.49	33
WIDE-S	200	0.77	11	68
WIDE-L	400	3.6	54	330
N160	800	4.3	63	388

Table A.2.2: Estimated confusion limits due to galactic cirrus in ASTRO-F IRC bands from the ASTRO-F Large Area Survey (NEP) document.

Band	Sensitivity (600s)	Confusion Limit (5σ, μJy) for $< B_\lambda >$		
	5σ (μJy)	0.5 MJy/sr	3 MJy/sr	10 MJy/sr
N2	7.9	<1	<1	<1
N3	3.7	<1	<1	<1
N4	7.2	<1	<1	<1
S7	32.8	<1	<1	<1
S9W	26.1	<1	<1	<1
S11	37.1	<1	<1	1.6
L15	68.4	<1	1.1	6.9
L18W	87.3	<1	1.6	9.5
L24	180.8	<1	3.1	19

$$N(> S_{lim}) = N_{lim}(\frac{S}{S_{lim}})^{-\alpha}, \tag{A.3.5}$$

where α,is the slope of the integral source counts (where $\alpha = 1.5$ for a Euclidean Universe) and N_{lim} is the number density at the limiting sensitivity S_{lim}. Assuming that the counts flatten at some faint flux, S_0, i.e. $\alpha(S_0) = 0$, then the intensity of the background (in Jy/sr) up to some maximum flux, S_{max}, corresponding to these sources is given by,

$$I = \int_{S_0}^{S_{max}} S\frac{dN}{dS}dS, \tag{A.3.6}$$

The fluctuations contributed by sources below the detection limit S_{lim} are given by the second moment of the differential source counts dN/dS, σ in MJy/sr,

$$\sigma^2 = \int_{S_0}^{S_{lim}} S^2\frac{dN}{dS}dS, \tag{A.3.7}$$

Assuming the power law distribution of sources given in equation A.3.5 and A.3.7 can be evaluated to give,

$$\sigma^2 = N_{lim}S_{lim}^2\frac{\alpha}{2-\alpha}(1 - (\frac{S_0}{S_{lim}})^{2-\alpha}), \tag{A.3.8}$$

For the Euclidean case the dominant sources contributing to the background intensity are those just below the detection limit S_{lim} (Matsuhara et al. (2000), Lagache et al. (2000)). However the strong evolution detected in the galaxy population steepens the source counts and produces super Euclidean slopes in excess of $\alpha > 1.5$ and the sources around the detection limit also contribute significantly to the fluctuations in the background intensity.

Rigorous theoretical definitions of confusion have been presented by Scheuer (1957) and Condon (1974). Hogg (2001) has highlighted the more practical aspects of galaxy confusion noise limitations. An analytical derivation broadly following Franceschini et al (1989) is given below. Note that the clustering of sources will complicate the confusion noise (e.g. as in the case of radio sources, Condon (1974)) although here, for clarity, we do not treat this effect (see Franceschini et al (1989), Takeuchi (2003) for discussions on the effect on the confusion limit of the clustering of sources).

Assuming that the sources are distributed randomly over the sky described by a power law form $N(S) \propto S^{-\alpha}$ and a corresponding differential distribution given by $n(S) = kS^{-\gamma}$ where $\gamma = \alpha - 1$, then the detector response to a source of flux S, at a position (θ, ϕ) from the axis of a detector beam of profile (point spread function) $f(\theta, \phi)$ is given by $x = Sf(\theta, \phi)$. Hence the mean number of responses with amplitudes between x, $x + dx$ in a solid angle $d\Omega$ is given by;

$$R(x) = \int_{\Omega_b} \frac{n(x/f(\theta,\phi))}{f(\theta,\phi)}d\Omega, \tag{A.3.9}$$

where Ω_b is the solid angle of the beam in steradians. Note that for the power law distribution of sources discussed above, equation A.3.9 can be rewritten as,

$$R(x) = kx^{-\gamma}\int_{\Omega_b} f(\theta,\phi)^{\gamma-1}d\Omega = kx^{-\gamma}\Omega_e, \tag{A.3.10}$$

where $\Omega_e = \int f(\theta)^{\gamma-1}d\Omega$ is the effective beam size (Condon 1974). Taking the second moment of the $R(x)$ distribution (the variance) gives the fluctuation of the response,σ ;

$$\sigma^2 = \int_0^{x_c} x^2R(x)dx, \tag{A.3.11}$$

where x_c is a cut off response introduced to stop the variance from diverging at bright source fluxes. More practically the confusion limit x_c (corresponding to a cut off flux S_c) is set to some factor of the confusion noise such that $x_c = q\sigma$, where the factor q limits the largest response included in the evaluation of the confusion noise σ (values of $\sim$5 are assumed in the calculations of Franceschini et al. (1991)). The difference in assuming a cut off in the response as opposed to a cut off in flux is that weak contributions from strong sources are not neglected, as even a strong source far from the axis of the beam may contribute significantly to the point spread function of the beam.

Assuming for clarity in the calculations, a circular Gaussian beam profile, $f(\Theta) = f((\theta/\theta_o)^2) = e^{-4(\theta/\theta_o)^2 ln2}$ such that $d\Theta = 2\theta d\theta/\theta_o^2$ where θ_o is the Full Width at Half Maximum (FWHM) of the beam, integrating equation A.3.11 over the solid angle of the beam gives;

$$\sigma_c^2(x_c) = \pi\theta_o^2 P(x_c) \tag{A.3.12}$$

or

$$\theta_o = \sqrt{\frac{\sigma_c^2}{\pi P(x_c)}}, \tag{A.3.13}$$

where P, effectively the power in the fluctuations, is given by,

$$P(x_c) = \int_0^{x_c} x^2 dx.n(x/f(\Theta))e^{4\Theta ln2} d\Theta, \tag{A.3.14}$$

Thus the confusion limit can be directly related to the FWHM of the instrument beam. For the simple power law representation of the distribution of extragalactic sources given previously and the definitions of equations A.3.9 and A.3.10, the confusion limit is given by,

$$\sigma_c = \sqrt{\frac{k\Omega_e}{3-\gamma}} x_c^{(3-\gamma)/2}, \tag{A.3.15}$$

Therefore, the confusion noise limit will be a complex function of the beam size θ_o, the source counts $N(S)$, the cut off in flux S_c or response x_c and the factor q. For the assumed symmetric Gaussian beam profile, $\sigma_c \propto \theta_o^{(2/(\gamma-1))}$.

Note that the beam size θ (or FWHM, θ_o) $\propto \lambda/D$ where λ is the observation wavelength and D is the telescope diameter. Therefore the confusion due to faint galaxies will be worse at longer wavelengths and smaller telescope diameters. Since the confusion noise is related to the mean number of responses (the source density) and the cut off response q/x_c, a useful, practical benchmark for the confusion limit can be set by limiting the number sources per beam before the beam becomes confused. Ideally the confusion limit would be determined by the flux at which the source density becomes 1 source per beam although more realistically a limit of between 1/20-1/50 sources per beam (20-50 beams per source) is assumed (e.g. Hogg 2001).

In Table A.3.3 and Table A.3.4 the source confusion limits for the ASTRO-F FIS and IRC wavebands respectively are tabulated assuming a confusion threshold of 20 beams per source and a concordance (i.e. flat, dark energy dominated) cosmological world model (H_o = 72 $\mathrm{km\,s^{-1}\,Mpc^{-1}}$, $\Omega = 0.3$, $\Lambda = 0.7$) for the evolutionary model of Pearson (2005). These models are consistent with the estimations of the confusion limits from the early release Spitzer results (Dole et al. 2004). From Table A.3.3 it is clear that source confusion will not be a problem for the All Sky Survey but may become critical for slow scan (pointed) observations with the FIS. In the case of the IRC, the longest wavelengths (15–24 μm) will suffer from source confusion for observations with pointings of the order of a few.

Table A.3.3: Estimated confusion limits (N.B. in mJy) due to point sources for ASTRO-F FIS bands.

	5σ Sensitivity (mJy)		Source Confusion Limit (mJy)
Band	All Sky Survey	Slow Scan Mode	20 beam/source
N60	600	33	3
WIDE-S	200	11	7
WIDE-L	400	8.3	45
N160	800	17	50

Table A.3.4: Estimated confusion limits (N.B. in μJy) due to point sources for ASTRO-F IRC bands.

	Sensitivity (600s) (μJy)	Source confusion limit (μJy)
Band	5σ (μJy)	20 beam/source
N2	7.9	< 1
N3	3.7	< 1
N4	7.2	< 1
S7	32.8	< 1
S9W	26.1	< 1
S11	37.1	2
L15	68.4	16
L18W	87.3	66
L24	180.8	134

REFERENCES

Condon, J.J., 1974, ApJ 188, 279
Dole H. et al., 2004, ApJSS, 154, 93
Franceschini, A., Toffolatti, L., Danese, L., De Zotti, D., 1989, ApJ 344, 35
Franceschini, A., Toffolatti, L., Mazzei, P., Danese, L., De Zotti, D., 1991, A&ASS 89, 285
Helou G., BeichmanC.A., 1990, The confusion limits to the sensitivity of sub-mm telescopes, In: From Ground-Based to Space-Borne Sub-mm Astronomy, Proc. of the 29th Liege International Astrophysical Coll., ESA pub. 117
Gautier, T.N., Boulanger, F., Perault M., Puget J.L., 1992, AJ 103, 1313
Herbstmeier, U. et al., 1998, A&A 332, 739
Hogg, D., 2001 AJ, 121, 1207
Jeong, W.S., et al., 2005, MNRAS 357, 535
Kiss, Cs., Abraham, P., Klaas, U., Juvela, M., Lemke, D., 2001, A&A 379, 1161
Lagache, G., & Puget, J.L., 2000, A&A 355, 17
Low, F.G., et al., 1984 ApJ, 278, L19
Matsuhara, H. et al., 2000, A&A 361, 407
Pearson C.P., 2005, MNRAS 358, 141
Scheuer, P.A., 1957, Proc. Cambridge Phil. Soc. 53, 764
Takeuchi T.T., Ishii T.T., 2004, ApJ, 604, 40
Vaisanen, P., Tollestrup, E.V., Fazio, G.G., 2001, MNRAS 325, 1241

Appendix B

ASTRO-F Cookbook for Open Time Observations

B.1 Introduction

In order to aid observers with the preparation of proposals for Open Time, we present in this section two worked examples for observation and submission of Open Time proposals with ASTRO-F. We show

1- Imaging of extragalactic fields with IRC + FIS

2- Spectroscopy of a galactic target with IRC

In general the preparation of Open Time proposals follows the algorithm below using dedicated tools available via a web interface. In addition we expect users to iterate their observations using the tools before their final submission in order to obtain the best possible observation strategy.

1- Target selection and visibility check

2- Preparation of the "Target list"

3- Validation check of the "Target list"

4- Run Duplication Check Tool

5- Run Instrument Performance Tool (IPT)

6- Submission via Submission Tool

Table B.2.1: Extragalactic target fields for observations with ASTRO-F

Name	Equinox	R.A.	Dec.
ISO FIRBACK MARANO	J 2000	03:11:00.0	−54:45:00.0
UKIDSS-UDS	J 2000	02:21:20.0	−04:30:00.0
SST GOODS-SVF	J 2000	16:09:52.0	+54:55:00.0
HST-N	J 2000	12:36:49.9	+62:12:58.0

B.2 Example 1: Imaging of extragalactic fields with the IRC and FIS

In this worked example we consider a program to image several deep extragalactic fields with the ASTRO-F IRC & FIS instruments. We will simulate the preparation of the proposal from scientific background to proposal submission.

B.2.1 Scientific Background

Studies with the Infrared Space Observatory (ISO), of the Hubble Deep Fields have revealed star formation rates at least comparable to, or higher than those of optical/UV studies (Mann et al. 2002). At submillimetre wavelengths, surveys with SCUBA on the JCMT have revealed a large (>3000 deg^{-2} at $S850 > 2$ mJy) strongly evolving population of sources with bolometric luminosities $> 10^{12}$ L$_o$ and star formation rates of $\sim$ 300–1000 M$_\odot$ yr^{-1} with a median redshift of 2.4 (Chapman et al. 2003). The star formation rate at z$\sim$1 requires significant evolution in the IR galaxy population from the current epoch. Deep observations with the Spitzer Space Telescope have confirmed this strong evolution in the galaxy population out to ISO redshifts and furthermore provided insight into the higher redshift Universe in the so called redshift desert z$\sim$ 1–3 (Papovich et al. 2004). To connect the local and intermediate redshift IRAS/ISO Universe to the higher and high z Universe observed by Spitzer and SCUBA, comprehensive multiwavelength imaging is required throughout the extragalactic populations. Observations with ASTRO-F can observe the full infrared wavelength range in 13 bands from 2–180 μm, fill in the area in the Spitzer wavelength desert between 8–24 μm to much higher sensitivities than obtained in the previous ISO surveys (Elbaz et al 2002). Our targets are the sources responsible for the strong evolution seen in the ISO counts. Although at fainter fluxes the sources responsible for the counts are thought to be luminous infrared galaxies (LIRGs) the identity of the sources at brighter fluxes at the upturn in the counts are not so clear. Depending on the various flavours of evolutionary scenario, they could be M82-like starburst galaxies or more luminous ARP 220-like ultraluminous galaxies (ULIRGs). We would like to test the latter possibility. Therefore our targets will be any ULIRG sources lying in the redshift range 0.5–1 since the redshift distribution of the ISO sources has a median value at around z$\sim$ 0.8. For our program we will chose a set of well known fields where there is already a lot of follow up data. These are the ISO-FIRBACK field, UKIDSS-UDS field, the SST-GOODS-SVF field and the HST-N field. These fields are summarized in Table B.2.1.

B.2.2 Selection of Target Field and Target Visibility

A Visibility Tool is provided that gives an approximate estimation of the open time visibility of the target field during the Phase 2 of the ASTRO-F mission. Note that only 30% of the total number of pointings with ASTRO-F is reserved for open time which translates roughly into 6 orbits every 2 days or almost a 2 degree interval on the ecliptic longitude. In addition to this any orbits not scheduled for the guaranteed time programs are available for *scheduling* for open time. However, visibility for specific targets is quite heavily constrained and an extremely strong function of ecliptic latitude. The visibility given by this tool is calculated under the following assumptions.

1- The instrument is of 10 arcmin width and at the boresight.

2- The nominal scan path along the great circle is considered with ±1 degree offset control.

3- The Moon and SAA orbits have been removed.

4- The maximum number of pointed observations at any single pointing has a ceiling set at 50.

Note that ASTRO-F has the capability to observe ±1 degree either side of the canonical scan path (known as the *offset control*), thus there is some limited flexibility in the available number of pointings per target although this number cannot be guaranteed in practice. Therefore the numbers given by the visibility tool should be considered a guideline as to the absolute maximum observing opportunities for any given target.

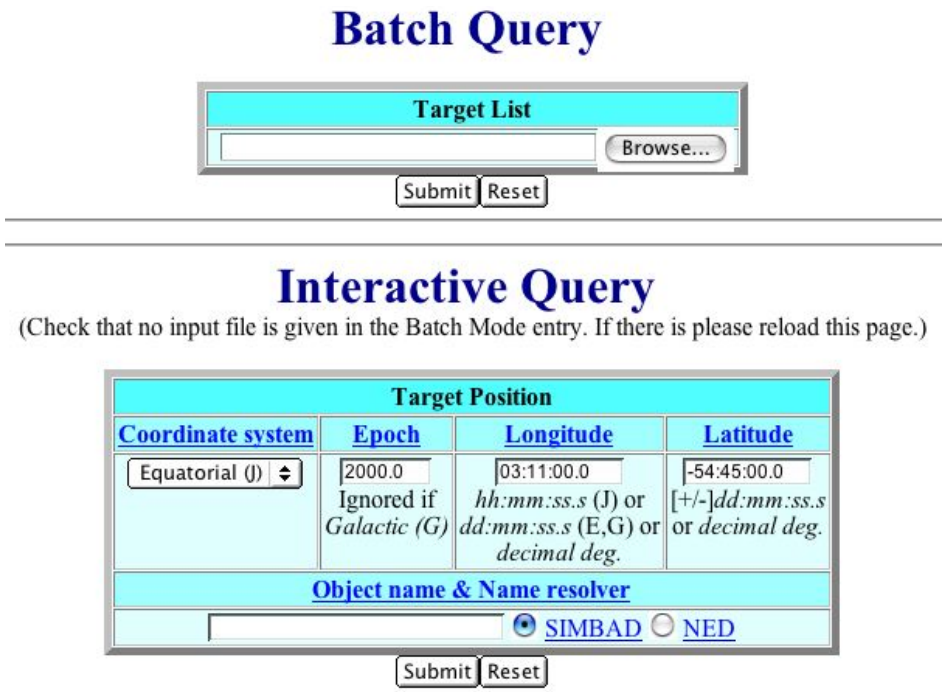

Figure B.2.1: The Visibility Tool user front end.

In general, if the number of targets we want to observe is small we can manually input these co-ordinates into the Visibility Tool, alternatively we can provide the full target list as a batch file: preparation of this list is explained in the next section. Figure B.2.1 shows the batch & interactive query page for the Visibility Tool with one of our fields as an entry. We have selected equatorial co-ordinates in this case. Alternatively, selecting batch mode we will be prompted for a target List file to upload. The results of the Visibility Tool for all our fields (i.e. using batch mode) are shown in Figure B.2.2. The input data from Table B.2.1 is shown on the right hand

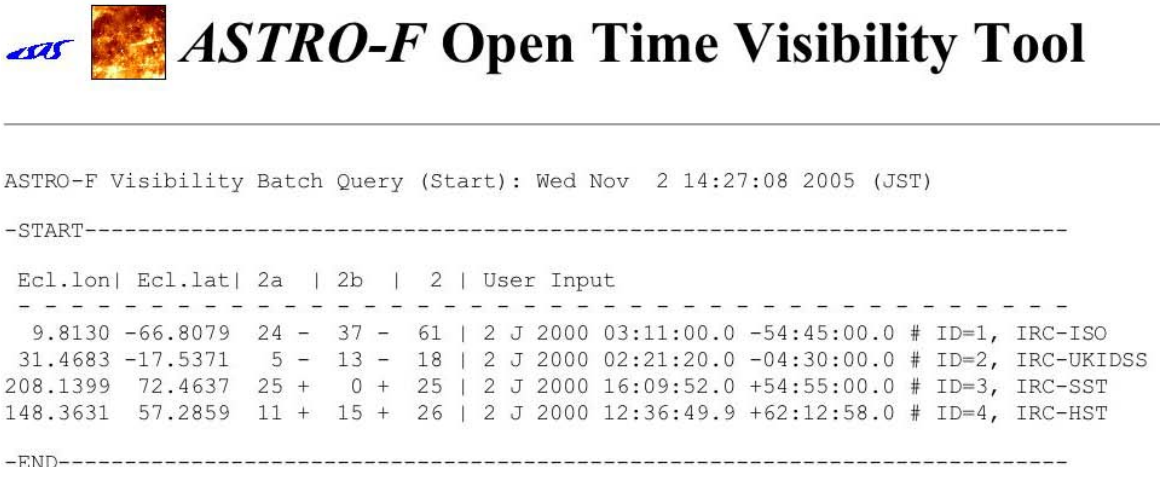

ASTRO-F Open Time Visibility Tool

```
ASTRO-F Visibility Batch Query (Start): Wed Nov  2 14:27:08 2005 (JST)

-START------------------------------------------------------------------------

 Ecl.lon| Ecl.lat| 2a  | 2b  |  2 | User Input
 - - - - - - - - - - - - - - - - - - - - - - - - - - - - - - - - - - - - - - -
  9.8130 -66.8079  24 -  37 -  61 | 2 J 2000 03:11:00.0 -54:45:00.0 # ID=1, IRC-ISO
 31.4683 -17.5371   5 -  13 -  18 | 2 J 2000 02:21:20.0 -04:30:00.0 # ID=2, IRC-UKIDSS
208.1399  72.4637  25 +   0 +  25 | 2 J 2000 16:09:52.0 +54:55:00.0 # ID=3, IRC-SST
148.3631  57.2859  11 +  15 +  26 | 2 J 2000 12:36:49.9 +62:12:58.0 # ID=4, IRC-HST

-END--------------------------------------------------------------------------
```

Figure B.2.2: Results from the Visibility Tool. The input data is shown on the right hand side and the output on the left. The output lists the co-ordinates in ecliptic format which is more suitable for the ASTRO-F orbit and the number of pointings available in Phase 2a (first 6 months after Phase 1), Phase 2b (4 months following Phase 2a) and the total number of pointings available for open time observations in the entire Phase 2 of the mission. The '+' & '-' signs refer to the scan direction: corresponding to the FoV moving from North to South in Ecliptic coordinates for the '+' case and in the opposite direction for the '-' case.

side and the output on the left.

The output lists the query input on the right hand side and on the left, the target co-ordinates in the ecliptic system, which is more suitable for the interpretation of the visibility and the total number of pointings available for open time in Phase 2 of the mission. The number of pointings are also broken down into categories of total number of orbits available in Phase 2a (first 6 months of Phase 2) and Phase 2b (next 4 months of Phase 2). The '+' & '-' signs refer to the scan direction: corresponding to the FoV moving from North to South in Ecliptic coordinates for the '+' case and in the opposite direction for the '-' case.

The visibility (i.e. number of times the field can be observed during phase 2) of our fields are 61, 18 ,25 & 26 respectively during Phase 2. At an ecliptic latitude of -17.5, the UDS field has rather low visibility with ASTRO-F and it may be unlikely that we will be able to carry out all the pointings with the FIS and IRC instruments as desired. Therefore, we shall drop this field and concentrate on the remaining three fields.

The output from the visibility tool should be saved as an ASCII file as it will need to be uploaded as part of the final submission process for our proposal.

B.2.3 Preparation of Target List

The objective of the IRC observations is to detect the emission from the mid-infrared dust features (PAH features in dusty ULIRGs to $z \sim 1$). Thus to fully sample these features over this redshift range we will require as many bands as possible. The IRC has 3 AOTs for imaging, IRC00 is for deep imaging in a single band and requires 3 pointed observations to ensure adequate dithering (moreover 2 bands are recommended so the total number of pointings required will increase to 6). Since we are more interested in spectral coverage we should choose either IRC02 or IRC03. IRC03 will give us the maximum number of filters (all of them) so we select this. IRC03 has only one micro-scan for each band and therefore we need to observe the same field twice for sufficient redundancy. We conservatively set the number of pointings for each IRC AOT to 3, which will will check and confirm at a later stage with the Instrument Performance Tool.

For the FIS, we wish to observe the emission from the dust hump from the ULIRGs in our target fields out to a redshift of around unity. We need to cover the IRC field of view (FoV) described above (10 arcmin $\times$ 10 arcmin), therefore we do not require a particularly long scan but rather need to scan an area somewhat wider than the FIS detector array. Therefore we select AOT FIS01 over FIS02 since the former gives us the option of a cross scan shift. The FIS01 AOT has several parameters that we need to set. The first is the scan speed and the second is the cross-scan shift. Furthermore, setting these parameters determines the scan length. AOT FIS01 includes 2 round trip scans with a cross-scan shift. Therefore there will be uneven coverage of our FoV with the central part being covered by the full 2 round trip scans while the edges will be covered by a single round trip scan only, thus the central region will have a better sensitivity by a factor of $\sqrt{2}$. The cross-scan shift can be either 70 or 240 arcsec, a smaller step will increase the cross-scan area covered on both scan trips (7–4 arcmin respectively) but decrease the overall area covered by the scan. We need to cover the 10 arcmin area of the IRC FoV so we choose a scan step of 70 arcsec with a speed of 15 arcsec/s (resulting in a scan length of 20 arcmin and a cross scan coverage of 7 arcmin) and make 2 slightly overlapping pointings with FIS01 to completely cover the IRC FoV with the FIS. A tool (iris_sky) is provided to aid us with the positioning of the instruments over our fields. With iris_sky we can project our instrument arrays onto our target fields (on images from IRAS and 2MASS). With iris_sky it is also possible to create our target list in its' entirety although we shall construct ours manually in this case. Figure B.2.3 shows how to input the field and AOT details into the iris_sky tool and Figure B.2.4 shows the output with the array field of view with from top left to bottom right, the NIR/MIR-S camera, MIR-L camera and the 2 FIS scans respectively overlaid on the target field.

Once the AOTs have been selected we can go ahead and prepare the target list for our observations. An ASTRO-F target list contains 1 line per target per AOT per field of view. We are observing our target fields with the IRC MIR-L camera, the IRC NIR/MIR-S camera and twice with the FIS, therefore we have 4 lines in our target list per target field. We have 3 target fields, therefore we have a total of 12 lines in our target list. The target list is shown in Table B.2.2. The target list consists of a unique I.D. in ascending but not necessarily contiguous order, followed by some identifier for the target name which should if possible be a resolvable by systems such as SIMBAD, NED. The next 3 fields are reserved for the coordinate system and target coordinates. For both the IRC03 AOT and the FIS01 AOT, the target position is at the centre of the FoV (note that for the FIS02 AOT, it would be at the beginning of the scan). Next we need the AOT, which will be either IRC03 or FIS01. Following the AOT are the specific parameters for each given AOT. For the IRC imaging, we have to specify 2 parameters, the filter combination and the camera with which we want to observe. For the IRC03 AOT the filter combination is fixed - all of them - so we can fix the first parameter as *a*.

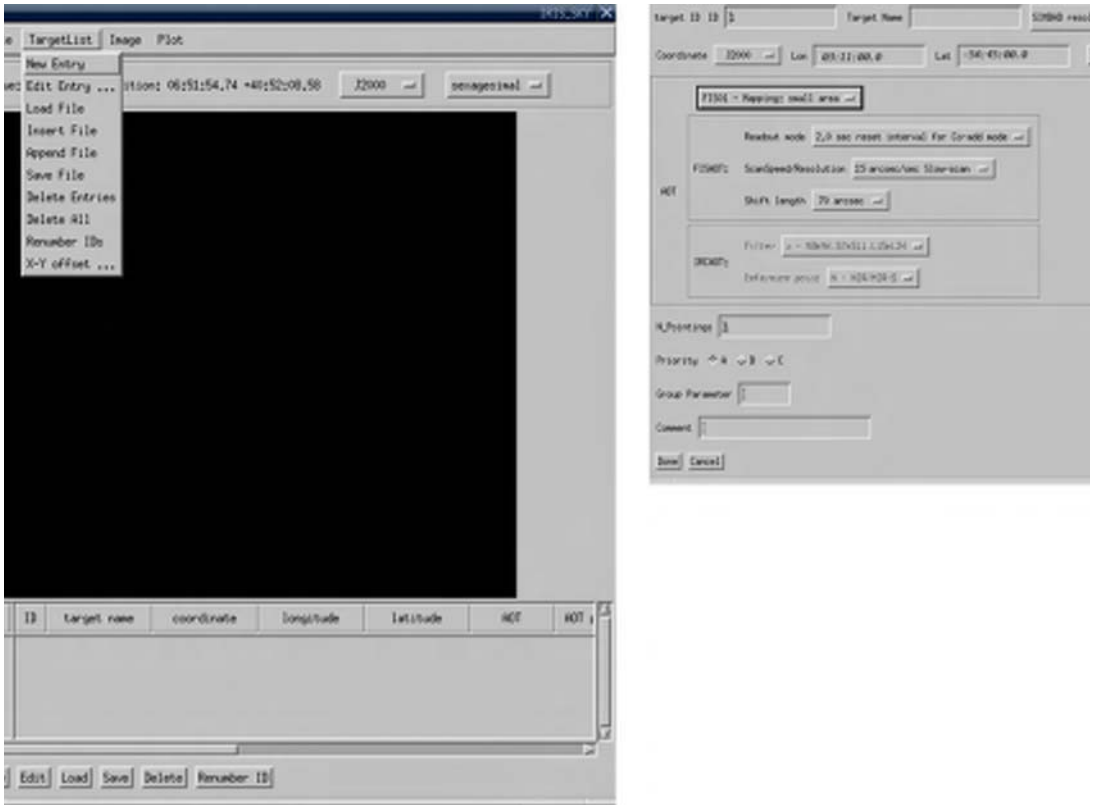

Figure B.2.3: The steps to set up the iris_sky tool. Selecting new entry opens a dialogue box. The target position can then be entered as well as the AOT details.

The second parameter is either L or N depending on whether we are observing with the MIR-L or NIR/MIR-S respectively. Since we are observing in all 9 bands we have 2 lines in our target list, one for each IRC FoV. For the FIS, it is a little more complex, we have 3 parameters to set for the AOT, the reset interval, scan speed and the cross-scan step. We have already discussed the latter pair of parameters and have set them to *15 arcsec/s* and *70 arcsec* respectively. The choice of reset interval (0.5, 1 or 2s) depends on what we are observing. In general a longer reset interval improves sensitivity but increases the chance of saturation. For our case, we do not expect extremely bright sources and would like to get right down to the galaxy confusion limit, hence we select the longest reset interval of *2s*.

In the following field we input the number of pointings for each AOT, for our case this will be 3 for each IRC03 AOT and 1 for each FIS01 scan. We then have to prioritize our targets. ASTRO-F Open Time Observations are divided into 3 priorities, A , B, C . Our A & B targets, barring any unforeseen events, should be observed, while the priority C targets should be considered as back-ups. In our target list, the number of priority A , B, C targets should be around the same. For our observations we prioritize by target field although we could just as easily prioritize the FIS observations over the IRC observations for all our fields instead for example. We choose to prioritize our fields by their visibility first and then by possible duplication conflict (see the discussion on duplication later) with the HST field as our back up priority C target due to a duplication conflict.

ASTRO-F supports the concept of "symbiotic observation". This option in the penultimate field of the target list entry (field 10) enables the observers to specify that more than 2 pointings

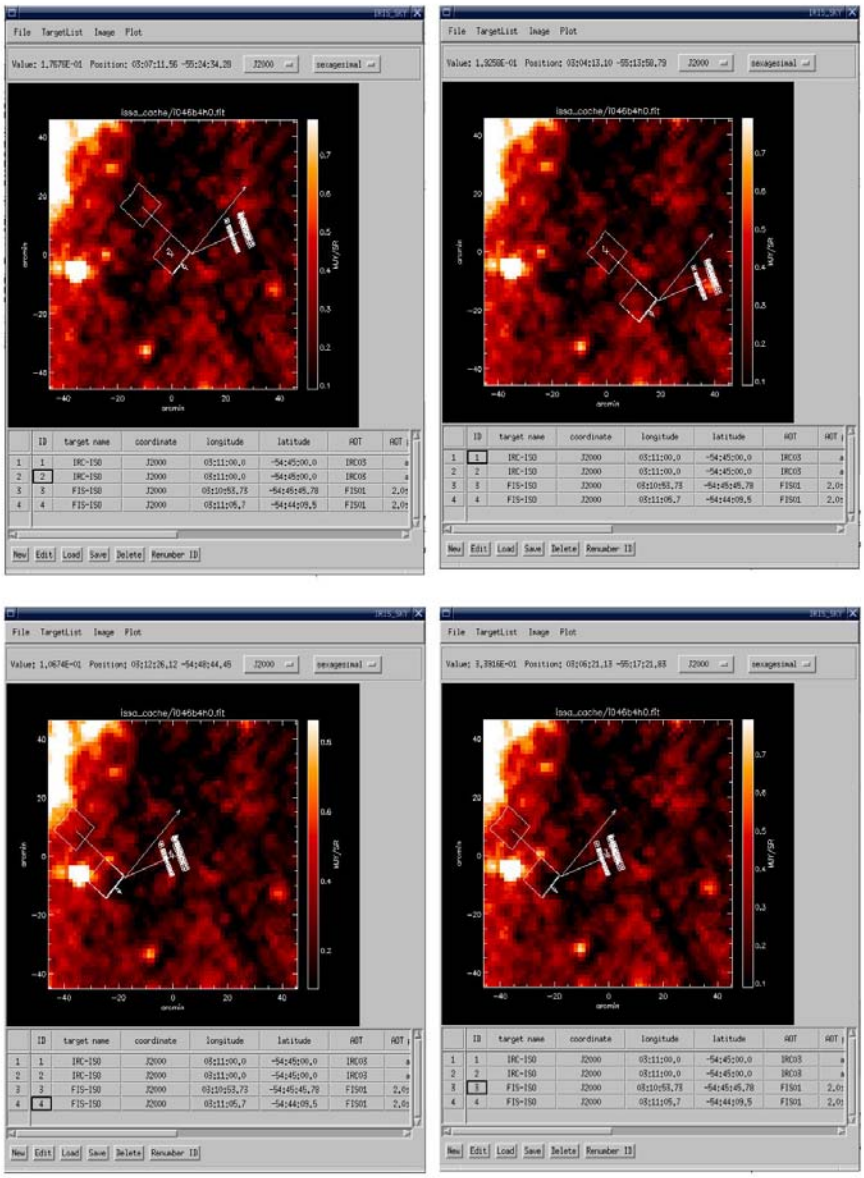

Figure B.2.4: Using the iris_sky tool to overlay the arrays and FoV of the instruments on our target fields. From top left to bottom right with the NIR/MIR-S camera, MIR-L camera and the 2 FIS scans respectively overlaid on the target field.

are required to complete an observation. This may be set, for example, for observations at the same position but with different instruments, or for mapping large areas. When this parameter is given, however, it will constrain the observation plan significantly and increases the risk that the observations will not be scheduled at all. If we schedule any of our observations as symbiotic we would group them together with a Group ID number and an observational style as *"1;o"* . The second parameter being either *o* or *a* , where *o* means one of the observation is acceptable and *a* means either all or none is acceptable. For our targets, we could still get useful information

Table B.2.2: Target List for submission

1, "IRC-ISO", "J2000", 03:11:00.0, -54:45:00.0, "IRC03", "a;L", 3, A, , "ISO FIRBACK MARANO"
2, "IRC-ISO", "J2000", 03:11:00.0, -54:45:00.0, "IRC03", "a;N", 3, A, , "ISO FIRBACK MARANO"
3, "FIS-ISO", "J2000", 03:10:53.73, -54:45:45.78, "FIS01", "2.0;15;70", 2, A, , "ISO FIRBACK MARANO"
4, "FIS-ISO", "J2000", 03:11:05.7, -54:44:09.5, "FIS01", "2.0;15;70", 2, A, , "ISO FIRBACK MARANO"
5, "IRC-SST", "J2000", 16:09:52.0, +54:55:00.0, "IRC03", "a;L", 3, B, , "SST GOODS-SVF"
6, "IRC-SST", "J2000", 16:09:52.0, +54:55:00.0, "IRC03", "a;N", 3, B, , "SST GOODS-SVF"
7, "FIS-SST", "J2000", 16:09:47.01, +54:55:33.08, "FIS01", "2.0;15;70", 2, B, , "SST GOODS-SVF"
8, "FIS-SST", "J2000", 16:09:56.88, +54:54:27.54, "FIS01", "2.0;15;70", 2, B, , "SST GOODS-SVF"
9, "IRC-HST", "J2000", 12:36:49.9, +62:12:58.0, "IRC03", "a;L", 3, C, , "HST-N"
10, "IRC-HST", "J2000", 12:36:49.9, +62:12:58.0, "IRC03", "a;N", 3, C, , "HST-N"
11, "FIS-HST", "J2000", 12:36:40.3, +62:14:08.7, "FIS01", "2.0;15;70", 2, C, , "HST-N"
12, "FIS-HST", "J2000", 12:36:59.4, +62:11:47.3, "FIS01", "2.0;15;70", 2, C, , "HST-N"

even with a partial observation so we do not want the extra constraint of symbiotic observation, therefore we will leave the field blank (not forgetting the "comma" field separator). Finally, any notes are appended on the end of each target list line. Our final target list is shown in Table B.2.2.

B.2.4 Target List Validation

Once the target list has been completed, we can proceed towards the submission stage. However there are still a few steps to complete. We should run our target list through both the Target List Validation Tool and then we need to submit the target list to the observation Duplication Check Tool.

The Target List Validation Tool takes a target list and makes a simple check on the target list format, e.g. correct number of fields, AOT in expected form etc. It does not perform any test on the scientific validation, e.g. on position or sensitivity etc. We can submit the Target List as a batch file in a similar manner to the Visibility Tool as in Figure B.2.5, in fact this (target list) format is accepted by all tools during the submission process. Figure B.2.6 shows the output of the Target List Validation Tool. Any errors would be highlighted in red and a summary given at the bottom of the output.

The target list will be automatically validated when we upload it during the final proposal submission stage so there is no need for us to save the output of the Validation Check Tool.

Figure B.2.5: Input to the Target List Validity Checker

```
1, "IRC-ISO", "J2000", 03:11:00.0, -54:45:00.0, "IRC03", "a;L", 3, A, ,  "ISO FIRBACK MARANO"

2, "IRC-ISO", "J2000", 03:11:00.0, -54:45:00.0, "IRC03", "a;N", 3, A, ,  "ISO FIRBACK MARANO"

3, "FIS-ISO", "J2000", 03:10:53.73, -54:45:45.78, "FIS01", "2.0;15;70", 2, A, ,  "ISO FIRBACK MARANO

4, "FIS-ISO", "J2000", 03:11:05.7, -54:44:09.5, "FIS01", "2.0;15;70", 2, A, ,  "ISO FIRBACK MARANO"

5, "IRC-SST", "J2000", 16:09:52.0, +54:55:00.0, "IRC03", "a;L", 3, B, ,  "SST GOODS-SVF"

6, "IRC-SST", "J2000", 16:09:52.0, +54:55:00.0, "IRC03", "a;N", 3, B, ,  "SST GOODS-SVF"

7, "FIS-SST", "J2000", 16:09:47.01, +54:55:33.08, "FIS01", "2.0;15;70", 2, B, , "SST GOODS-SVF"

8, "FIS-SST", "J2000", 16:09:56.88, +54:54:27.54, "FIS01", "2.0;15;70", 2, B, , "SST GOODS-SVF"

9, "IRC-HST", "J2000",  12:36:49.9, +62:12:58.0, "IRC03", "a;L", 3, C, ,  "HST-N"

10, "IRC-HST", "J2000", 12:36:49.9, +62:12:58.0, "IRC03", "a;N", 3, C, ,  "HST-N"

11, "FIS-HST", "J2000",  12:36:40.3,  +62:14:08.7, "FIS01", "2.0;15;70", 2, C, ,  "HST-N"

12, "FIS-HST", "J2000",  12:36:59.4, +62:11:47.3, "FIS01", "2.0;15;70", 2, C, ,  "HST-N"


### Pointings ... Total=30 : A=10 B=10 C=10
### Format error=0

Validation check: 2005/11/02 16:35:13
< iris_help @ ir.isas.jaxa.jp >
```

Figure B.2.6: Output from the Target List Validation Tool. Any Errors would have been marked in red and the number of errors would have been listed at the bottom of the output in the Pointings summary.

B.2.5 Duplication Check Tool

Duplicate observations are decided on a basis of position, instrument/AOT and the number of pointings. Figure B.2.7 shows the input screen for the Duplication Check Tool. Full results or summary output can be selected, where selecting full results would give details of the conflicting guaranteed time (Mission Programmes) observations for each duplicated observation in our target list. Putting our target list into the Duplication Check Tool and selecting summary for the out put, we find that indeed there is a conflict of position or instrument for 5 of our observations in 2 of our fields (see Figure B.2.8), however since the AOT is different it is not strictly a duplicate observation, the TAC will have to look into the scientific justification to decide whether our observation is unique.

The output from the Duplication Check tool should be saved as an ASCII file as it will need to be uploaded as part of the final submission process for our proposal.

Figure B.2.7: Input screen for the Duplication Check Tool. The input is the target list as usual. Full results or summary output can be selected.

ASTRO-F Duplication Check tool results

-START----------

Duplication summary

ID	cor	ra/lon	dec/lat	AOT	Target name	P+AOT	P+Inst	Pos	Result
1	J2K	47.7500,	-54.7500	IRC03	IRC-ISO	0	0	0	OK
2	J2K	47.7500,	-54.7500	IRC03	IRC-ISO	0	0	0	OK
3	J2K	47.7239,	-54.7627	FIS01	FIS-ISO	0	0	0	OK
4	J2K	47.7737,	-54.7360	FIS01	FIS-ISO	0	0	0	OK
5	J2K	242.4667,	54.9167	IRC03	IRC-SST	0	0	0	OK
6	J2K	242.4667,	54.9167	IRC03	IRC-SST	0	0	0	OK
7	J2K	242.4459,	54.9259	FIS01	FIS-SST	0	0	3	Duplication
8	J2K	242.4870,	54.9076	FIS01	FIS-SST	0	0	0	OK
9	J2K	189.2079,	62.2161	IRC03	IRC-HST	0	3	0	Duplication
10	J2K	189.2079,	62.2161	IRC03	IRC-HST	0	3	0	Duplication
11	J2K	189.1679,	62.2358	FIS01	FIS-HST	0	0	3	Duplication
12	J2K	189.2475,	62.1965	FIS01	FIS-HST	0	0	3	Duplication

-END----------

Format Description

Figure B.2.8: Results from the Duplication Checker Tool. We see that 5 of our observations are in conflict with the guaranteed time on ASTRO-F. The *green* denotes a conflict in position whilst the red denotes a conflict in position and instrument. Duplication can be made on position, instrument, AOT and the number of pointings.

Table B.2.3: Observation Details file for the Instrument Performance Tool. Columns are ID number, Target name, Band, flux in mJy, signal/noise, number of pointings (blank) and type of source point/diffuse/line.

1,"IRC-ISO", L15, 90,5., ,P
1,"IRC-ISO", L18W, 200,5., ,P
1,"IRC-ISO", L24, 300,5., ,P
2,"IRC-ISO", N2, 5,5., ,P
2,"IRC-ISO", N3, 5,5., ,P
2,"IRC-ISO", N4, 10,5., ,P
2,"IRC-ISO", S7, 50,5., ,P
2,"IRC-ISO", S9W, 50,5., ,P
2,"IRC-ISO", S11, 50,5., ,P

B.2.6 Estimation of Sensitivity for IRC

The typical flux densities for the colder ULIRGs in the mid-infrared are around one to a few 100 μJy in the 15–24 μm range dropping to 10's μJy in the 7–12 μm range (see Figure B.2.11). A performance estimator tool is available to calculate the number of pointings required for a given specific AOT, target sensitivity and desired signal to noise. The Instrument Performance Tool requires the Target List and an Observation Details file to be combined as in Figure B.2.9. The Observation Details file includes an identifier for each separate AOT, the target name, AOT, band, required sensitivity in micro-Jy, signal to noise, number of pointings and whether we are observing a point, diffuse source, lines etc. One of either, *sensitivity*, *signal/noise*, *number of pointings* is omitted in our input list and this is what will be calculated by the Instrument Performance Tool. The Observation Details file for the Instrument Performance Tool, for the FIRBACK-Marano field is shown in Table B.2.3.

Putting these values into the Instrument Performance Tool, the output in Figure B.2.10 is returned and from this we find that we would require around 3 pointings in each band of the IRC using AOT IRC03. Note that the field that has been calculated by the IPT is marked with an asterisk for clarity. The output from the Instrument Performance Tool also gives us a warning for the L18W band that we require more than 1 single pointing to complete this AOT. The 3 pointing 5 σ detection limits are overlaid on a typical $z \sim 0.8$ cold ULIRG in Figure B.2.11. Not forgetting that the IRC MIR-L does not share the same field of view as the IRC NIR/MIR-S, this means that to cover our chosen target field we require 3 pointings $\times$ 2 FoV = 6 pointings in total with the IRC.

B.2.7 Estimation of Sensitivity for FIS

For the FIS, we wish to observe the emission from the dust hump from the ULIRGs in our target fields out to a redshift of around unity. For this we need to cover the IRC field of view described in the previous section (10 arcmin $\times$ 10 arcmin) down to a sensitivity of around 20 mJy and 50 mJy in the short and long wavelength FIS bands respectively. The Observation Details file for the Instrument Performance Tool, for the FIRBACK-Marano field is shown in Table B.2.4 assuming a single pointing in FIS01. From the Instrument Performance Tool (Figure B.2.12) we see that we can obtain our desired sensitivity (except in the N60 band but we shall live with that) in a single pointing of the FIS under FIS01 with a scan speed of 15 arcsec/s. We also get a warning for the 2 wide bands, notifying us that we are dangerously near the confusion limit for point sources and diffuse cirrus emission for these observations. Note that since we input the number of pointings as a parameter for the FIS observations, the Instrument Performance Tool has marked the calculated flux with an asterisk. The resulting sensitivity from the Instrument

Figure B.2.9: Input screen for the Instrument Performance Tool. Two files are required: the target list and an observation details file.

Performance Tool is shown overlaid on a typical $z \sim 0.8$ cold ULIRG in Figure B.2.11.

The output from the Instrument Performance Tool should be saved as an ASCII file as it will need to be uploaded as part of the final submission process for our proposal.

ID	TARGET	COORD	AOT	BAND	FLUX	SNR	#POINTINGS	SOURCE/ FLUX TYPE
1	IRC-ISO	03:11:00.0 -54:45:00.0	IRC03	L15	9.00e+01 microJy	5	3*	P
Warning! It is strongly recommended to repeat at least 2 pointings for IRC03:								
1	IRC-ISO	03:11:00.0 -54:45:00.0	IRC03	L18W	2.00e+02 microJy	5	1*	P
1	IRC-ISO	03:11:00.0 -54:45:00.0	IRC03	L24	3.00e+02 microJy	5	2*	P
2	IRC-ISO	03:11:00.0 -54:45:00.0	IRC03	N2	5.00e+00 microJy	5	12*	P
2	IRC-ISO	03:11:00.0 -54:45:00.0	IRC03	N3	5.00e+00 microJy	5	3*	P
2	IRC-ISO	03:11:00.0 -54:45:00.0	IRC03	N4	1.00e+01 microJy	5	3*	P
2	IRC-ISO	03:11:00.0 -54:45:00.0	IRC03	S7	5.00e+01 microJy	5	3*	P
2	IRC-ISO	03:11:00.0 -54:45:00.0	IRC03	S9W	5.00e+01 microJy	5	2*	P
2	IRC-ISO	03:11:00.0 -54:45:00.0	IRC03	S11	5.00e+01 microJy	5	3*	P

The calculated magnitude, either Flux, SNR or number of pointings is marked with *

Figure B.2.10: Output from the Instrument Performance Tool for the IRC input file

Table B.2.4: Observation Details file for the Performance Estimator Tool. Columns are ID number, Target name, Band, flux in mJy (blank), signal/noise, number of pointings and type of source point/diffuse/line

3,"FIS-ISO", N60, ,5.,1 ,P
3,"FIS-ISO", WIDE-S, ,5.,1 ,P
3,"FIS-ISO", WIDE-L, ,5.,1 ,P
3,"FIS-ISO", N160, ,5.,1 ,P

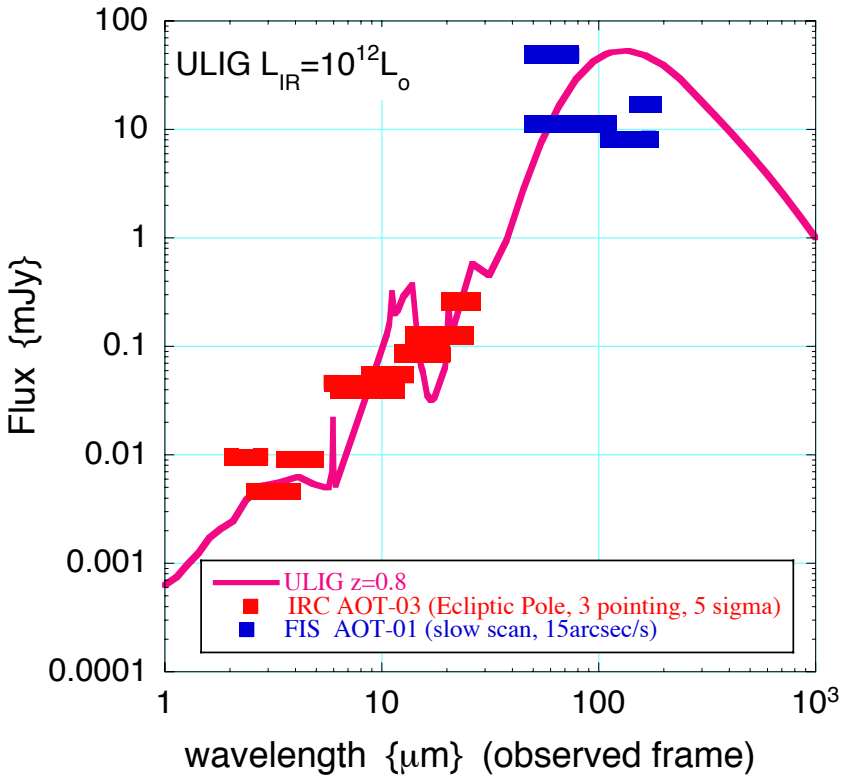

Figure B.2.11: Estimated required sensitivities to detect dusty cold ULIRGs to redshift 0.8. We assume 3 pointings with AOT IRC03, i.e. observations in all 9 filter bands and single FIS01 observation utilizing a scan speed of 15arcsec/s

***ASTRO-F* Instrument Performance Tool result**

ID	TARGET	COORD	AOT	BAND	FLUX	SNR	#POINTINGS	SOURCE/ FLUX TYPE
3	FIS-ISO	03:10:53.73 -54:45:45.78	FIS01	N60	4.88e+04 microJy*	5	1	P
3	FIS-ISO	03:10:53.73 -54:45:45.78	FIS01	WIDE-S	1.06e+04 microJy*	5	1	P
Warning! Detection is limited by cirrus and source confusion = 4.72e+04 microJy in line:								
3	FIS-ISO	03:10:53.73 -54:45:45.78	FIS01	WIDE-L	6.36e+03 microJy*	5	1	P
Warning! Detection is limited by cirrus and source confusion = 5.44e+04 microJy in line:								
3	FIS-ISO	03:10:53.73 -54:45:45.78	FIS01	N160	1.27e+04 microJy*	5	1	P

Note: For FIS01 the Flux and SNR are calculated with the 'number of round trip scan' which is N_rt=N_pointing*2

The calculated magnitude, either Flux, SNR or number of pointings is marked with *

Figure B.2.12: Output from the Instrument Performance Tool for the FIS input file

B.2.8 Submission of Proposal

After the duplication check, we can finally submit our proposal via the web interface. The proposal submission has several stages and we will need to upload various output files saved from the tools we used earlier. Each proposal has a 5 character abbreviation which will be used to identify each proposal. The next step is to upload the Target List which will be automatically verified (syntax only) on uploading. Following this we will be required to upload the results we saved from the output of the Visibility Tool, Duplication Check Tool and Instrument Performance Tool respectively. Once all these files have been uploaded we will have to enter the specific proposal information (name, address, telephone number, etc.) and general proposal information (Co-Is, category, title, abstract). The Scientific Justification must be submitted in PDF format and should not exceed 6 pages in total including scientific rationale, objective, references, figures and tables, and technical feasibility of the proposal. A confirmation page of the submission is created automatically. Shortly after, users will receive a formal confirmation by e-mail with the cover page of their proposal.

B.3 Example 2: Spectroscopy of Planetary Nebulae with the IRC

In this worked example we consider a program to perform spectroscopy on a few Planetary Nebulae with the ASTRO-F IRC instrument. We will simulate the preparation of the proposal from scientific background to proposal submission.

Table B.3.5: Suitable Planetary Nebula for pilot spectroscopic study with ASTRO-F

Name	Equinox	R.A.	Dec.
NGC7027	J 2000	21:07:01.7	+42:14:11.0
SMP83	J 2000	05:36:21.0	−67:18:14.0

B.3.1 Scientific Background

We consider 2 planetary nebulae as a pilot study for spectroscopy with ASTRO-F. These objects have extremely rich and highly ionized spectrum due to their hot central star. Analysis of the spectra can give insight into the evolution and origin of the ionizing central stars. Our first target is NGC7027, a very well known, bright planetary nebula with a rich spectrum that has previously been observed by ISO (Bernard-Salas et al., 2001). The second target is the fainter SMP83 planetary nebula in the Large Magellanic Cloud, also observed by Spitzer (Bernard-Salas et al., 2004). We will perform both high resolution spectroscopy in the near-infrared range which is unique to ASTRO-F, since Spitzer has no capability in this wavelength range. In addition we shall carry out lower resolution spectroscopy over the entire wavelength range of the IRC in order to obtain the dust spectrum of our sources. The target positions are given in Table B.3.5.

B.3.2 Target Visibility

Using the Visibility Tool to check the availability of our targets (entering the co-ordinates using the interface in FigB.2.1) we find that both targets have reasonable visibility. The result of the Visibility Tool is shown in Figure B.3.13. The visibility of SMP83 is extremely high with 86 observable opportunities due to its location almost on the South Ecliptic Pole where as NGC7027 at a more moderate latitude is only visible on 15 orbits. This emphasizes the unique visibility constraints of the ASTRO-F Open Time observations.

The output from the visibility tool should be saved as an ASCII file as it will need to be uploaded as part of the final submission process for our proposal.

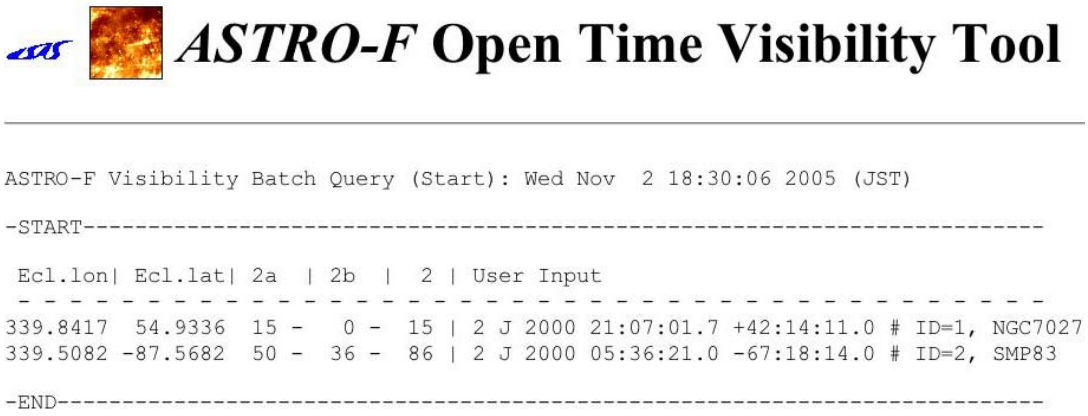

Figure B.3.13: Results from the Visibility Tool. The input data is shown on the right hand side and the output on the left. The output lists the co-ordinates in ecliptic format which is more suitable for the ASTRO-F orbit and the number of pointings available in Phase 2a (first 6 months after Phase 1), Phase 2b (4 months following Phase 2a) and the total number of pointings available for open time observations in the entire Phase 2 of the mission. The '+' & '-' signs refer to the scan direction: corresponding to the FoV moving from North to South in Ecliptic coordinates for the '+' case and in the opposite direction for the '-' case. Note that our second target SMP83 has an extremely high visibility of over 86 due to its location almost on the South Ecliptic Pole at an ecliptic latitude of -87 degrees while NGC7027 has a more moderate visibility of 15 at an ecliptic latitude of 55 degrees. This result emphasises the strong dependence of the visibility of ASTRO-F observations on ecliptic latitude.

Table B.3.6: Target List for submission

1,"NGC7027","J2000", 21:07:01.7, +42:14:11.0,"IRC04","b;Nh",2,A,"","NGC7027 high resolution"
2,"NGC7027","J2000", 21:07:01.7, +42:14:11.0,"IRC04","a;Ns",2,B,"","NGC7027 lower resolution"
3,"NGC7027","J2000", 21:07:01.7, +42:14:11.0,"IRC04","a;Ls",2,C,"","NGC7027 lower resolution"
4,"SMP83","J2000", 05:36:21.0, -67:18:14.0,"IRC04","b;Nh",2,A,"","SMP83 high resolution"
5,"SMP83","J2000", 05:36:21.0, -67:18:14.0,"IRC04","a;Ns",2,B,"","SMP83 lower resolution"
6,"SMP83","J2000", 05:36:21.0, -67:18:14.0,"IRC04","a;Ls",2,C,"","SMP83 lower resolution"

B.3.3 Preparation of Target List

We intend to carry out high resolution spectroscopy with the IRC grism (NG) in the near-infrared as our first priority. Following this, as our second priority, we will observe the entire dust spectrum over the full wavelength range of the IRC. Note that unfortunately, due to degradation, the LG1 channel is not available for spectroscopic observations so we will have a gap of a few microns in the mid-infrared. The spectroscopic IRC AOT is IRC04. This AOT has 2 parameters, the first is the filter set and the second is the position of the slit. The NIR camera has 3 slits. A common slit with the IRC MIR-S camera for spectroscopy of diffuse sources, an entrance aperture for point source spectroscopy and another slit for high resolution spectroscopy with the NG element. In addition, the MIR-L camera also has a slit for spectroscopy of diffuse sources. Since we wish to carry out both high resolution spectroscopy with the NG element and lower resolution spectroscopy with the NP/SG1/SG2 elements, plus the longer wavelength coverage provided by the LG2 element on the MIR-L camera, we require at least 3 pointing per field of view. In addition since no dithering is carried out during this AOT, we must observe each sky area at least twice for data redundancy. Therefore we are looking at a minimum of 6 pointings per target and 3 lines per target in the Target List. Later we shall see with the Instrument Performance Tool that our fainter target (the high visibility SMP83) requires 2 pointings per field of view per AOT. The target list is shown in Table B.3.6. As in the previous example, with have a unique I.D. in ascending but not necessarily contiguous order, followed by some identifier for the target name which in the case of many of our targets should resolvable the NED/SIMBAD systems. The IRC04 AOT has 2 parameters to set, the filter set and the slit position. The filter set is determined by whether we wish to use the NP (filter set *a*) or NG (filter set *b*) element of the NIR camera. We can use the iris_sky tool to visualize our observations and Figure B.3.14 shows the iris_sky tool with the outmost slit of the IRC camera positioned over the target (NGC7027). In this figure, the entrance aperture for point sources and the common inner slit for diffuse sources.

Next we have to choose the slit parameter. For the high resolution spectroscopy, this parameter is *Nh* : the target position is placed at the high resolution slit of the NIR camera. For the lower resolution spectroscopy, the parameter is *Ns* & *Ls* for the NIR/MIR-S and MIR-L cameras respectively. We set the number of pointings as 2 for both the brighter source and for our fainter source which we will confirm with the Instrument Performance Tool later. For this example, we prioritize our targets by the high and low resolution spectroscopy, giving the high resolution observations with NG a priority *A* and the lower resolution spectroscopy with NIR/MIR-S and MIR-L priorities *B* & *C* respectively. Again, as in the previous example we choose not to link our observations together as symbiotic since we can still get decent scientific results with either the high or low resolution spectroscopy.

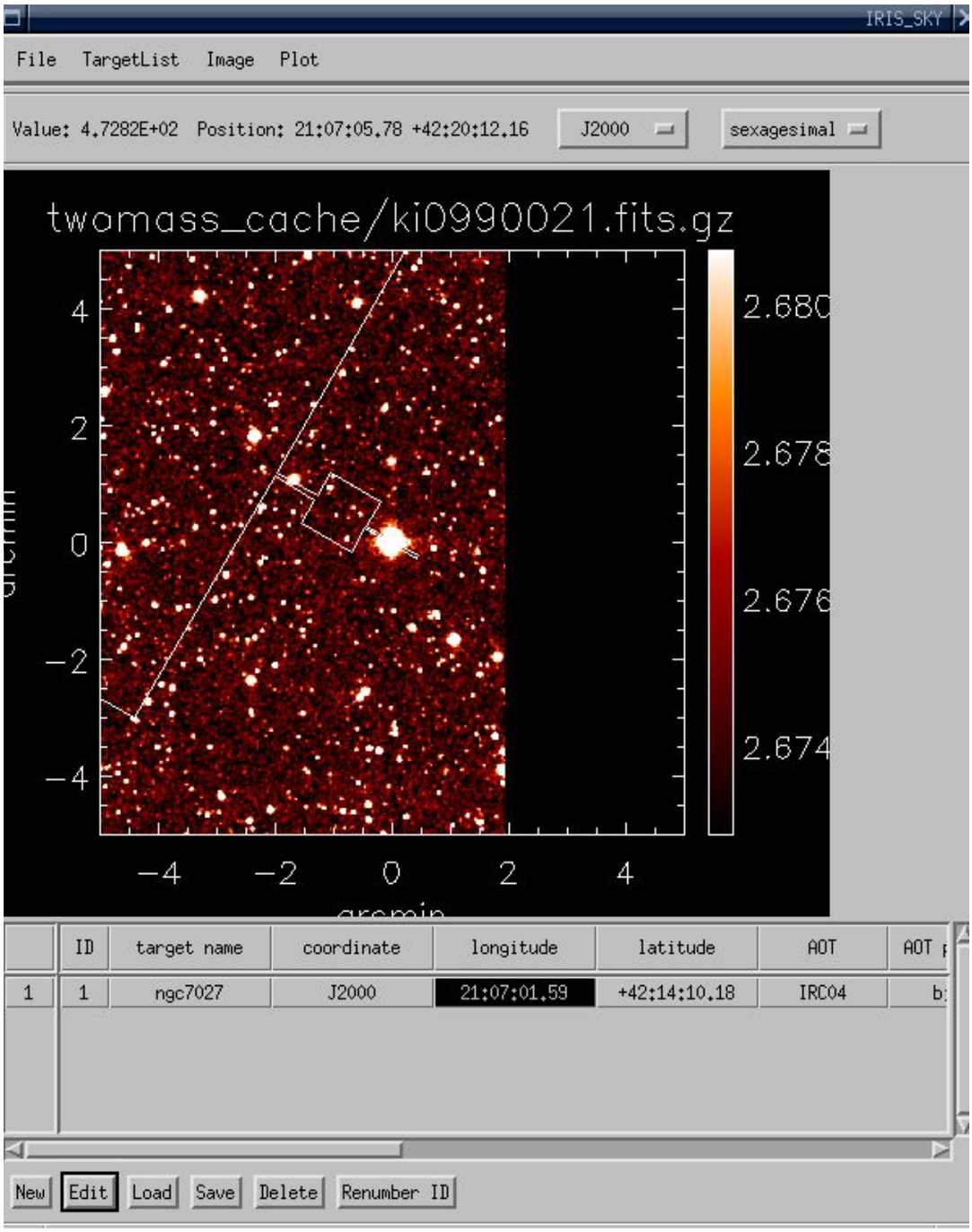

Figure B.3.14: Using the iris_sky tool to overlay the IRC NIR high resolution spectroscopy slit over the Planetary Nebula NGC7027.

B.3.4 Target List Validation

The Target List syntax is validated in an identical manner to the previous imaging example. The target list will also be automatically validated when we upload it during the final proposal submission stage so there is no need for us to save the output of the Validation Check Tool at this stage.

B.3.5 Duplication Checker

Duplicate observations are decided on a basis of position, instrument/AOT and the number of pointings. Putting our target list into the duplication checker we find that indeed there is a conflict of position for one of our fields (see Figure B.3.15). Interestingly, the high latitude target, SMP83, actually in the LMC has escaped conflict with the ASTRO-F LMC LS guaranteed program. The output from the Duplication Check tool should be saved as an ASCII file as it will need to be uploaded as part of the final submission process for our proposal.

ASTRO-F Duplication Check tool results

-START----------

Duplication summary

ID	cor	ra/lon	dec/lat	AOT	Target name	P+AOT	P+Inst	Pos	Result
1	J2K	316.7571,	42.2364	IRC04	NGC7027	0	0	1	Duplication
2	J2K	316.7571,	42.2364	IRC04	NGC7027	0	0	1	Duplication
3	J2K	316.7571,	42.2364	IRC04	NGC7027	0	0	1	Duplication
4	J2K	84.0875,	-67.3039	IRC04	SMP83	0	0	0	OK
5	J2K	84.0875,	-67.3039	IRC04	SMP83	0	0	0	OK
6	J2K	84.0875,	-67.3039	IRC04	SMP83	0	0	0	OK

-END----------

Format Description

Figure B.3.15: Results from the Duplication Checker Tool. We see that one of our targets are in conflict with the guaranteed time on ASTRO-F. Duplication can be made on position, instrument/AOT and the number of pointings.

Table B.3.7: SMP83 line strengths

Wavelength (microns)	Line	Flux $10^{-17} W/m^2$
7.652	[Ne vi]	8.53
10.52	[S iv]	14.7
12.82	[Ne ii]	1.55
13.11	[Ar v]	1.23
14.33	[Ne v]	14.2
15.55	[Ne iii]	10.3
18.73	[S iii]	3.92
24.33	[Ne v]	15.0
25.89	[O iv]	43.7
33.46	[S iii]	3.47
34.84	[Si ii]	2.76

Table B.3.8: Observation Details file for the Performance Estimator Tool. Columns are ID number, Target name, Band, flux in $\mathrm{W\,m^{-2}}$ (blank), signal/noise, number of pointings and type of source point/diffuse/line

1,"SMP83",NG, ,5.,1,L
2,"SMP83",SG2, ,5.,1.,L
3,"SMP83",LG2, ,5.,1.,L

B.3.6 Estimation of Sensitivity for IRC

For our first target (NGC7027) all the lines are brighter than 10^{-15} $\mathrm{W\,m^{-2}}$ (Bernard-Salas et al., 2001), therefore this is well above the IRC detection limits and should be easily observable in a single pointing. The second target (SMP83) presents fainter lines of the order of 10^{-17} $\mathrm{W\,m^2}$, which are closer to the IRC line detection limits (compare for example the LG2 detection limit of $\sim 1 \times 10^{-17}$ $\mathrm{W\,m^2}$ to the S III line given in Table B.3.7 at 18.73 micron of intensity 3.9×10^{-17} $\mathrm{W\,m^{-2}}$. For the shorter wavelength lines, as a first approximation, we can scale the line fluxes of NGC7027 by the distance to the LMC. Under this assumption, we could expect the H2 line at 2.8 microns to be of the order of $\sim 3.0 \times 10^{-17}$ $\mathrm{W\,m^{-2}}$ and the Br alpha line at 4.05 microns to be $\sim 92.0 \times 10^{-17}$ $\mathrm{W\,m^{-2}}$. Using the Instrument Performance Estimator Tool (Target List plus Observation Details File) we can estimate the capability of the IRC in spectroscopy mode. Table B.3.8 shows the Observation Details File to be input into the Performance Tool. For this example we leave the flux field (out of the flux, S/N, number of pointings fields) blank and initially set the number of pointings to 1. The result is shown in Figure B.3.16 and we can see the IRC is sensitive enough to detect these lines in SMP83 in a single pointing! Although we still require 2 pointings for dithering. The output field that is calculated by the Instrument Performance Tool is marked by asterisks for clarity.

The output from the Instrument Performance Tool should be saved as an ASCII file as it will need to be uploaded as part of the final submission process for our proposal.

ASTRO-F Instrument Performance Tool result

ID	TARGET	COORD	AOT	BAND	FLUX	SNR	#POINTINGS	SOURCE/ FLUX TYPE
1	SMP83	05:36:21.0 -67:18:14.0	IRC04	NG	1.91e-18 W/m^2*	5	1	L
2	SMP83	05:36:21.0 -67:18:14.0	IRC04	SG2	6.27e-18 W/m^2*	5	1	L
3	SMP83	05:36:21.0 -67:18:14.0	IRC04	LG2	9.21e-18 W/m^2*	5	1	L

The calculated magnitude, either Flux, SNR or number of pointings is marked with *

Figure B.3.16: Output from the Instrument Performance Tool for the IRC input file for spectroscopy. The calculated fields are marked by asterisks.

B.3.7 Submission of Proposal

After all the tools have been used and the Target List checked, we can finally submit our proposal via the web interface in an identical manner as that described for the previous imaging example in SectionB.2. Remember that we will need to upload the previously saved ASCII files from the outputs of the Visibility, Duplication & Instrument Performance Tools.

REFERENCES

Bernard-Salas et al., A&A, 2001, 367, 949
Bernard-Salas et al., ApJ, 2004, 154, 271
Chapman S.C., Blain A.W., Ivison R.J., Smail I.R., 2003, Nature, 422, 695
Elbaz D., Cesarsky C.J., Chanial P., Aussel H., Franceschini A., Fadda D., Chary R.R., 2002, A&A, 384, 848
Mann R.G., et al. 2002, MNRAS, 332, 549
Papovich C. et al., 2004, ApJSS, 154, 70
Pearson C.P., 2005, MNRAS 358, 141